TRANSPARENT CONDUCTING OXIDES FOR EPSILON-NEAR-ZERO NANOPHOTONICS

A Dissertation

Submitted to the Faculty

of

Purdue University

by

Clayton T. DeVault

In Partial Fulfillment of the

Requirements for the Degree

of

Doctor of Philosophy

December 2018

Purdue University

West Lafayette, Indiana

THE PURDUE UNIVERSITY GRADUATE SCHOOL
STATEMENT OF DISSERTATION APPROVAL

Dr. Vladimir M. Shalaev, Chair
    School of Electrical and Computer Engineering
Dr. Alexandra Boltasseva
    School of Electrical and Computer Engineering
Dr. Leonid Rokhinson
    Department of Physics and Astronomy
Dr. Francis Robicheaux
    Department of Physics and Astronomy

Approved by:
    Dr. John Finley
        Department of Physics and Astronomy

To Mom

ACKNOWLEDGMENTS

First and foremost, I would like to acknowledge my advisor, Professor Vladimir Shalaev, who has not only provided exceptional guidance and mentorship, but also care, understanding, and encouragement during my PhD. I am both grateful and honored to have been a part of his Purdue family. I would also like to express my deepest gratitude to Professor Alexandra Boltasseva for her wisdom, support, and encouraging direction, to Professor Alexander Kildishev for sharing his profound intellect, wonderful humor, and love of life, and to Dr. Alexei Lagoutchev for his tutelage, insightful discussion, and spending hours with me in the optics lab.

I would also like to express my sincere appreciation to those colleagues who I have had the honor to work alongside. Thank you to Professors Marcello Ferrera, Nathaniel Kinsey, Guru Naik, Sergei Bozhevolnyi, Daniele Faccio, and Justus Ndukaife; Doctors Simeon Bogdanov, Paul West, Misha Shalaginov, Jongbum Kim, Anders Pors, Piotr Nyga, Zhaouxian Wang, Amr Shaltout, Urcan Guler, Xiangeng Meng, Jieran Fang, Ludmila Prokopeva, Rohith Chandrasekar, Jingjing Liu, Swati Pol, Vladimir Zenin, Naresh Emani, and Zhaxylyk Kudyshev; and, finally my colleagues Di Wang, Krishnakali Chaudhuri, Soham Saha, Oksana Makarova, Deesha Shah, Sajid Choudhury, Aveek Dutta, Harsha Eragamreddy, Sam Peana, Shaimaa Azzam, and Sarah Chowdhury.

In addition to my Purdue family, I would like to acknowledge the many friendship I developed during my time here. Life would have been boring without the adventures.

I would like to express both my love and appreciation to my best-friend, companion, and wife, Nyssa, who was patient and steadfast through all the highs and lows. I am overwhelmed with happiness that we get to continue this story together, and I cannot wait to see what comes next.

Finally—and most importantly—I would like to thank my parents, Nick and Susan, and my brother, Cole. They have been understanding, supportive, and loving throughout this chapter of my life, and I do not feel that any written or spoken word can express the immense and immutable love I have for them. I have thought of each of you each and every day and love you completely.

TABLE OF CONTENTS

Page

LIST OF TABLES . . . ix

LIST OF FIGURES . . . x

ABSTRACT . . . xvii

1 INTRODUCTION . . . 1
  1.1 Outline . . . 2

2 TRANSPARENT CONDUCTING OXIDES . . . 5
  2.1 Fabrication . . . 6
  2.2 Linear Optical Properties: Drude-Sommerfeld and Lorentz Models . . . 6
    2.2.1 Ellipsometry Parameter Retrieval . . . 11

3 EPSILON-NEAR-ZERO PROPERTIES OF TCOS . . . 13
  3.1 ENZ Modes . . . 14
  3.2 Enhancing Nonlinear Optics with ENZ Materials . . . 20
    3.2.1 Field Intensity Enhancement . . . 22
    3.2.2 Static and Slow Light . . . 24

4 ULTRAFAST AND NONLINEAR OPTICS WITH TRANSPARENT CONDUCTING OXIDES . . . 27
  4.1 Ultrafast Optical Dynamics in Semiconductors and Metals . . . 28
  4.2 Refractive Index Modulation at Epsilon-Near-Zero . . . 30
  4.3 Pump Probe Experiments . . . 31
    4.3.1 Interband Dynamics . . . 34
    4.3.2 Intraband Dynamics . . . 36
    4.3.3 Controlling Hybrid Nonlinearities . . . 39
    4.3.4 Modulation Bandwidth and Wavelength Control . . . 41
  4.4 Dynamic Control of Nanocavities with Transparent Conducting Oxides 44
    4.4.1 Nanocavity Fabrication and Design . . . 45
    4.4.2 Dynamic Modulation with Intraband Pump . . . 46
    4.4.3 Numerical Model . . . 49
  4.5 Discussion and Conclusions . . . 51

5 SINGLE AND DIMER NANOANTENNAS ON ENZ SUBSTRATES . . . 53
  5.1 Fabry-Pérot Model for Single Nanorod . . . 55
  5.2 Single Nanorod Far-Field Characterization . . . 61
  5.3 Single Nanorod Near-Field Characterization . . . 65

Page
5.4 Suppression of Near-Field Coupling in Plasmonic Dimer Antennas . . . 67
5.5 Discussion and Conclusions 70

6 STRONG COUPLING BETWEEN ENZ FILMS AND PLASMONIC ANTENNAS 73
6.1 Coupled Harmonic Oscillators 74
6.2 ENZ Mode in Aluminum-doped Zinc Oxide Thin Films 77
6.3 Conclusions 84

7 OUTLOOK AND CONCLUSIONS 87

REFERENCES 90

LIST OF TABLES

Table Page

4.1 **Summary of the Extracted Properties of Ga:ZnO Film** 49

5.1 **Ellipsometry Model and Fits** 63

LIST OF FIGURES

Figure Page

2.1 Drude-Sommerfeld Model of the Dielectric Permittivity. (a) Real portion of the permittivity for a fixed damping constant of $\Gamma = 0.001\omega_p$ and carrier concentrations (in unites of cm^{-3}) of $n = 5 \times 10^{21}$ (Red), $n = 1 \times 10^{22}$, (Magenta), and $n = 2 \times 10^{22}$ (Blue). Larger values of n blue-shifts the cross-over wavelength and makes the TCO behave as a metal at smaller wavelengths. (b) Imaginary portion of the permittivity for a fixed plasma frequency $\hbar\omega_p = 0.8$ eV and varying values of damping rates, $\Gamma = 0.001\omega_p$ (Red), $0.01\omega_p$, (Magenta), and $0.5\omega_p$ (Blue). Larger damping constants increase the imaginary portion of the permittivity. 9

2.2 Lorentz Model of the Dielectric Permittivity. (a) Real and imaginary (b) portion of the permittivity for different pairs of central resonance frequencies and damping coefficients: $\hbar\omega_p = 4.5$ eV, $\hbar\gamma = 0.01$ eV (Red); $\hbar\omega_p = 3.5$ eV, $\hbar\gamma = 0.05$ eV (Blue); and $\hbar\omega_p = 2.5$ eV, $\hbar\gamma = 0.1$ eV (Magenta). In general, the larger the damping term, the broader the resonance. 10

3.1 Dispersion Relation of a Thin Drude Film. Mode solutions of Eq. 3.1 are plotted for film thicknesses of $d = \infty, 150$, and 2 nm to demonstrate the splitting of the two plasma branches. For very thin films, the long range plasmon exhibits a very flat dispersion at the plasma frequency, and the mode is referred as the ENZ mode. Inset shows a schematic of the three-layered system. 17

3.2 Perfect Absoprtion in ENZ Films. Absorption spectrum of transverse magnetic light incident at the perfect absoprtion angle of various TCO films. The TCO films have ENZ points which vary from 1100 to 2300 nm. 19

3.3 Field Intensity Enhancement. Amplitdue color-maps of the ratio between the normal electric field inside a TCO and the total incident field for different wavelengths and incident angles. The TCO is a 23-nm film with ENZ wavelength of 1440 nm, and a damping constant of $\gamma = 0.01$ (a), $\gamma = 0.1$ (b), and $\gamma = 0.1259$ (c). The ENZ wavelength is indicated by the dotted white line. The magnitude of the enhancement and the line width are observed to be invsersely and directly, respectively, proportional to the damping constant 23

Figure Page

3.4 ENZ for Boosting Phase-Dependent Nonlinear Interactions. a) Normalized electric field amplitude of a normal-incident wave on an ENZ material with a permittivity of $\epsilon = 0.1, 0.01$, and, 0.001 demonstrating the wavelength scaling $1/\sqrt{\epsilon}$. Schematic of phase-matching in a non-epsilon-near-zero (ENZ) media (top,b) and an ENZ media (bottom,c). Phase variation is constant across the ENZ media and contributes to both forward and backward signal generation. 25

3.5 Group Velocity in an ENZ Material of $\gamma = 0, 0.3, 0.8$, and 0.13 with $\lambda_{ENZ} = 1420$ nm. For all but the ideal ENZ material ($\gamma = 0$), the group velocity is small but finite for wavelengths greater than the ENZ wavelength.26

4.1 Modulation of an Epsilon-Near-Zero Material. Absolute change in the reflection of a purley real ($Img\,[n] = 0$) material versus base refractive index provided an index change of $\delta n = -0.1$. The magnitude of the reflection coefficients are calculated using Fresnel's equations at a single interface between air ($n_0 = 1$) and the material assuming normal incidence. Note that operating in the epsilon-near-zero regime (i.e. $n < 1$) provides larger absolute changes in the reflection for the same change in refractive index. 32

4.2 Two-color Pump Probe Experiment. (a) Schematic of the two-color pump-probe experimental set-up where the two pump wavelengths, 787 nm (NIR) and 262 nm (ultraviolet), are illustrated along with the probe wavelength of 1,300 nm. The delay between the two pump pulses is denoted Δt while the delay between the probe and ultraviolet signal is denoted $\Delta\tau$. For intraband excitation using only the NIR pump, Δt is defined as the delay between the probe and NIR pump pulse arrival time. The black arcs indicate the arrival time of the pulses. (b) Change in transmission at 1300 nm versus the pumpprobe delay $\Delta\tau$ under 262 nm excitation fitted with simulation. The inset illustrates the process diagram for interband excitation: ultraviolet light ($E_{ultraviolet}$) generates electron-hole pairs (δ_n, δ_p) above the Fermi level (E_f) in addition to the intinsic concentration (N_i), which recombine through mid-gap trap states (N_t, τ_r). (c) Change in transmission at 1300 nm versus the pumpprobe delay $\Delta\tau$ under 787 nm excitation fitted with simulation. The inset illustrates the process diagram for intraband excitation: NIR light (E_{NIR}) raises the temperature of conduction band electrons ($T_{cool} \rightarrow T_{hot}$), which relax through scattering processes (τ_{e-p}), heating the lattice. 35

Figure Page

4.3 Dynamic Change in the Optical Response of AZO Thin Films Triggered by Two-Color Excitation. Percent change of the real (a-e) and imaginary (f-j) part of the refractive index as a function of the delay $\Delta\tau$ between the ultraviolet pump and the infrared probe pulses. Multiple vertical plots are shown, for different delay Δt between the ultraviolet and the NIR pump pulses. Shaded areas indicate whether the ultraviolet pump, which is used as time reference, precedes (light blue) or follows (light red) the NIR pump. Overlapping the results obtained by simultaneous two-colour pumping (red curves), we plot the computed change in refractive index calculated by the algebraic summation of the results obtained from experiments with separate ultraviolet and NIR pump pulses (black dashed curves). The probe, the NIR, and the ultraviolet pump wavelengths were set to 1300 nm, 787 nm, and 262 nm, respectively. The probe intesntiy was low: $I_p \approx 5$ mJ cm^{-2}, while the pump fluences were $F_{ultraviolet} = 5$ mJ cm^{-2} and $F_{NIR} = 14$ mJ cm^{-2} 40

4.4 Two-Color Pumping Effects. (a) Change in the probe pulse transmission as a function of the pumpprobe delay ($\Delta\tau$) and the inter pumpdelay (Δt). The ultraviolet (UV) pump decreases the transmission, whereas the NIR increases it. The combined effect produces a Δt-dependent modulation. The modulation bandwidth is evaluated by performing a Fourier transform along $\Delta\tau$, and is shown by the black curve in (b). For delays close to $\Delta t = 0$, the modulation bandwidth can be decreased or increased by the two-colour combined effect. The blue and red dashed lines show the bandwidth of the ultraviolet-only and NIR-only driven modulation. (c) Measured central wavelength shift of the transmitted probe pulse (≈ 15 nm bandwidth) in a zoomed $\Delta t - \Delta\tau$ region (square box in a). The ultraviolet pump blue shifts the probe wavelength, whereas the NIR pump does the opposite. At $\Delta t \approx 0$, the opposite effects almost entirely cancel the wavelength shift. (d) Summary of the findings in c, showing the maximum positive ($\Delta\lambda_+$) and negative ($\Delta\lambda_-$) wavelength shift for the NIR-only (red-dashed/dotted), ultraviolet only (blue-dashed/dotted) and two-color (solid black) Al:ZnO excitation. 43

Figure Page

4.5 Active Nanocavity Design. (a) Cross-sectional schematic of the Ga:ZnO embedded nanocavity. The thickness of both top and botom silver mirror is 24 nm; the total thickness of alumina is 230 nm; and the thickness of Ga:ZnO is 70 nm. The reflection phase-shift from the metal mirrors (ϕ_m) and the phase accumulated throughout the cavity ($4\pi nL/\lambda$) is indicated. (b) Analytic transmittance of the nanocavity for several Ga:ZnO filling fractions (FF $= L_{Ga:ZnO}/\left(L_{Ga:ZnO} + L_{Al_2O_3}\right)$). The first-order resonance of the cavity occurs at a wavelength of 1200 nm for all FF, but the total transmittance decreases for larger FF due to the Ga:ZnO losses. The red line indicates the optimal FF choice considering both total transmittance and modulation performance. 45

4.6 Ultrafast Modulation of the Nanocavity. (a) Pump-probe setup. (b) Normalized Gaussian fit (orange line) of the Lorentzian maxima representing the probe pulse is compared to the resonance (green dashed line) measured by ellipsometry on the nanocavity with Ga:ZnO and without a metasurface. For the sake of clarity only few spectra are shown. (c) Normalized resonance shift of about $\Delta\lambda = 15$ nm of the nanocavity with 70 nm Ga:ZnO film and under pump excitation of intensity $I_p = 9$ mJ cm^{-2}. . . . 48

4.7 Transient Response of the Nanocavity. Percentage of the change in transmission as a function of the delay $\Delta\tau$ between the pump and probe pulses in Ga:ZnO embedded nanocavity. Transient dynamics is modeled with two temperature model (pink solid line). Three temporal phases have been identified: rise time, modulation region, and thermal tail. (b) Dielectric functions of Ga:ZnO thin film. Real (solid) and imaginary (dotted) part of permittivity of Ga:ZnO films are extracted by spectroscopic ellipsometry measurement without pump and fitted by numerical simulations with pump. (c) Refractive index of Ga:ZnO films calculated from the extracted dielectric function. Temporal positions for on/off pump states are indicated in panel a. 50

5.1 Semi-analytical Fabry-Pérot model for single nanorod. (a) Sketch of a nanorod upon normal illumination, exciting two counter-propagating nanorod modes. (b,c) Electric field distribution of nanorod waveguiding mode at the free-space wavelength of 1475 nm, deposited on (b) a Al:ZnO and (c) a ZnO substrate. Magenta arrows represent transverse electric field. (d,e) Numerically calculated effective mode index, propagation length, and reflection coefficient for a gold nanorod on the Al:ZnO (solid lines) and a ZnO substrate (dashed lines). Insets show the approximate configurations of the finite-element solver. 57

Figure Page

5.2 Comparison of the field produced by full 3D FEM simulations and semi-analytical Fabry-Pérot model. Simulations are done for gold antennas on Al:ZnO substrate at 1500 nm excitation from the bottom, polarized along the antenna length. The field was calculated at $z = 20$ nm (i.e., through the middle of the antenna, top) and $z = 90$ nm (i.e., 50 nm above the antenna, bottom) for two antenna lengths: 600 (left) and 1800 nm (right). The fields were normalized to the amplitude of the transmitted plane wave (note different colormap scales). 60

5.3 Far-field characterization of nanorod arrays. (a) Cross-polarized configuration of our ellipsometer used for measuring the far-field scattering of the single antenna arrays. The input polarization is rotated $-45°$ with respect to the nanorod's long axis and incident at 18°. The reflected light is passed through an analyzer set at the 45°. (b) Resonant wavelength as a function of antenna length for the Al:ZnO (black) and ZnO (red) substrates. The solid lines are calculated using the Fabry-Pérot model; square and circular markers are results of scattering cross-section numerical calculations; and cross markers indicate experimental values obtained from cross-polarization spectroscopy. The dashed line indicates the ENZ wavelength of 1475 nm. 62

5.4 Permittivity values of the Al:ZnO film extracted using spectroscopic ellipsometry. The ENZ wavelength,λ_{ENZ}, is defined when real part $\epsilon' = 0$. 64

5.5 Representative SEM image of (a) single and (b) dimer nanoantenna arrays deposited on Al:ZnO substrates. 65

5.6 Near-field optical microscopy of individual nanorods. (a) Schematic of the SNOM setup. (b) First column contains the measured topography, the magnitude, and the phase of the near-field for gold antennas on Al:ZnO substrate at 1475 nm excitation, polarized along the antenna length (the polarization is shown with a white arrow). Second and third column are the corresponding z-component of the electric field (E_z) calculated at 50 nm above nanorods with full 3D finite-element simulations and semi-analytical Fabry-Pérot model, respectively. Recorded topography and designed antenna parameters were used for masks in phase maps. 66

Figure Page

5.7 Suppression of near-field coupling in dimer antennas. (a) Scattering, extinction, and absorption cross-sections of dimer antennas on both Al:ZnO (left column) and glass (right column) substrates calculated with FEM. Gap distances of 10 and 200 nm are shown in the top and bottom rows, respectively. The antenna lengths are chosen such that the maximum cross-sections coincide at a gap distance of 200 nm to clearly illustrate the distinction in total red-shift. (b) Resonance wavelength red-shift of dimer nanoantennas as a function of gap size, normalized to a gap of 200 nm. Black squares and line mark the experimentally measured and simulated, respectively, red-shift of dimers on Al:ZnO as a function of gap size. Red line marks simulated red-shift for dimers on glass. Inset shows the collected cross-polarized reflection spectra. 69

5.8 Resonance wavelength of dimer antennas as a function of gap size and antenna length. The resonance wavelength was calculated as a position of the peak in the simulated extinction spectra. Bottom image shows a shift of the resonance wavelength for dimer antennas, normalized to the resonance wavelength of dimer antennas with a 200-nm gap. The shift is reduced with a decrease of antenna length for ENZ substrate, while it is nearly the same for antennas on a glass and ZnO substrate or in vacuum. . 71

6.1 Coupled Harmonic Oscillators. (a) Real portion of the complex eigenvalues of two coupled harmonic oscillators as a function of the variable frequency parameter $\delta\omega$ for a coupling constant of $g = 0\langle\gamma\rangle$, $0.5\langle\gamma\rangle$, $1\langle\gamma\rangle$, $1{,}5\langle\gamma\rangle$, and $2\langle\gamma\rangle$. Resonance amplitude of each oscillator in the (b) weak coupling regime, with a coupling parameter $g = 0.5\,\langle\gamma\rangle$, and (c) the strong coupling regime, with a coupling parameter $g = 2.0\,\langle\gamma\rangle$ 76

6.2 Plasmonic-ENZ System. (a) Schematic of the plasmonic antenna on an ENZ film, along with pictorial depiction of the antenna and ENZ film as two coupled harmonic oscillators. (b) SEM image of the gold nanoantennas deposited on a 23-nm-thick Al:ZnO film. (c) Real (black line, left axis) and imaginary (red line, right axis) dielectric constants of the Al:ZnO flim retrieved with spectroscopic ellipsometry, where the ENZ wavelength of 1440 nm is indicated with a dashed black line. (d) Dispersion relation of the air-ENZ-glass three-layered system (see inset). The long (short) range plasmon is indicated with a blue(red) line. The long range plasmon approaches the screened plasma frequency (i.e. ENZ wavelength) for large wavevectors β, as indicated by the nearly flat dispersion. The solid blue line indicates the mode bound to the film, while the dashed blue line is a wave which leaks into the substrate. 78

Figure Page

6.3 Transmission spectra of antennas on ultrathin ENZ film. (a) FDTD and (b) experimental transmission spectra of gold plasmonic antennas on 23 nm-thick Al:ZnO film. Transmission curves correspond to different antenna lengths and are separated for clarity. Triangles and diamonds correspond to the minimum transmission wavelength for the antenna and ENZ mode, respectively. (c) FDTD and (d) experimental color maps of the transmission as a function of antenna length and wavelength. Anti crossing behavior is observed near the ENZ wavelength of 1440 nm. 80

6.4 Wavelengths of the transmission minimum as a function of antenna length. Blue (Red) dots: minimum experimental transmission of ENZ (antenna) mode . Blue (Red) line: theoretical fit of the coupled harmonic oscillator model to the ENZ (antenna) mode. Black horizontal dashed (dashed dot) line: uncoupled resonance wavelength of the ENZ (antenna) mode. Extracted g value (in wavelengths) indicated by the purple arrow at the anti crossing point. Inset shows the pictorial description of the coupled harmonic oscillator model. 82

6.5 FDTD transmission and reflection spectra of ENZ-nanorod array. (a) Illustration of FDTD simulation for varying gap sizes. (b) Transmission and (c) reflection of ENZ-nanorod array as a function of the distance (d) between the antenna and the ENZ film. (d) Illustration of FDTD simulations for varying ENZ film thickness. (e) Transmission and (f) reflection of ENZ-nanorod array as a function of varying ENZ film thickness. 83

ABSTRACT

DeVault, Clayton T. PhD, Purdue University, December 2018. Transparent Conducting Oxides for Epsilon-Near-Zero Nanophotonics. Major Professor: Vladimir M. Shalaev.

Epsilon-near-zero materials are an emerging class of nanophotonic materials which engender electromagnetic field enhancement and small phase variation due to their approximate zero permittivity. These quasi-static fields facilitate a number of unique optical properties such as supercoupling, subwavelength confinement, and enhanced light-matter interactions, which has made epsilon-near-zero media a rapidly expanding field of optical physics. Contemporary methods of realizing a system with zero permittivity rely on microwave cavities/waveguides or complex metal-dielectric metamaterials; however, both techniques require advanced fabrication and their operational wavelength is fixed relative to their geometric and optical parameters. It remains an open and substantial challenge to realize an epsilon-near-zero material at pertinent wavelengths, particularly near- and mid-infrared, with tunable/dynamic properties. The focus of this thesis is the exploration of transparent conducting oxides for the development of epsilon-near-zero nanophotonic phenomena and applications. Transparent conducting oxides have an inherent low permittivity, in addition to simple fabrication and tunable optical properties, making them exceptionally promising. Application of transparent conducting oxide films for highly confined modes, nonlinear/ultrafast optics, and strongly coupled systems are discussed.

1. INTRODUCTION

The permittivity of a material captures the complex nature of light-matter interactions in a single number. Universally denoted with the Greek symbol epsilon (ϵ), the permittivity dictates the propagation of electromagnetic radiation throughout Nature, manifested as our visual perception of color, refraction, reflection, and transmission, in addition to fundamental physical properties transcending our eye's tiny spectrum. Control of light, from simple lenses to complex laser systems, is mediated by the ability to incorporate the appropriate permittivity into an optical technology, which is directly facilitated by the judicious choice of an appropriate optical material [1–4]. Therefore, there exists an intimate connection between optical physics and materials sciences, bridged together by the desire to advance discovery and control of light's most fascinating properties.

Before the advent of modern materials and optical sciences, selecting the appropriate permittivity was largely accomplished with trial and error (an early version of the scientific method). Today, armed with Maxwell's equations, quantum mechanics, and advanced material fabrication techniques, we can now control materials at sub-wavelength and even atomic scales to provide an extended range of permittivity values beyond those that occur "naturally" [5–9]. Engineered/artificial optical materials can now exhibit permittivities from extraordinarily large ($\epsilon > 5$) [10, 11] to exceptionally small ($\epsilon \approx 0$). Materials which exhibit this latter feature (i.e. $\epsilon \approx 0$) are named—rather appropriately—as *Epsilon-Near-Zero Materials* and are the focus of this thesis.

Interest in epsilon-near-zero materials has grown at a prolific rate in the last decade, largely driven by numerous theoretical demonstrations of exceptional—if not somewhat confrontational—electromagnetic phenomena and applications, including super-coupling, sub-wavelength tunneling, wavefront engineering, field confinement, and enhanced nonlinearities [12–20]. These studies were largely pioneered by the scientists Richard Ziolkowski, Adrea Alú, and Nader Engheta, who continue to lead the front of epsilon-near-zero research.

Experimental observation of epsilon-near-zero phenomena has largely concentrated within the microwave spectrum where the permittivity can be easily manipulated [21, 22]. Although these experiment have confirmed many fascinating properties of epsilon-near-zero materials, the desired spectral window of application is across the ultraviolet, visible, near- and mid-infrared. Unfortunately, achieving epsilon-near-zero conditions at these wavelengths is challenging and remains the prominent focus of experimentalist in the field. The two common approaches focus on (1) engineering an artificial material (i.e. metamaterial) to exhibit a zero permittivity [23–27], or (2) synthesizing materials which have an inherent zero or near-zero permittivity [28–31]. Both approaches have advantages/disadvantages, and the particular strategy to achieve a zero permittivity is absolutely dependent on what particular phenomena is to be observed and the wavelength of interest. Particularly, there is a growing interest in applying epsilon-near-zero phenomena for the near-infrared wavelengths where a large density of optical technologies exist including telecommunication, biological imaging, and quantum sciences.

1.1 Outline

The contents of this thesis are the major results of my doctoral research and pertain to *the development of transparent conducting oxides for near-infrared epsilon-near-zero materials and their application for nanophotonic applications.* It is divided into two parts, which focus, respectively, on epsilon-near-zero ultrafast, nonlinear optics and plasmonic coupling. For brevity, I outline each chapter below:

CHAPTER 2: Fundamentals of Transparent Conducting Oxides Discusses the development of transparent conducting oxides for alternative plasmonics, their fabrication, optical properties, and ellipsometry techniques.

CHAPTER 3: Epsilon-Near-Zero Physics Provides a background of epsilon-near-zero phenomena relevant to the contents of this thesis. It details the epsilon-near-zero modes of ultrathin TCO films, the benefits of ENZ materials for nonlinear optics, and discusses alternative material platforms for realization of ENZ media.

CHAPTER 4: Ultrafast, Nonlinear Optics with Epsilon-Near-Zero Films Contains an introduction to ultrafast processes in semiconductors and metals; a discussion of the modulation performance of ENZ flims; the ultrafast and nonlinear response, as measured by pump-probe, of aluminum-doped zinc oxide to interband, intraband, and simultaneous excitation; and, finally, the use of these processes for the design of a dynamic, ultrafast nanocavity.

CHAPTER 5: Single and Dimer Nanoantennas on Epsilon-Near-Zero Films Details the response of single and dimer plasmonic antennas on an aluminum-doped zinc oxide substrate with an ENZ wavelength close to the resonance of the antennas. An analytic model, numerical simulations, and experimental observations demonstrate two phenomena of plasmonic antennas on ENZ films: resonance-pinning and suppression of near-field coupling.

CHAPTER 6: Coupling between Epsilon-Near-Zero Films and Plasmonic Antennas Here, the interaction of a plasmonic antenna and a thin film of aluminum-doped zinc oxide supporting an ENZ mode are shown to exhibit strong coupling. ENZ modal anaylsis and a coupled oscillator model is developed to retrieve the Rabi splitting energies of the system, verifying the system is within the strong coupling regime.

2. TRANSPARENT CONDUCTING OXIDES

Any user of a modern touch-screen smart phone has a tangible familiarity with transparent conducting oxides. A touch-screen consists of two conducting layers separated by a spacer [32,33]. A weak voltage is applied to the bottom conductor and a capacitance is formed. When a finger or pen contacts the top layer, the capacitance at that point changes and is resolvable with sensors inside the screen. TCOs are essential to this technology exactly because they are both conductive and transparent, unlike most conductors which are opaque. Popular TCOs for touchscreen devices include indium tin oxide (ITO) and amorphous indium gallium zinc oxide (a-IGZO), although several other types exist and offer comparative performance but at lower cost and/or toxicity [34,35].

The origin of TCOs unique optical and electrical properties is their material composition. Oxides such as zinc oxide, indium oxide, and cadmium oxide have large bandgaps ($>$ 4 eV) and do not absorb visible light. When doped with metal interstitials (e.g. aluminum, gallium, indium, dysprosium), these oxides can support free electron carrier concentration as large as 10^{22} cm^{-3}. Furthermore, these TCOs have small effective masses and low-resistivity, which make them excellent conductors [29,36,37].

TCOs have gained considerable attention from the nanophotonics community in the past decade precisely because of their unique physical properties. Particularly, TCOs are being developed as alternative materials for plasmonics [28,29,31,38]. Plasmonics is a sub-field of nanophotonics and is concerned with leveraging the oscillations of free electrons in a metal to concentrate and/or enhance optical fields [39–41]. Noble metals are the most common choice of plasmonic material because of their large carrier concentration, low optical losses, and mature fabrication techniques; however, several inherent disadvantages of noble metals prohibit the realization of real-world plasmonic technologies, such as fabrication limitations, CMOS incompatibility, and lack of tunability [42]. This last detrimental feature—the lack of tunability–is one of the most prominent advantages of TCOs over noble metals. For instance, TCOs have a widely tunable carrier concentration via both static methods such as thermal annealing or defect/dopant chemistry and dynamic control including electrical biasing and photoinduced carriers. This property is exceptionally beneficial for the design of active nanophotonics and plasmonics [43–45].

2.1 Fabrication

TCOs can be grown as films and nanoparticles through a variety of methods including sputtering, laser ablation, evaporation, solution processing, chemical vapor deposition, and vapor-liquid-solid techniques [34, 46]. Their optical properties are largely dependent on the deposition technique and have made direct comparison between various TCOs difficult. We have chosen pulsed laser deposition (PLD) to fabricate all TCO films because this method provides consistent stoichiometric properties. PLD is the ablation of a target material (typically a high purity TCO) using an intense ultraviolet laser beam [47]. Film thickness is controlled via deposition time and carrier concentration is dependent on the partial pressure and temperature of the chamber. For example, oxygen defects contribute additional free carriers in addition to those from the metal dopant. By depositing the TCO with a partial pressure of oxygen, interstitials and vacancies bring the carrier concentration to larger values [48, 49]. PLD is also a convenient method because nearly any substrate is suitable, although the crystallinity of the TCO can be dependent on the substrate.

2.2 Linear Optical Properties: Drude-Sommerfeld and Lorentz Models

The optical properties of TCOs can be described by a simple complex dielectric function. The dielectric function captures the response of the TCO subject to an external electromagnetic field. To calculate this response, we look to establish a relation between an applied electric field and the induced polarization field, i.e.

$$\boldsymbol{P}(\omega) = \epsilon_o \chi(\omega) \boldsymbol{E}(\omega). \tag{2.1}$$

From this, we can calculate the displacement field

$$\boldsymbol{D}(\omega) = \epsilon_o \epsilon(\omega) \boldsymbol{E}(\omega) = \epsilon_o \boldsymbol{E}(\omega) + \boldsymbol{P}(\omega) \tag{2.2}$$

and finally the frequency-dependent dielectric function

$$\epsilon(\omega) = (1 + \chi(\omega)). \tag{2.3}$$

At first, we only consider the contribution from the conduction electrons and apply the Drude-Sommerfeld model [50]. This model assumes the electrons in a material are delocalized and free to move throughout a static ionic background. Additionally, all electron-electron and electron-ion interactions are ignored; the only interaction is the instantaneous collisions with ions which occur, on average, every τ seconds. If we assume a time-harmonic driving field, the displacement of a free electron will obey

$$m^* \frac{d^2 \boldsymbol{x}}{dt^2} + m^* \Gamma \frac{d\boldsymbol{x}}{dt} = e \boldsymbol{E}_o e^{-i\omega t}, \tag{2.4}$$

where e and m^* are the charge and effective mass of the free charge and $\boldsymbol{E}_o$ and ω are the frequency of the applied electric field. The damping term Γ is proportional to $\tau^{-1} = l/\nu_f$, where ν_f and l are the Fermi velocity and electron mean free path. Assuming a time harmonic displacement $\boldsymbol{x}(t) = \boldsymbol{x}_o e^{-i\omega t}$, we can solve for the dielectric function by inserting $\boldsymbol{P} = ne\boldsymbol{x}$ into Eq. 2.1 and 2.3; the results yield

$$\epsilon_D(\omega) = 1 - \frac{\omega_p^2}{\omega^2 + i\Gamma\omega} \tag{2.5}$$

where $\omega_p = \sqrt{ne^2/(m^*\epsilon_o)}$ is the plasma frequency and n is the electron density. For DC-fields ($\omega = 0$) Eq. 2.5 diverges to infinity, which is the condition of a perfect conductor, i.e. Drude metals behave as perfect semiconductors for frequencies much larger than the plasma frequency.

In Fig.2.1a the real portion of the Drude-Sommerfeld is plotted as a function of wavelength for several different carrier concentration and a fixed damping term. For increasing carrier concentrations, the cross-over frequency (defined as the transition wavelength when $\epsilon' = 0$) shifts to higher energies. Note that the real portion of the permittivity exhibits a transition from positive to negative values near the plasma frequency ω_p. For $\omega < \omega_p$ a TCO will behave as a metal, since the electrons move approximately π-radians out-of-phase with respect to the driving field. For $\omega > \omega_p$ the electrons are over-driven and the TCO starts to behave as a dielectric and transmits incoming light. The carrier concentration values are typical of standard TCOs. Fig.2.1b shows the change of the imaginary portion of the permittivity for a fixed plasma frequency (i.e carrier concentration), but with varying damping rates. The simplified Drude-Sommerfeld model of permittivity is extremely accurate and useful at frequencies far from the bandgap; however, for higher energies, the dielectric response becomes influenced by interband transitions. For low energy photons, the predominant interactions involve intraband transitions, i.e. electronic interactions near the Fermi surface. However, as the photon frequency increases, larger intraband transitions occur in the conduction band and eventually interband transitions begin to contribute.

To account for the interband transitions, we use the Lorentz model which assumes that valence band electrons can be treated as localized or bound electrons. The equation of motion then becomes

$$m_{eff}\frac{d^2\boldsymbol{x}}{dt^2} + m_{eff}\gamma\frac{d\boldsymbol{x}}{dt} + \alpha\boldsymbol{x} = e\boldsymbol{E}_o e^{-i\omega t}. \tag{2.6}$$

Here, m_{eff} is the effective mass of the valence band electron, γ is the damping constant predominately associated with radiate recombination, and α is a phonological spring constant associated with the restoring force of the atom. Proceeding in an analogous fashion as in the Drude-Sommerfeld derivation, the Lorentz dielectric constant is found to be

$$\epsilon_L(\omega) = 1 + \frac{\tilde{\omega}_p^2}{(\omega_o^2 - \omega^2) - i\gamma\omega} \tag{2.7}$$

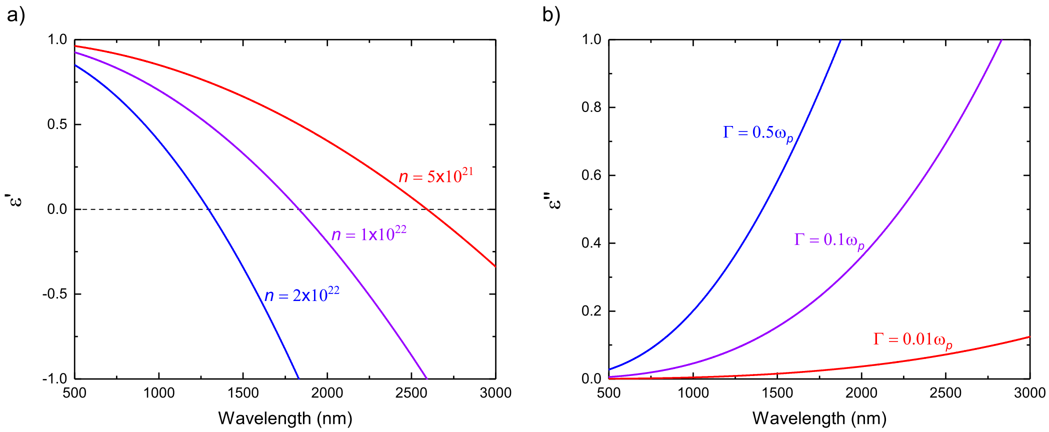

Figure 2.1. Drude-Sommerfeld Model of the Dielectric Permittivity. (a) Real portion of the permittivity for a fixed damping constant of $\Gamma = 0.001\omega_p$ and carrier concentrations (in unites of cm^{-3}) of $n = 5 \times 10^{21}$ (Red), $n = 1 \times 10^{22}$, (Magenta), and $n = 2 \times 10^{22}$ (Blue). Larger values of n blue-shifts the cross-over wavelength and makes the TCO behave as a metal at smaller wavelengths. (b) Imaginary portion of the permittivity for a fixed plasma frequency $\hbar\omega_p = 0.8$ eV and varying values of damping rates, $\Gamma = 0.001\omega_p$ (Red), $0.01\omega_p$, (Magenta), and $0.5\omega_p$ (Blue). Larger damping constants increase the imaginary portion of the permittivity.

In this case, the plasma frequency is defined in terms of the bound electron density $\tilde{n}$, i.e. $\tilde{\omega}_p = \sqrt{\tilde{n}e^2/(m_{eff}\epsilon_o)}$, and $\omega_o = \sqrt{\alpha/m}$. The nomenclature at this point should be evident: the dielectric function of interband transitions is a Lorentzian curve centered at the interband transition frequency with a line width dictated by the damping coefficient. Fig.2.2 shows the real (a) and imaginary (b) portions of the Lorentz dielectric function for varying central resonance frequencies and damping coefficients. The full dielectric function of a material is the sum of both interband and intraband transitions. In general, there are multiple interband transitions occurring throughout the entire electromagnetic spectrum, including non-electronic transitions

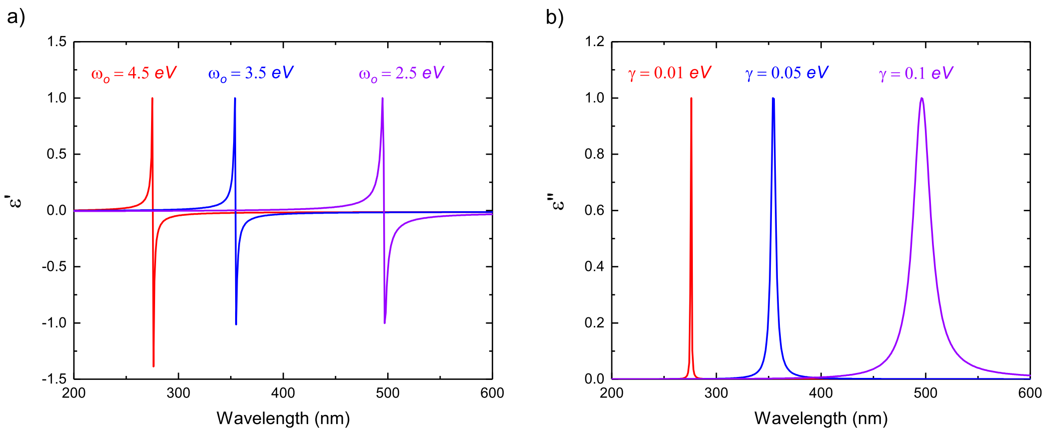

Figure 2.2. Lorentz Model of the Dielectric Permittivity. (a) Real and imaginary (b) portion of the permittivity for different pairs of central resonance frequencies and damping coefficients: $\hbar\omega_p = 4.5$ eV, $\hbar\gamma = 0.01$ eV (Red); $\hbar\omega_p = 3.5$ eV, $\hbar\gamma = 0.05$ eV (Blue); and $\hbar\omega_p = 2.5$ eV, $\hbar\gamma = 0.1$ eV (Magenta). In general, the larger the damping term, the broader the resonance.

such as optical phonons. The general expression for the dielectric function is given by [51]

$$\epsilon(\omega) = 1 - \frac{\omega_p^2}{\omega^2 + i\Gamma\omega} + \frac{Ne^2}{\epsilon_o m^*}\sum_i f_i(\omega_i^2 - \omega^2 - i\gamma_i\omega), \qquad (2.8)$$

where each resonance has an associated oscillator strength f_i and damping term γ_i and N is the number of molecules per unit volume. When considering a particular frequency window, it is typically necessary to keep the terms which have central resonances near or within the region of interest. This means the remaining Lorentz resonances are far away from resonance and, in total, only contribute a background term to the dielectric function; this term is referred to as the background permittivity and is denoted by ϵ_∞. Although this derivation is purely classical, it can be shown that the by considering quantum effects the dielectric function is nearly identical to Eq. 2.8.

Unlike metals, TCOs have Lorentz absorption terms which are deep in the ultraviolet and far from the Drude-Sommerfeld plasma frequency. In this way, the large imaginary portion contribution from the interband absorption does not contribute additional losses to the Drude term. Therefore, TCO can behave as near-perfect Drude metals.

2.2.1 Ellipsometry Parameter Retrieval

To access the dielectric functions experimentally, we perform spectroscopic ellipsometry on films of TCOs. Ellipsometry is a linear optical characterization technique for measuring the dielectric constants of films [52, 53]. In ellipsometry, the ratio of the reflection coefficient of s- and p-polarized light is measured, r_s/r_p, and both the amplitude ratio, $\tan(\Psi)$, and phase difference, Δ, is experimentally collected. These measured values are directly related to the film thicknesses and their respective dielectric permittivities via Fresnel's equations [1,3]. Although it is at this point possible to use the experimental values to back-calculate the permittivities and thickness of each film using regression analysis or similar numerical techniques, the permittivities can be more accurately determined if they are constrained using a numerical model. For TCO films, an ideal model is Drude+Lorentz (Eq.2.8). Throughout this work, we fit all ellipsometry measurements to a Drude+Lorentz function since the ellipsometer's spectral window ranges from 300-2500 nm and only one interband transition occurs for the TCOs under consideration. Once we have specified the permittivity model, regression analysis is used to minimize the mean squared error (MSE) between the experimental data and the permittivity/thickness parameters of the model. An MSE > 10 is considered a good fit. Generally, better MSE values are obtained when the film thicknesses are known, which can be accomplished using SEM cross-sectional analysis of film structures.

3. EPSILON-NEAR-ZERO PROPERTIES OF TCOS

Somewhat surprisingly, there is not a consistent or clear definition of what constitutes an epsilon-near-zero material. The ambiguity arises because various authors have followed, for the most part, two different conventions: the first asserts that a material is ENZ provided the real portion of the permittivity is approximately zero, $\epsilon' \approx 0$, while the second claim the absolute value of both the real and imaginary portions must be approximately zero, $|\epsilon'| + |\epsilon''| \approx 0$. Although the distinction appear minute, the implications can be drastic. For example, the former definition implies that metals have an ENZ wavelength at visible or ultraviolet wavelengths, even though the imaginary portion is extremely large [54]; however, certain processes—as we analyze later in this chapter—are dependent on the both the real and imaginary portions of permittivity, and the effect becomes insignificant when losses are large. On the other hand, losses do not always play a large role and ENZ effects have been observed in systems with a zero real permittivity, but very large imaginary [55]. Therefore, there is not a clear definition of ENZ since particular physical phenomena may depend on only the real permittivity, the imaginary portion, or a combination of both. For instance, in the context of low-index (LI) materials, the refractive index is dependent on both real and imaginary portions of the permittivity [1] via $n = Re\left[\sqrt{\epsilon}\right] = \sqrt{|\epsilon' + \epsilon''| + \epsilon'}/\sqrt{2}$ which has a minimal value which is distinct from the ENZ wavelength [56]. Although both definitions are arguably accurate, I define epsilon-near-zero materials as having the sum of the absolute real and imaginary permittivity which is approximately zero (i.e. the latter definition, $|\epsilon'| + |\epsilon''| \approx 0$). This choice reflects my experimental and numerical studies of materials with low permittivity values, as the most prominent effects occur for materials within this definition. Furthermore, I choose to distinguish between ENZ and low-index materials. My research has focused entirely on non-magnetic materials where the permeability is unity ($\mu = 1$). Therefore, the complex refractive index is directly calculated with $n = \sqrt{\epsilon}$, so any phenomena dependent can be succinctly interpreted in the context of the permittivity without convolving the problem.

Near the bulk plasma frequency, $\omega_b = \omega_p/\sqrt{\epsilon_\infty}$, of a TCO film, the real portion of the dielectric permittivity is approximately zero, while the imaginary portion remains small because of the low damping constant, $\gamma \ll \omega_p$. Therefore, TCOs are inherent ENZ materials at this spectral range. Since these materials have relatively simple fabrication and synthesis methods, TCOs represent a convenient material platform for realizing ENZ systems in contrast to complicated artificial structures which require advanced fabrication [23–25]. Furthermore, their tunable carrier concentrations allow for ENZ wavelengths which can extend throughout the near- and mid-infrared wavelengths. Beyond these properties, TCOs have demonstrated remarkable potential for two emerging applications and fields of study: ENZ modes and Enhanced Nonlinear Optics. The following two sections discuss these properties in detail and provide fundamental background relevant to the remaining chapters of this thesis.

3.1 ENZ Modes

Ultrathin films of TCOs support unique types of modes which occur near the ENZ wavelength in addition to surface plasmon polaritons existing in the metallic $Re\{\epsilon\} < 0$ region [57, 58]. Modes of a film are defined as solutions to Maxwells equations in the absence of source excitations. Considering a film of permittivity ϵ_2 and thickness d, surrounded by two regions with permittivity ϵ_1 (superstrate) and ϵ_3 (substrate), a solution of Maxwells equations exists provided the following dispersion relation is satisfied [58]

$$f(\beta, \omega) = 1 + \frac{\epsilon_1 \gamma_3}{\epsilon_3 \gamma_1} - i \tan(\kappa d) \left(\frac{\epsilon_2 \gamma_3}{\epsilon_3 \kappa} + \frac{\epsilon_1 \kappa}{\epsilon_2 \gamma_1} \right) = 0. \tag{3.1}$$

Here, $\gamma_{1,3} = \pm\sqrt{\epsilon_{1,3} k_o^2 - \beta^2}$ and $\kappa = \sqrt{\beta^2 - \epsilon_{1,3} k_o^2}$ are the transverse wave numbers, ω is the angular frequency, $k_o = \omega/c$ is the free-space wave number, and β is the longitudinal wave number. The dispersion relation is derived by applying Maxwells boundary conditions to a three-layer system with the assumption of TM polarization. Eq. 3.1 is a complex valued transcendental equation and must be solved numerically by either selecting a complex ω and solving for a real-valued β or *vice versa*, by selecting a complex β and solving for a real-valued ω. A complex-frequency, real-wave vector description represents waves which decay temporally, where a complex-wave vector, real-frequency describes waves with a spatial decay. To a degree, both representations are equivalent and capture pertinent physics of the modes; however, certain scenarios benefit from choosing one representation over the other, such as calculating the local density of states [59–62]

Both bound and leaky modes exist depending on the sign of the transverse wave numbers $\gamma_{1,3}$ in the superstrate and substrate. Consider the case of bound modes where the out-of-plane exponentially decays into the top and bottom semi-infinite layers; this is done by selecting negative values of the superstrate and substrate's transverse wavenumber, i.e. $(-\gamma_1, -\gamma_3)$. We assume the permittivity of the film is given by Drudes formula $\epsilon_2 = 1 - \frac{\omega_p^2}{\omega(\omega + i\gamma)}$ where ω_p is the plasma frequency and γ is the damping constant (see Eq. 2.5). Furthermore, for simplicity, we let the superstrate and substrate be vacuum ($\epsilon_{1,3} = 1$). To solve Eq. 3.1, we will choose a complex frequency ($\tilde{\omega} = \omega + i\gamma$), real wavenumber ($Img\,[\beta] = 0$) representation to avoid back-bending and set $\omega_p/\gamma = 100$. The sign convention of the complex frequency is selected such that $exp\,(-i\tilde{\omega}t) = exp\,(-i\omega t + \gamma t)$, which imlies negative values of γ correspond to temporal decay instead of gain.

Solving complex transcendental equations can be tricky, since many root-finding methods fail in the complex plane. Newton's method is one such method which will work for complex equations, but this method requires an initial guess which is close to the true zero [63]. The other disadvantage of this method and others methods which rely on initial guess parameters is that there may be a large number of zeros. A more general approach is the argument principle method (APM) which allows for the determination of every complex root in a particular complex domain [64,65]. This approach consists of calculating the contour integrals of an analytic complex function about some closed region C,

$$\frac{1}{2\pi}\int_C z^m \frac{f'(z)}{f(z)} dz = \sum_{i=1}^{N} z_i^m = S_m \tag{3.2}$$

for $m = 1, 2, 3..., S_o$, where S_o is the number of zeros in the region C, and z_i are the roots of $f(z)$ inside C. Eq. 3.2 leads to a system of equations that can be used to construct a polynomial of degree S_o, which has the same roots as $f(z)$. The constructed polynomial can be more easily solved numerically [66]. The convenience of this method is that, within a chosen region C, the initial number of zeros can be calculated S_o and, depending on if this number is greater (less) than one, the region can be expanded (divided). Care must be taken when choosing the contour as to avoid both singularities and branch cuts. We use the APM method to solve Eq. 3.1 in order to find all modal solutions within a domain which is consistent with $Re\,[\omega] > 0$ and $Img\,[\omega] < 0$ (no gain).

Fig. 3.1 shows the solutions to the dispersion equation for several film thicknesses. Here, the inset shows the schematic of the three layered structure, with air on either side of a variable-thick Drude film. For very thick films ($d \rightarrow \infty$), we find Eq. 3.1 reduces to the dispersion of a semi-infinite metal-dielectric interface and exhibits a surface plasmon branch (Fig. 3.1, solid red line). As the films thickness is decreased past the skin depth, the surface plasmons at each interface begin to interact and form two branches. These two surface plasmons are referred to as long-range (LR) and short-range (SR) surface plasmon polaritons. The blue and magenta lines in Fig. 3.1 show the dispersion of both LR (solid) and SR (dashed) branches for film thicknesses of d = 150 nm and 2 nm. For the d = 2 nm film, the LR mode becomes nearly flat and asymptotically approaches the dispersion of the plasma frequency within a range of wavenumbers. Thus, this mode occurs at exactly the frequency where its permittivity is approximately zero and is referred to as the Epsilon-Near-Zero mode. This mode lies on the right side of the light line, so it will not couple to free space and requires excitation via Kretchmann configuration, grating coupling, or scattering element; furthermore, this mode will only couple to TM polarized light. The electric field within the film is highly confined due to the discontinuity of the displacement field and enhances the transverse electric field component inversely proportional to the film thickness i.e. $E_z \sim 1/d$ [58]. Although we have considered a simplified system, the ENZ mode exists for a large range of both superstrates and substrates, including both dielectrics and metals. We can solve for the leaky modes of the system

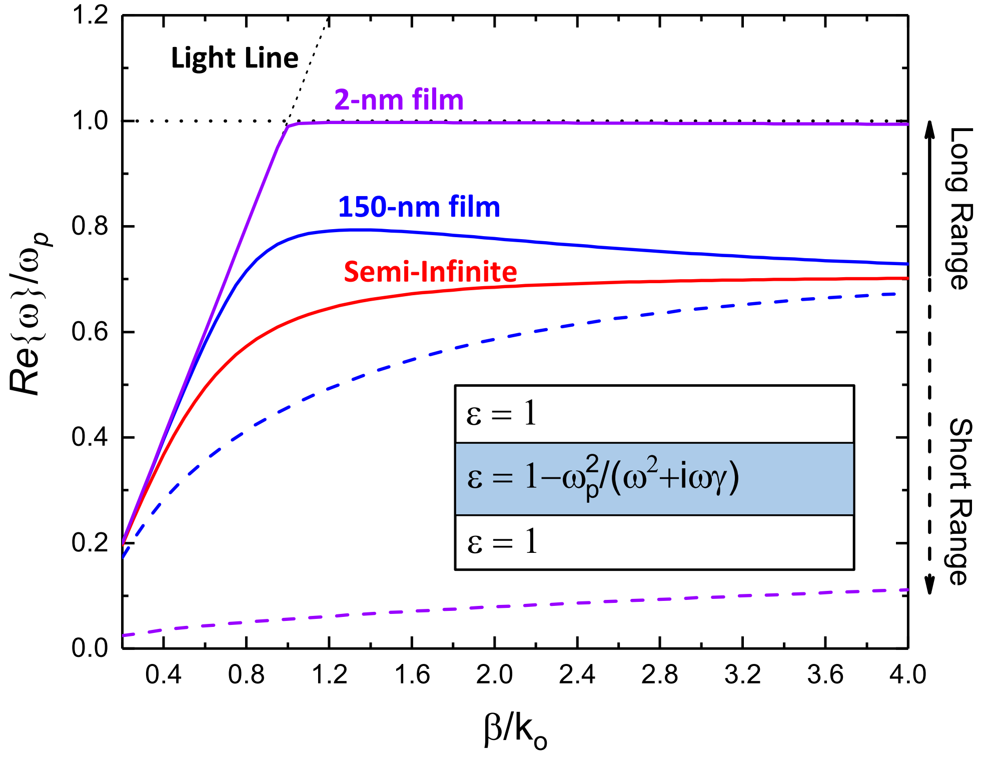

Figure 3.1. Dispersion Relation of a Thin Drude Film. Mode solutions of Eq. 3.1 are plotted for film thicknesses of $d = \infty, 150$, and 2 nm to demonstrate the splitting of the two plasma branches. For very thin films, the long range plasmon exhibits a very flat dispersion at the plasma frequency, and the mode is referred as the ENZ mode. Inset shows a schematic of the three-layered system.

by choosing positive signs of the vacuum's transverse wavenumber i.e. $(+\gamma_1, +\gamma_3)$. Above the plasma frequency, this branch also exhibits a flat dispersion near the plasma frequency for extremely thin films. Here, the branch lies to the left of the light line and can couple directly to free space. In literature, this mode is denoted as either the Berreman or the Brewster mode. The distinction appears to be nomenclature only, based on the difference in which materials were being studiedBerreman modes were associated with polaritonic material (e.g. SiC) and Brewster modes with metals and doped semiconductors (e.g. GaAs) [62].

An extremely pertinent feature of these modes is the strong polarization- and directional-dependent absorption at ENZ frequencies. Remarkably, near-perfect absorption is achievable in deeply subwavelength films of ITO coated on metallic substrates [67]. This perfect absorption coincides with the transition from bound to leaky modes and correspond to a mode profile of a totally absorbed incoming plane wave. These results are general and perfect absorption is achievable in many materials which exhibit an ENZ point; several examples of materials with perfect absorption features are shown in Fig. 3.2. Several works have utilized this unique property of ENZ films for the design of selective thermal and mid-infrared emitters consisting of either ultrathin films of doped semiconductors or phononic materials [68, 69]. More recently, there has been a growing interest to develop dynamic perfect absorbing films by taking advantage of phase-change materials such as vanadium dioxide or the ultrafast nonlinearities of the ENZ metal oxide films themselves [70]. Ultrafast polarizers have been realized by pumping a film of indium-doped cadmium oxide and inducing a red-shift in the high-quality factor Berreman perfect absorption dip. The s-to-p polarization extinction ratio was demonstrated to be 91 with an overall switching speed of 800 fs [71]. Most recently, perfect light absorption was demonstrated in an ultrathin ITO film which could be tuned via doping concentration and electrical bias with a shift of 20% the perfect absorption wavelength [72]. ENZ and Berreman modes have also been studied in the context of coupled light-matter interactions. Initial investigations focused on the coupling between planar metamaterials and

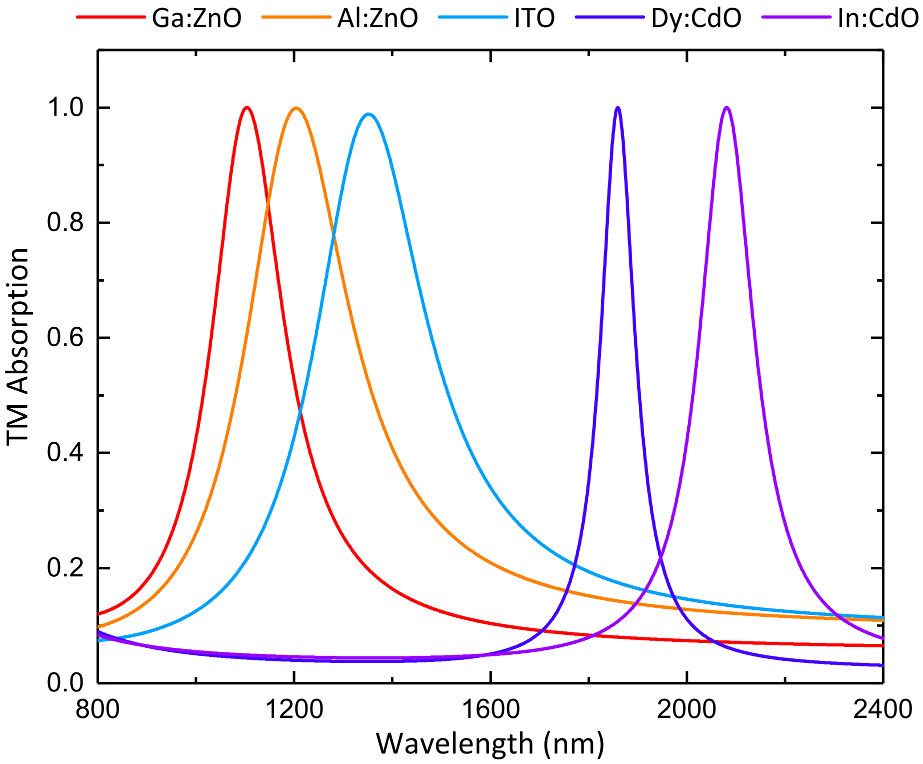

Figure 3.2. Perfect Absoprtion in ENZ Films. Absorption spectrum of transverse magnetic light incident at the perfect absoprtion angle of various TCO films. The TCO films have ENZ points which vary from 1100 to 2300 nm.

doped semiconductor nanolayers at near- and mid-infrared wavelengths [58, 73, 74]. Large Rabi splitting was observed in these systems because of the strong coupling between the metamaterial resonators and the ENZ mode of the nanolayers. Strong coupling between a single surface phonon polariton at a SiC/AlN interface with an ENZ phonon polariton in the ultrathin AlN film was very recently demonstrated and shown to exhibit hybrid features of the constituent modes, namely long propagation and ultrahigh field confinement [75]. The ability to enhance the light-matter interactions in this strong-coupling regime has also engendered promising applications in nonlinear optics. Experimental demonstrations of optically induced refractive index changes ±2.5 was recently accomplished using optical dipole antennas deposited on an ultrathin (23 nm) film of ITO which supported a near-infrared ENZ region [76,77]. The extremely large nonlinearity is attributed to the coupling between the antenna resonance and the ENZ mode of the film. The following section discusses the origin of these nonlinearities in further detail.

3.2 Enhancing Nonlinear Optics with ENZ Materials

Solutions of Maxwell's equations in a material require a specific relation between the displacement and electric field $\mathbf{D}(\mathbf{E})$ or, equivalently, the polarization and the electric field $\mathbf{P}(\mathbf{E})$ [51]. These are the constitutive relations and capture the response of a material's atoms and molecules to an applied electric field. In reality, the response is never exactly proportional to the input, or in other words, that is the response is nonlinear. The subject of nonlinear optics is concerned with understanding the nonlinear response of an optical material and utilizing the emergent phenomena to control light in novel ways [78–80].

The standard tool-kit of nonlinear optics is perturbation theory. Here, the response of the material is assumed to be equivalent to a series expansion in terms of an applied electrif field. In the frequency-domain, the polarization density components $\tilde{P}_i$ is expanded about the electric field components $\tilde{E}_j = 0$

$$\tilde{P}_i = \epsilon_o \left(\chi^{(1)}_{i,j} \tilde{E}_j + \chi^{(2)}_{i,j,k} \tilde{E}_j \tilde{E}_k + \chi^{(3)}_{i,j,k,l} \tilde{E}_j \tilde{E}_k \tilde{E}_l + ... \right) . \tag{3.3}$$

In Eq. 3.3, the response of the atoms and molecules are hidden inside the nonlinear coefficients $\chi^{(n)}$, which are assumed to follow standard series convergence properties, i.e. $\chi^{(n+1)} \gg \chi^{(n)}$. Physically, this condition is satisfied provided the applied electric fields are weak compared to those within the material, which is generally true for the atomic response of electrons [79]. However, there are many situations in which the series expansion of Eq. 3.3 fails, such as resonant interactions or electron ionization., and therefore, caution should be applied when analyzing novel materials and systems.

Epsilon-near-zero materials are materials which have not only shown promising potential for enhancing nonlinear interactions, but also brought to question the validity of the perturbative expansion (Eq. 3.3) [81, 82]. Consider, the third-order nonlinear Kerr effect which occurs when the intensity of a single beam is strong enough to modify the refractive index of a material. For the case of linear polarized light, the nonlinear polarization is subject to a third-order perturbation term,

$$\tilde{P}_i(\omega) = \frac{3}{4}\epsilon_o \chi^{(3)} |\tilde{E}_i(\omega)|^2 \tilde{E}_i(\omega) \tag{3.4}$$

which implies an intensity-dependent refractive index

$$n(I) = n_o + \left(\frac{3\chi^{(3)}}{4n_0 Re\left(n_o\right) c\epsilon_o} \right) I = n_o + n_2 I \tag{3.5}$$

where $n_o = \sqrt{\epsilon}$ is the complex refractive index of the material in terms of the permittivity ϵ, c is the speed of light, I is the intensity of the electric field, ϵ_o is the permittivity of free space, $\chi^{(3)}$ is the third-order material response, and n_2 is the Kerr refractive index. Eq. 3.5 is derived using the power series approximation $\sqrt{1+x} \approx 1 + x/2$, where $x \propto \chi^{(3)}/(1+\chi^{(1)})$; however, for an epsilon-near-zero material, $(1+\chi^{(1)}) = 0$ and this series expansion is no longer valid. Therefore, we conclude that Eq.3.5 is unusable for the case of an *ideal* epsilon-near-zero material. However, for our considerations of TCOs, the imaginary portion of permittivity remains large enough at the epsilon-near-zero point that we will consider Eq. 3.5 valid. In fact, even for material platforms which have shown to have extremely small losses (SiC), the ratio of the linear and third order responses remains considerably small. It is an open question as to whether or not there exists a system with an absolute permittivity which would cause significant divergence in the nonlinear terms. It may even be possible that such a system does not exist in Nature, since simultaneous zero real and imaginary permittivity may not be consistent with Kramers Kronig relations [79, 83].

Under the assumption that Eq.3.5 is valid, the experimental value of typical third-order response of TCOs has been found to be $\chi^{(3)} \sim 10^{-20}$ m^2 V^{-2}, equivalent to a Kerr refractive index of $n_2 \sim 10^{-13}$ cm^2 W^{-1}. These values are not exceptional and are similar to values reported for silicon. Indeed, an enhancement of the Kerr index has been observed to follow the inverse relationship with linear refractive index (Eq.3.5), but these values are relatively modest, providing a factor of 4-times enhancement (following directly from calculating $1/|n_o(\lambda_{ENZ})|$). Although this would seem to imply that TCOs are somewhat mediocre nonlinear materials, the total refractive index modulation is found to be consistently large and approaching unity-order modulation, $\delta n \sim n_o$. Why the large modulation? Simply put, TCOs are capable of surviving under large field intensities (i.e high damage thresholds) [77,81,82]. Therefore, the best strategy for utilizing these materials for nonlinear optics is to couple light efficiently inside. Fortunately, TCOs at their ENZ wavelength have the natural property of electric field enhancement. This is discussed in the following section.

3.2.1 Field Intensity Enhancement

Maxwell's boundary conditions imply an inherent field-enhancement property in ENZ materials. Continuity of the normal displacement field $\hat{n} \cdot (\mathbf{D}_1 - \mathbf{D}_0) = 0$ across the interface of two materials with permittivity ϵ_0 and ϵ_1, respectively, gives

$$\frac{\epsilon_0}{\epsilon_1} E_{n,0} = E_{n,1}. \tag{3.6}$$

Thus, if $\epsilon_1 \to 0$, then $E_n \to \infty$. This effect is observable by calculating the field intensity enhancement, which we define consistent with literature [84] as,

$$FIE = |E_{z,1}|^2 / |E_0|^2 \tag{3.7}$$

where $E_{z,1}$ is the z-component of the electric field amplitude on the $z = 0^+$ plane (inside the TCO), and E_0 is the total electric field incident on the $z = 0^-$ plane (outside the TCO). To illustrate the field enhancement, we calculate the fields of a unity-amplitude p-polarized electric field incident on a thin film (23 nm) TCO surrounded by air using the transfer matrix method. The incident field propagates from $z = -\infty$ to the air-TCO interface situated at the $z = 0$ plane. The fields inside ($z = 0^+$ plane) and outside ($z = 0^-$ plane) the interface are evaluated at a value of $z = \pm 0.5$ nm. Fig. 3.3 shows the FIE amplitude for a TCO with a damping constant of $\gamma = 0.01$ (a), $\gamma = 0.1$ (b), and $\gamma = 0.13$ (c) with all plasma frequencies set such that $\lambda_{ENZ} = 1440$ nm; the final values (Fig. 3.3c) are taken from experimental ellipsometry of a 23-nm Al:ZnO film. All films exhibit a strong enhancement of the normal field component at the ENZ wavelength of the film and for a particular angle of incidence, but the magnitude and line width of the FIE is largest and narrowest for low-damping films. This follows directly from Eq. 3.6 since the normal electric field is inversely proportional to the complex value of ϵ_1 and not soley the real portion.

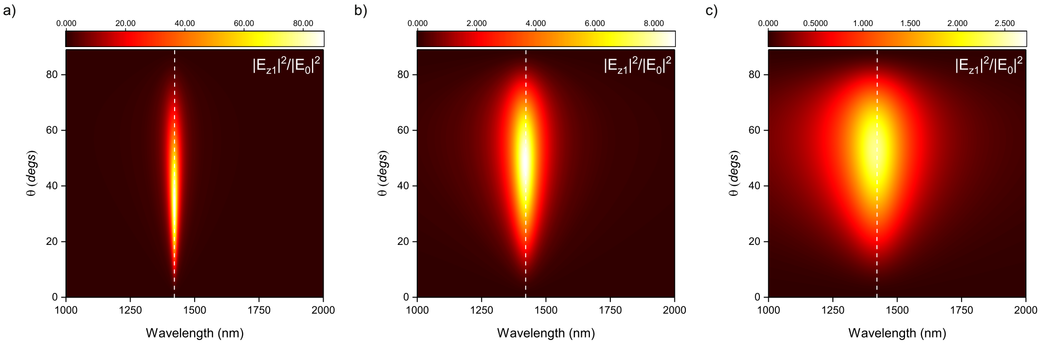

Figure 3.3. Field Intensity Enhancement. Amplitdue color-maps of the ratio between the normal electric field inside a TCO and the total incident field for different wavelengths and incident angles. The TCO is a 23-nm film with ENZ wavelength of 1440 nm, and a damping constant of $\gamma = 0.01$ (a), $\gamma = 0.1$ (b), and $\gamma = 0.1259$ (c). The ENZ wavelength is indicated by the dotted white line. The magnitude of the enhancement and the line width are observed to be invsersely and directly, respectively, proportional to the damping constant

The electric field enhancement of the normal electric field correlates well with observations of enhanced nonlinearities in simple TCO films, including the angular dependence [77]. Although TCOs are isotropic materials and do not exhibit a χ^2 response, second harmonic generation is possible at an interface [79] due to the anharmonic normal field components. Therefore, it may be possible to observe a strong second harmonic (SHG) enhancement of TCO films near their ENZ wavelength and particular incident angle. Some inital studies and theoretical results have pointed to this effect, although the exact mechanism for the enhancement is still under question [85–87].

3.2.2 Static and Slow Light

Two additional effects of ENZ materials could be relevant for enhancing nonlinear optical interactions. The first is wavelength extension which occurs due to the reduced permittivity whereby $\lambda_{ENZ} = \lambda_o/\sqrt{\epsilon}$ such that when the permittivity ϵ is small, the wavelength increases drastically. The consequence of this is a negligible phase advance $kL = 2\pi L/\lambda_{ENZ} \rightarrow 0$ of the wave for films with thickness (L) much larger than the free-space wavelength. This has been used to achieve phase-matching free nonlinear optics [88–90], super-coupling [15, 16, 22], and antenna resonance pinning [91–94]. Fig. 3.4a visual demonstrates this effect for several, purely-real permittivity values. All fields have been normalized to unity for illustrative purposes; otherwise, the transmitted field inside the ENZ media would be significantly smaller due to the large impedance mismatch. Fig. 3.4a and b show the possibility of increasing a nonlinear interaction which is dependent on phase-matching. The uniform phase accumulation across the ENZ media increases the coherence of the nonlinear emitter. This effect has particular relevance to four-wave mixing experiments since the phase conjugate beam automatically satisfies the momentum relation since the pump wavevectors are zero in a ENZ material, i.e. $2\mathbf{k}_p + \mathbf{k}_{pr} = \mathbf{k}_{pr} = \mathbf{k}_c$, where $\mathbf{k}_p = 0$ is the pump wavevector, $\mathbf{k}_{pr}$ is the probe wavevector, and $\mathbf{k}_c$ is the phase-conjugate wavevector [89, 95].

The second effect is the reduction of group velocity i.e. slow light. As the permittivity approaches zero from the positive side, transverse electromagnetic modes experience a cutoff at the crossover wavelength as $k \rightarrow 0$ while from the negative side $k \rightarrow \infty$. At this wavelength, the phase velocity $v_p = c/\sqrt{\epsilon}$ becomes large, while the group velocity $v_b = \partial\omega/\partial k$ becomes small [96–99]. As a result, energy propagating in

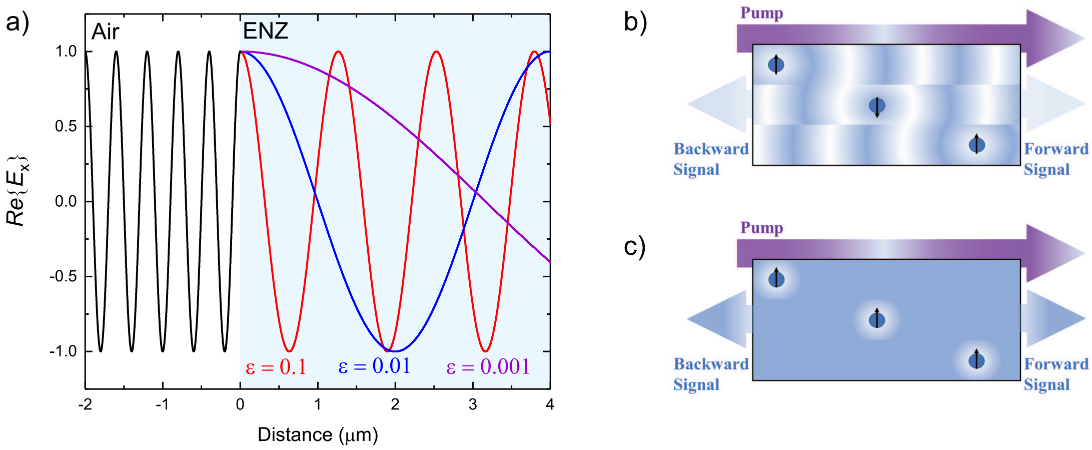

Figure 3.4. ENZ for Boosting Phase-Dependent Nonlinear Interactions. a) Normalized electric field amplitude of a normal-incident wave on an ENZ material with a permittivity of $\epsilon = 0.1, 0.01$, and, 0.001 demonstrating the wavelength scaling $1/\sqrt{\epsilon}$. Schematic of phase-matching in a non-epsilon-near-zero (ENZ) media (top,b) and an ENZ media (bottom,c). Phase variation is constant across the ENZ media and contributes to both forward and backward signal generation.

the structure experiences a much stronger light-matter interactions due to the slow group velocity [100, 101]. Fig. 3.5 contains calculated values of the group velocity of a Drude ENZ material ($\lambda_{ENZ} = 1420$ nm) with various damping coefficients. For the theoretical, loss-less ENZ material, the group velocity is exactly zero for wavelengths greater than the ENZ wavelength. This is consistent with the picture that light inside of an ideal ENZ material will have zero phase propagation and is essentially a static field. For realistic values of γ, the group velocity remains small but finite.

It should be noted that ENZ in homogeneous materials is not the only methods to achieve such effects [100, 101]. Additional approaches such as resonant cavities [102–104], photonic crystals [5,105,106], and waveguide modes near cutoff [23,107] can achieve similar enhancements to the light-matter-interaction by slowing the group velocity of light and/or confining light to small volumes. Moreover, it has recently

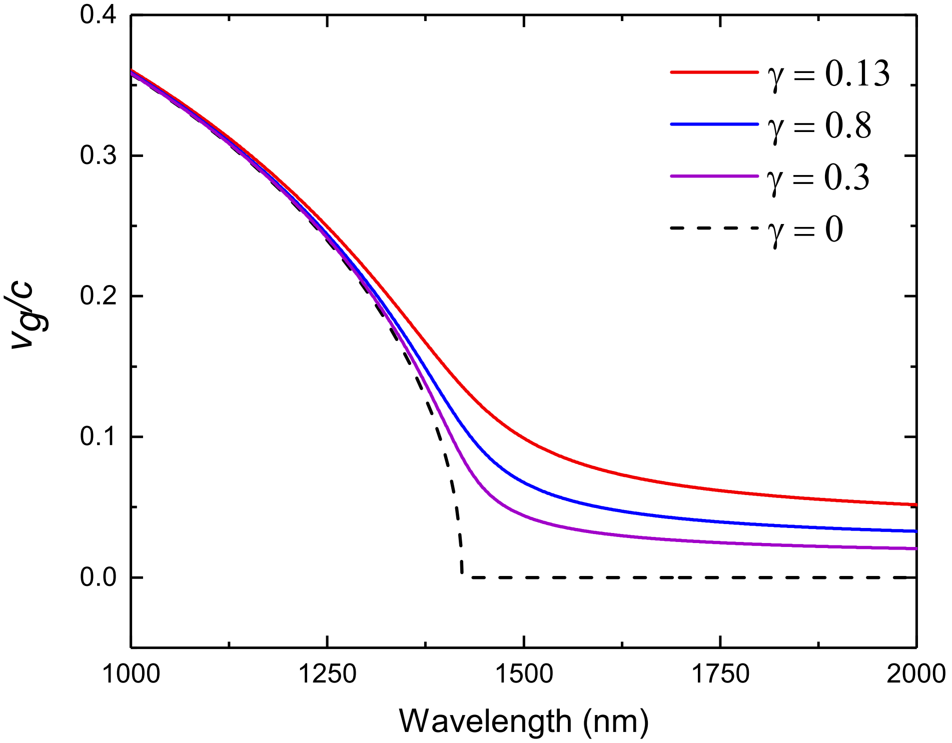

Figure 3.5. Group Velocity in an ENZ Material of $\gamma = 0, 0.3, 0.8,$ and 0.13 with $\lambda_{ENZ} = 1420$ nm. For all but the ideal ENZ material ($\gamma = 0$), the group velocity is small but finite for wavelengths greater than the ENZ wavelength.

been shown that random photonic structures can also produce strong light-matter-interactions [108, 109]. Although light does not physically slow down inside the random material, the multiple scattering events can be viewed as an effective reduction in the group velocity of the light passing through the material, thereby leading to stronger light-matter-interactions. From this perspective, ENZ materials can be viewed as a subset of a more general class of enhancement effects which achieve their impact through slow-light, and the optimal approach therefore depends upon the application and desired outcomes.

4. ULTRAFAST AND NONLINEAR OPTICS WITH TRANSPARENT CONDUCTING OXIDES

A portion of this chapter has been published in the journal Optica, *Optica* 2.7 (2015): 616-622., DOI: 10.1364/OPTICA.2.000616; the journal Nature Communications, *Nature Communications* 8 (2017): 15829., DOI: 10.1038/ncomms15829; and the journal Nano Letters, *Nano Letters* 18.2 (2018): 740-746., DOI: 10.1021/acs.nanolett.7b03919. u

The ideal nanophotonic switch has a large ratio of modulation amplitude to energy consumption (efficiency), which is sustainable at high frequencies (speed). In all-optical modulation platforms, these two pertinent features are difficult to achieve simultaneously because relaxation dynamics are slow in materials with large modulation, while materials with fast relaxation dynamics typically have inefficient modulation amplitudes. In this chapter, the performance of aluminum-doped zinc oxide near its epsilon-near-zero wavelength is evaluated for ultrafast modulation of nanophotonic and plasmonic applications. Due to the particular nature of this material's electronic bandstructure, we observe ultrafast (sub-picosecond) recombination for both interband and intraband pump wavelengths. Furthermore, we find the modulation amplitude of aluminum-doped zinc oxide is enhanced at the epsilon-near-zero wavelength. This enhancement occurs from an inherent inverse dependence of nonlinear interactions on the base refractive index and the static electric field properties for low refractive indices. Together, these two features make aluminum-doped zinc oxide and–in general–epsilon-near-zero transparent conducting oxides strong potential materials for efficient and ultrafast nanophotonic switches and, additionally, the exploration of novel nonlinear optics.

4.1 Ultrafast Optical Dynamics in Semiconductors and Metals

Carrier dynamics in semiconductors and metals are goverened by a plethora of processes including interband transitions, electron-electron and electron-phonon scattering, and nonradiative recombination [53,110]. These processes occur together, but the individual contribution to the overall transient optical modulation is dependent on the electronic and phononic bandstructure and the particular type of optical excitation and measurement energy. This dependence on optical "*pump*" excitation and "*probe*" measurement energies allows ultrafast optical characterization experiments to isolate particular processes and study their separate effects. In general, the pump energies are categorized as either *interband* or *intraband*. Interband refers to pump energies large enough to drive electrons across distinct bands, while intraband pumps only excite electrons within an individual band. The probe energy is selected in order to monitor particular electronic transitions.

For intrinsic, crystalline semiconductors (Si, GaAs, etc), the electronic structure is typically treated with either a direct or indirect parabolic band approximation, and the Fermi level is assumed to reside within the bandgap of the material so there is only a sufficient density of electrons inside the valence band. In this case, the electron transitions will only occur via interband (direct or indirect) transitions, meaning the pump energy is chosen to be greater than the semiconductor bandgap. Following optical pump excitation, the probe is selected to either probe electron population changes in the conduction band (low, intraband energies) or the valence band (large, interband energies). In either case, the recombination or relaxation of the electrons back to equilibrium will occur on the order of hundreds of picoseconds to several nanoseconds [111,112], which limits the all-optical switching frequencies to well-below conventional electronic switches.

An approach for increasing the recombination rates in semiconductors is the introduction of defect/trap/surface states [113–115]. For highly confined devices such as quantum wells and dots, interband and intersubband recombination can also result in extremely fast recombination times on the order of hundreds of femtoseconds to a few picoseconds [116–118]. An example of such methodologies is low-temperature grown GaAs, where various defect states are introduced into the crystalline structure. The presence of defects drastically decreases the recombination times due to the introduction of midgap states according to $\tau = (N_t \sigma v_{th})^{-1}$, where N_t is the trap density, σ is the capture cross-section, and v_{th} is the thermal velocity of carriers [112]. Recombination times on the order of 2 picoseconds have routinely been achieved with such materials [114, 115, 119]. Additional methods of introducing defects are possible, such as deep-level defects ($\tau \sim 50 - 100$ ps) [120], and ion bombardment ($\tau \sim 0.5 - 4$ ps) [121, 122]; however, these methods result in deterioration of optical (i.e. higher loss) and/or electronic (e.g. carrier mobility) properties, which is typically a detriment for nanophotonic applications.

Another example of reducing the recombination time is Auger processes [110]. which occurs in semiconductors under extreme free-carrier concentrations ($> 10^{-19}$ cm^{-3}). Recombination times as small as 100 fs have been achieved in silicon for a carrier density of 10^{-21} cm^{-3}, although the recombination rate was dependent on pump intensity and the nonradiative nature of the effects can lead to a significant thermal buildup, potentially limiting the speed of a device [123].

Ultrafast processes in metals are distinct from semiconductors since the carrier concentrations are much larger and changes in their optical properties arises from transitions near the Fermi surface [53, 124, 125]. After the excitation of an ultrafast optical pulse, metal electrons decay via either electron-electron or electron-phonon collisions. Electron-electron scattering is responsible for the formation of an incoherent population of highly nonthermal electrons and holes. The lifetime of these hot electrons is on the order of 1-100 fs, as can be calculated with Fermi liquid theory [126]

$$\tau_{e-e} = \frac{128}{\pi^2 \sqrt{3} \omega_p} \left(\frac{E_f}{E - E_f} \right)^2 \tag{4.1}$$

where E_f is the Fermi energy and ω_p is the plasma frequency. Because these time scales are less than or equal to the time resolution of most femtosecond laser sources, we will assume that their effect is unresolvable in experiments. Therefore, observed recombination rate is primarily due to the electron-phonon scattering. Given these assumptions, the electron-phonon thermalization can be accurately captured using a two-temperature model [127, 128]. This model (see Eq. 4.5 below) treats the electrons and the lattice as two thermal bodies which are allowed to exchange heat via a coupling factor, g, referred to as the electron-phonon coupling constant. Using this model, the electron-phonon coupling constant can be determined, which for small change in temperature, can be used to directly calculate the electron-phonon recombination rates. For noble metals such as gold, silver, and copper, these recombination rates are typically very fast ($\sim 1-10$ ps), but the total modulation amplitude is very small ($\sim 10^{-2} - 10^{-3}$) [125, 129, 130]

4.2 Refractive Index Modulation at Epsilon-Near-Zero

Modulation amplitude is equally important as ultrafast transient times for dynamic materials. However, a material's inherent refractive index change is often very weak and direct optical modulation is inefficient. To circumnavigate this problem, the dynamic material is often incorporated within a resonant system, such as an antenna or cavity, where the change in the system's transmission, reflection, or absorption is extremely sensitive to the dynamic material's optical properties. In this way, even a small change in the refractive index of the material will result in a large modulation of the total system's electromagnetic response. Here, we discuss the ability to enhance the modulation performance of aluminum-doped zinc oxide (Al:ZnO) films by operating near the film's ENZ wavelength where small changes to the Al:ZnO's refractive index results in large modulation amplitudes. As shown in Fig. 4.1, operating in the ENZ regime (i.e. n <1) produces larger absolute changes in the reflection for a fixed change in the refractive index ($\delta n = -0.1$ in a purely real ENZ media). This can be understood by considering the change in magnitude with respect to the initial index, e.g. a change of -0.1 for an initial index of 0.2 is 50%, while for an initial index of 2, the change is 2%. Consequently, this makes the ENZ regime an attractive region for maximizing the performance of modulators.

4.3 Pump Probe Experiments

To measure the ultrafast dynamics of Al:ZnO, we designed and constructed a femtosecond pump-probe spectroscopy [53] setup to provide both interband and intraband pumps and a variable near-infrared probe to measure the femtosecond changes in reflection $\Delta R(\Delta\tau, \lambda_{pr})/R_o$ and transmission $\Delta T(\Delta\tau, \lambda_{pr})/T_o$ (See Fig. 4.2a). Femtosecond pump and probe beams were produced using a chirped pulse amplifier seeded with a Ti:saphhire laser (Amplitude Technologies) which delivered up to 10 mJ energy pulses at a 787 nm central wavelength and 100 fs pulse duration. A fraction of the laser power was routed to a commercial optical parametric amplifier (OPA) (Topas, Light Conversion Ltd), which produced short (<120 fs) probe pulses tunable between 1100 and 2600 nm. The s-polarized probe beam was spatially filtered, reduced in energy with a neutral density filter, and focused by a 250 mm focal length lens onto the sample surface at a small angle of incidence ($< 10°$). The probe beam waist on the sample was measured using a knife-edge technique and was found to be 65 μm. The probe intensity in the focus was found to be 200 MW/cm^2, determined by measuring the pulse energy and duration at the sample plane. The probe pulse delay from the pump pulses was set by a computer-controlled linear translation stage (M-VP-25XA, Newport), equipped with a gold-coated hollow retroreflector (PLX Inc.). Interband pulses of wavelength (262 nm) were generated by pumping a third-harmonic generation set-up (Femtokit, Eskma Optics) with $\approx$1 mJ of the 787

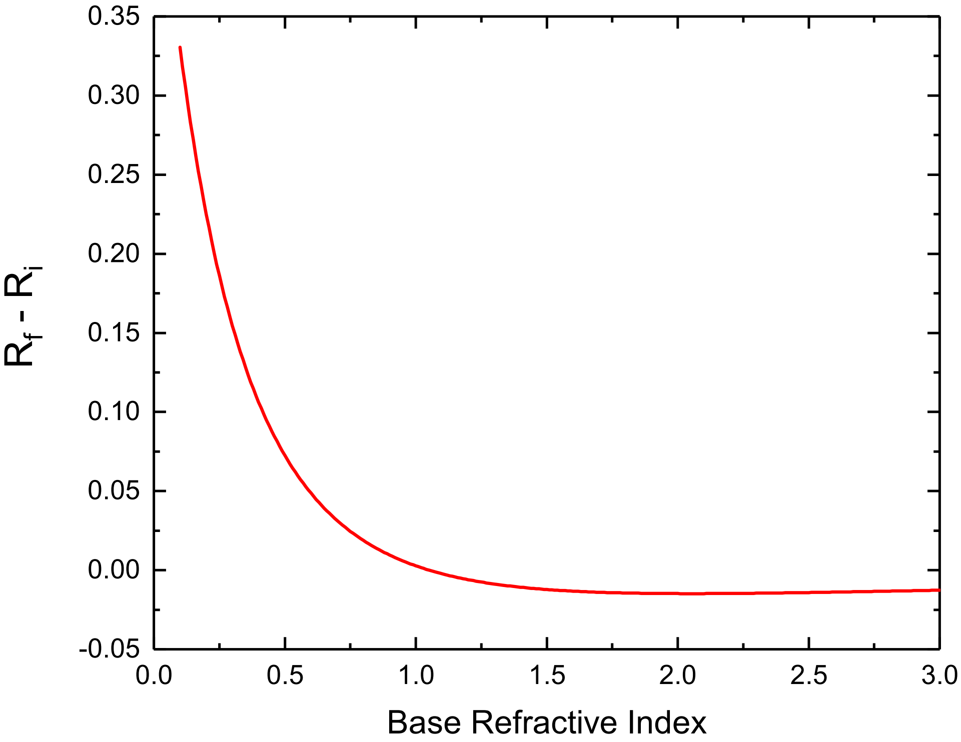

Figure 4.1. Modulation of an Epsilon-Near-Zero Material. Absolute change in the reflection of a purley real ($Img\left[n\right] = 0$) material versus base refractive index provided an index change of $\delta n = -0.1$. The magnitude of the reflection coefficients are calculated using Fresnel's equations at a single interface between air ($n_0 = 1$) and the material assuming normal incidence. Note that operating in the epsilon-near-zero regime (i.e. $n < 1$) provides larger absolute changes in the reflection for the same change in refractive index.

nm beam. The 200 μJ, ≈65 fs, 262 nm ultraviolet pump was spectrally filtered from the 787 nm beam using four dichroic mirrors (HR at 266 nm, HT at 400 and 800 nm, Layertec GmbH). The s-polarized ultraviolet pulse was focused at normal incidence with a 250 mm focal length CaF_2 lens. The beam size measured with knife-edge was 400 μm. The ultraviolet energy was controlled by rotating the half-waveplate at the input of the third-harmonic generation setup. The near-infrared pump was obtained by splitting a portion of the laser beam and delaying it from the ultraviolet pulse using a computer-controlled linear translation stage (M-VP-25XA, Newport), equipped with a silver-coated hollow retroreflector (PLX Inc.). The s-polarized near-infrared pump was focused at normal incidence onto the sample plane. A dichroic mirror (HR at 266 nm, HT at 800 nm, Layertec GmbH) was employed for combining the two pump pulses. The beam waist of the near-infrared pump was measured to be 210 μm using the knife-edge technique. The pulse energy was controlled with a waveplate in front of a thin-film polarizer (Altechna). The ultraviolet, near-infrared, and probe energies were measured with a thermopile detector (XPL12, Gentec-EO). The reflected and transmitted signals were recorded with amplified Germanium photodetectors (PDA50B-EC, Thorlabs).

Our sample consisted of a 900 nm of Al:ZnO deposited onto a 1-mm-thick silica substrate. The films were deposited using pulsed laser deposition (PVD Products Inc.) operating at a wavelength of 248 nm for source material ablation. A 2wt% doped Al:ZnO target was purchased from the Kurt J. Lesker Corp. with a purity of 99.99% or higher. The energy density of the 248 nm ablation laser at the target surface was maintained at 1.5 J cm^{-2} and the deposition temperature was 75 °C. We maintained the oxygen pressure under 0.01 mTorr to achieve additional free carrier concentrations due to the oxygen defects. The prepared thin films were characterized by spectroscopic ellipsometry (J.A. Woollam Co. Inc.) in the spectral range of 200 to 2500 nm. The dielectric permittivity of the Al:ZnO was retrieved by fitting a Drude+Lorentz oscillator model to the ellipsometry data. The optical properties of at 262 nm were estimated from a spline extrapolation of the measured properties combined with bounds provided by data from similar films [131]. To probe the electrical properties of thin films, such as mobility and carrier concentration, we carried out Hall measurements (MMR Technologies) at room temperature. From ellipsometry data, we found our film to have an ENZ wavelength of $\lambda_{ENZ} = 1300$ nm. To probe the ultrafast response of the Al:ZnO film at this wavelength, we tuned our OPA to generate $\lambda_{pr} \approx 1300$ nm laser pulses.

4.3.1 Interband Dynamics

To elucidate the interband (conduction to valence) recombination in Al:ZnO, we blocked the near-infrared 787 nm pump and set the ultraviolet $\lambda_{pu} = 262$ nm pump to a fluence of $F_{ultraviolet} \approx 5$ mJ cm^{-2} at the Al:ZnO surface. We then measure the transient change of transmission $\Delta T(\Delta\tau)/T_o$ and reflection $\Delta R(\Delta\tau)/R_o$ as a function of the pump-probe delay time $\Delta\tau$. The normalized and percent change in the transmission are shown in Fig. 4.2b. Using a single exponential fit, we find the recombination time is approximately 600 fs and the modulation amplitude is nearly 45%. The inset of Fig. 4.2b is a schematic illustration of the interband dynamics: ultraviolet light of energy $E_{ultraviolet}$ generates electrons and holes (δ_n, δ_p, respectively) above the Fermi level (E_f) in addition to the initial conduction electron population ()N_i), which then recombine to either valence states or trap states (N_t).

We model the interband dynamics and relaxation by considering the total change in transmission as a linearized function of the change in real ($\Delta\epsilon'$) and imaginary ($\Delta\epsilon''$) portions of the film's permittivity [53, 130, 132],

$$\frac{\Delta T}{T_o} = \frac{\partial \ln(T)}{\partial \epsilon'}\Delta\epsilon' + \frac{\partial \ln(T)}{\partial \epsilon''}\Delta\epsilon'' \tag{4.2}$$

. In Eq. 4.2, we define the derivatives to be taken at the unperturbed permittivity of the film ($\epsilon_i = \epsilon_i' + i\epsilon_i''$) and assume a small, linear change in the dielectric permittivity $\epsilon = \epsilon_i + \Delta\epsilon$, which valid within our experimental conditions [132]. Although we have only considered changes in transmission, Eq. 4.2 is equally valid for changes in reflection. The linear change in the real and imaginary permittivity is related to the photoexcited electron δ_n and hole δ_p density by,

$$\Delta\epsilon(\delta_n, \delta_p) = \frac{e^2}{m_n^* m_o \epsilon_o}\frac{(N_i + \delta_n)}{\omega^2 + i\gamma_n\omega} + \frac{e^2}{m_p^* m_o \epsilon_o}\frac{(P_i + \delta_p)}{\omega^2 + i\gamma_p\omega} \tag{4.3}$$

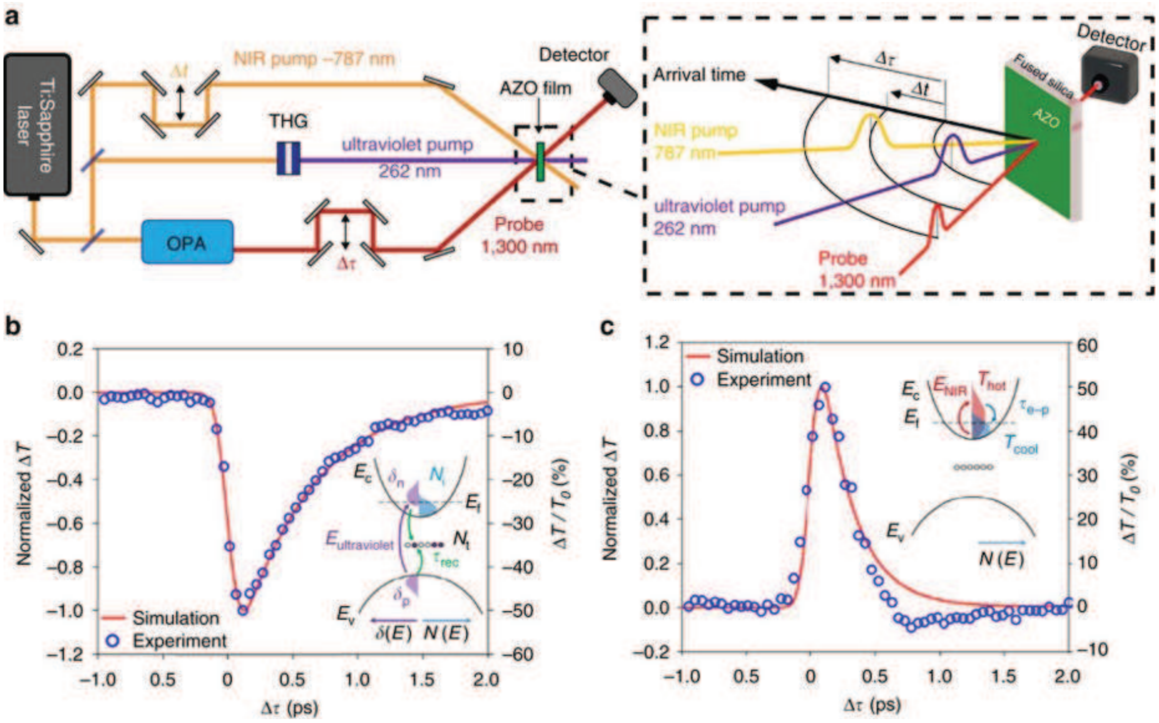

Figure 4.2. Two-color Pump Probe Experiment. (a) Schematic of the two-color pumpprobe experimental set-up where the two pump wavelengths, 787 nm (NIR) and 262 nm (ultraviolet), are illustrated along with the probe wavelength of 1,300 nm. The delay between the two pump pulses is denoted Δt while the delay between the probe and ultraviolet signal is denoted $\Delta\tau$. For intraband excitation using only the NIR pump, Δt is defined as the delay between the probe and NIR pump pulse arrival time. The black arcs indicate the arrival time of the pulses. (b) Change in transmission at 1300 nm versus the pumpprobe delay $\Delta\tau$ under 262 nm excitation fitted with simulation. The inset illustrates the process diagram for interband excitation: ultraviolet light ($E_{ultraviolet}$) generates electron-hole pairs (δ_n, δ_p) above the Fermi level (E_f) in addition to the intinsic concentration (N_i), which recombine through mid-gap trap states (N_t, τ_r). (c) Change in transmission at 1300 nm versus the pumpprobe delay $\Delta\tau$ under 787 nm excitation fitted with simulation. The inset illustrates the process diagram for intraband excitation: NIR light (E_{NIR}) raises the temperature of conduction band electrons ($T_{cool} \rightarrow T_{hot}$), which relax through scattering processes (τ_{e-p}), heating the lattice.

where N_o and P_o are the electron and hole initial densities, respectively, $m^*_{n(p)}$ is the effective mass of the electrons(holes) obtained with Hall measurements, $\gamma_{n(p)} = e(m^*_{n(p)} m_o \mu_{n(p)})^{-1}$ is the loss factor of electrons(holes) with $\mu_{n(p)}$ being the mobilities, e is the electron charge, m_o the electron mass, and ϵ_o the permittivity of free space. Due to the high intrinsic carrier concentration of the Al:ZnO, we take $P_o = 0$. The effective mass and mobility of holes were taken from literature as $m^*_p = 0.59$ [133] and $\mu_p = 30$ cm^2 V^{-1} s^{-1} [134].

To find the photoinduced electron and hole population dynamics, we use a standard Transfer Matrix Method (TMM) to calculate the local absorption $\alpha(z)$ of the pump as a function of sample thickness z [135,136]. This value is then used to calculate the initial spatial distribution of electrons and holes, which can then be multiplied by temporal convolution of the temporal response of the pump pulse with the single exponential relaxation function of the material [53],

$$\delta_{n,p}(z,t) = (1-R)F_o\alpha(z)\left[1 - erf\left(\frac{w}{2\tau_1} + \frac{t}{w}\right)\right] e^{-t/\tau_1}. \tag{4.4}$$

The terms in Eq. 4.4 are the reflectivity of the unpumped Al:ZnO R, the laser fluence F_o, the recombination time extracted from our exponential fit τ_1, and the cross-correlation width of the pump and probe pulses $w = \tau_{FWHM}(2\ln 2)^{-1/2}$; here, $erf()$ is the error function. Our model is exact in the sense that there are no fitting parameters. We then numerically calculate the linear change in transmission by inserting Eqs. 4.3–4.4 into Eq. 4.2 and calculating the derivatives numerically. The red line in Fig. 4.2b shows the results of our model, which shows excellent agreement with the experimental values (blue circles).

4.3.2 Intraband Dynamics

Having measured the interband relaxation dynamics of our Al:ZnO film and developed an accurate numerical model of the photoexcited carriers, we now focus on the intraband dynamics. Proceeding in a similar fashion as interband pumping, we block the ultraviolet pump and set the near-infrared $\lambda_{pr} = 787$ nm pump to a fluence of $F_{NIR} \approx 16$ mJ cm^{-2} at the Al:ZnO surface. The differential reflection and transmission are then measured as a function of the near-infrared pump and probe delay $\Delta\tau$ (see Fig. 4.2a). We find a relaxation time of approximately 100 fs from single exponential decay fits of the transient signal, which is significantly faster compared with interband pumping. Again, the inset of Fig. 4.2c shows a pictorial depiction of the intraband dynamics: (1) near-infrared light of energy E_{NIR} raises the conduction electron temperature ($T_e^{cool} \rightarrow T_e^{hot}$) via free-electron absorption; for experimental time scales longer than the electron-electron scattering time ($\tau_{e-e} \sim 1 - 10$ fs), the thermalized excited electron population is accurately described using a Fermi-Dirac distribution; (2) the electrons then relax through electron-phonon scattering processes (τ_{e-p}) and heat the lattice to temperature T_l.

We model the relaxation of the thermal conduction electrons with a two-temperature model (TTM), whereby the change in the electron temperature and lattice temperature are captured as a function of time for the material. Generally, the response is described by

$$C_e(T_e)\frac{\partial T_e}{\partial t} = \frac{\partial}{\partial z}(\kappa\frac{\partial T_e}{\partial z}) - G(T_e - T_l) + H \tag{4.5}$$

$$C_e(T_l)\frac{\partial T_l}{\partial t} = G(T_e - T_l) \tag{4.6}$$

where C_e is the volumetric heat capacity of electrons, C_l is the volumetric heat capacity of the lattice ($C_l = 2.8 \times 10^6$ J m^{-3} K^{-1}) [137], κ is the thermal conductivity ($\kappa = 100$ W m^{-1} K^{-1}) [137], and G is the electron-phonon couling constant; H is the source term, given by

$$H(z,t) = 0.94J\frac{1-R-T}{w(\delta+\delta_b)}\frac{exp\left[-\frac{z}{\delta+\delta_b} - 2.77\left(\frac{t}{w}^2\right)\right]}{1-exp\left[-\frac{d}{\delta+\delta_b}\right]} \tag{4.7}$$

wher R is the reflectivity of the sample, T is the transmissivity of the sample, J is the excitation intensity, δ is the skin depth of the pump, δ_b is the ballistic range of electrons, w is the pump-probe cross-correlation width, and d is the sample thickness [138]. This coupled set of equations is solved numerically using the *pdepe*() built-in function of MATLAB assuming a ballistic range of hot electrons of 1 nm. For metals such as gold, this value is $\approx$ 100 nm, however, our films have a large density of defects and grain boundaries so we expect a significantly smaller value for Al:ZnO.

The electron heat capacity relates the resulting linear change of the electron temperature with the increase in electron energy density (ΔU_e), i.e. $\Delta T_e = C_e(T_e)^{-1}\Delta U_e$, and was calculated as [139]

$$C_e(T) = \frac{1}{2}\pi^2 N_i k_b \frac{T}{T_F} \tag{4.8}$$

where N_i is the intrinsic electron density ($N = 1 \times 10^{21}$ cm^{-3}), k_b is Boltzmann's constant, T is the equilibrium temperature, and T_F is the Fermi temperature (1.16×10^4 K) [140]. We calculate a value of $C_e = 3500$ J m^{-3} K^{-1}. This value is two orders of magnitude less than elemental metals such as Al, Cu, Ag, Au, Ni, Pt, W, and Ti [141]. The small heat capacity of Al:ZnO compared with standard metals is the result of the low carrier concentration of free electrons and small Fermi temperature. The low heat capacity is one reason why we observe such large changes in the probe signal compared with metals and metal-like materials [77, 142]; the electron temperature change per change in electron energy density (due to pump absorption) is large for small heat capacities, which results in a large modification of the optical constant.

The resulting change in optical properties was modeled using an effective thermal dependent complex index, n_{th}, such that $\Delta n_{Al:ZnO} = (\Delta T_e + \Delta T_l)\, n_{th}$. The TMM was used to determine the change in optical properties of the graded index materials (as described above). The reflection and transmission of the sample were normalized and the rate was fitted to extract the electron-phonon coupling constant and found to be $G \approx 14 \times 10^{15}$ W m^{-3} K^{-1}. After the normalization procedure, only the sign of the complex effective thermal index is relevant, and it was found that the extinction coefficient decreased while the index increased (i.e. $n_{th} > 0$ and $n_{th} < 0$) matching the effect observed in experiments. The fit of the transient intraband signal is shown in Fig. 4.2c as the solid red line.

4.3.3 Controlling Hybrid Nonlinearities

The observed co-existence of both intraband and interband nonlinearities suggests the possibility of achieving new dynamic functionalities through their combined effect and if these two excitation regimes are independent, the corresponding effects can be algebraically combined. We therefore performed a thorough investigation of the AZO optical response under combined ultraviolet and NIR excitation as a function of the relative delay Δt between the two pumps and $\Delta\tau$ between the pumps and the probe (the ultraviolet pump signal is used as the time reference). From the recorded probe reflection and transmission as a function of the two delays, $R_p(\Delta t, \Delta\tau)$ and $T_p(\Delta t, \Delta\tau)$, respectively, we retrieve the real and imaginary refractive index of the film using a transfer matrix approach, as described in [143]. The extracted values are shown in Fig. 4.3, where the time-dependent relative change in the real (Fig. 4.3a-e) and imaginary (Fig. 4.3f-j) refractive index of the AZO film at 1300 nm is shown, for five values of the NIRultraviolet pump pulse delay, between $\Delta t = -1.7$ ps and $\Delta t = 1.8$ ps. The results in Fig. 4.3 are achieved with optical pump fluences of $F_{ultraviolet} = 5$ mJ cm^{-2} and $F_{NIR} = 14$ mJ cm^{-2}.

Our measurements demonstrate that the temporal dynamics of AZO film properties, such as reflection and transmission, or equivalently the real and imaginary part of the refractive index, can be optically controlled via a two-color excitation scheme. This is enabled by the independence of the two nonlinear processes responsible for the modulation of the material properties. This independence is demonstrated by the good match of the red and the black dashed curves in Fig. 4.3. The former are obtained from the measurements with simultaneous ultraviolet and NIR excitation while the latter are generated by the algebraic addition of the time-dependent refractive index changes induced by the ultraviolet and NIR pumps independently. It is worth mentioning that all the experiments are performed in a condition of balanced excitation, meaning that the adopted fluences for ultraviolet and NIR pumping were set in such a way to produce similar alterations (in amplitude but not in sign) on

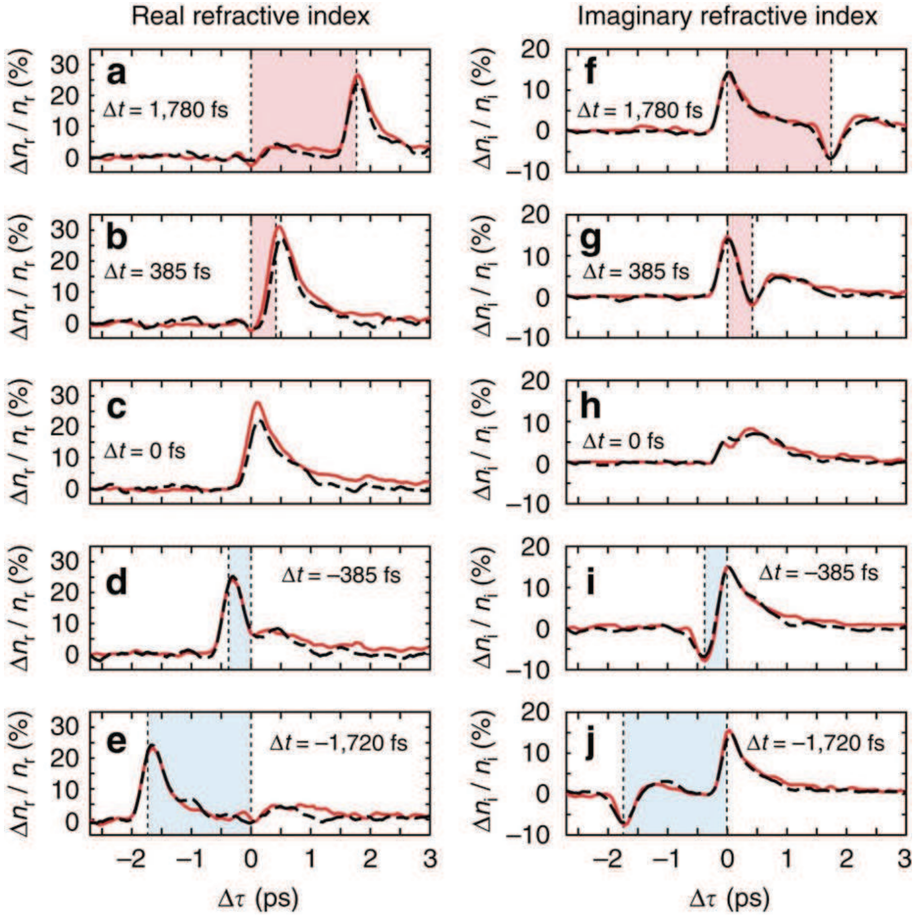

Figure 4.3. Dynamic Change in the Optical Response of AZO Thin Films Triggered by Two-Color Excitation. Percent change of the real (a-e) and imaginary (f-j) part of the refractive index as a function of the delay $\Delta\tau$ between the ultraviolet pump and the infrared probe pulses. Multiple vertical plots are shown, for different delay Δt between the ultraviolet and the NIR pump pulses. Shaded areas indicate whether the ultraviolet pump, which is used as time reference, precedes (light blue) or follows (light red) the NIR pump. Overlapping the results obtained by simultaneous two-colour pumping (red curves), we plot the computed change in refractive index calculated by the algebraic summation of the results obtained from experiments with separate ultraviolet and NIR pump pulses (black dashed curves). The probe, the NIR, and the ultraviolet pump wavelengths were set to 1300 nm, 787 nm, and 262 nm, respectively. The probe intesntiy was low: $I_p \approx 5$ mJ cm^{-2}, while the pump fluences were $F_{ultraviolet} = 5$ mJ cm^{-2} and $F_{NIR} = 14$ mJ cm^{-2}

the transmitted power. Operatively speaking, we first arbitrarily choose a fluence for the ultraviolet beam while the NIR pump fluence is set afterwards, to induce a change on the transmitted power of the same magnitude as that obtained with the ultraviolet pump. Such a change saturates for both ultraviolet ($\Delta T/T_o \approx 75\%$ at $F_{ultraviolet} \approx 15$mJ cm^{-2}) and NIR ($\Delta T/T_o \approx 100\%$ at $F_{NIR} \approx 60$mJ cm^{-2}).

While cross-coupling between interband and intraband effects is negligible at the pump fluences used in these experiments, we observed that it becomes appreciable for higher fluences. To evaluate the impact of crosstalk, we calculate the relative difference between the measured (me) and ideal (id) change in the real and imaginary refractive index $D_{r,i} = |n^{me}_{r,i} - n^{id}_{r,i}|/n^{id}_{r,i}$ for increasing pump fluences. In the case, 'measured' refers to the refractive index with the simultaneous pumping scheme while ideal refers to the algebraic sum of the refractive indices retrieved with independent ultraviolet and NIR excitations. In the experimental conditions of Fig. 4.3, we estimate $D_r \leq 6\%$ and $D_i \leq 3\%$, whereas at higher pump fluences $F_{ultraviolet} = 24$mJ cm^{-2} we observe stronger crosstalk: $D_r \leq 22\%$ and $D_i \leq 7\%$.

4.3.4 Modulation Bandwidth and Wavelength Control

The ability to optically control the AZO properties with nonlinear effects of similar amplitude yet opposite sign paves the way to intriguing applications. In Fig. 4.4, we show two new effects enabled by the two-color AZO modulation. The first, in Fig. 4.4a,b, is the dynamic control of the optical modulation bandwidth of the AZO film, while the second, in Fig. 4.4c,d, is the dynamic control of the transmitted probe wavelength.

All-optical modulation of infrared radiation is relevant to the development of future telecommunications and data networks technologies [144–146]. Fig. 4.4a shows the change in T of the AZO film pumped by both ultraviolet and NIR light, resolved as a function of the inter-pump delay Δt and the pumpprobe delay $\Delta\tau$. The effect of the ultraviolet pump is to reduce the transmission (the horizontal blue and purple band), while the effect of the NIR pump is to increase the transmission (the diagonal, green-to-red band). Performing the Fourier transform along the vertical direction provides the modulation bandwidth of the optically excited film as a function of the inter-pump delay Δt and is shown in Fig. 4.4b. The blue and red dashed lines indicate the bandwidth (rms) obtained by only ultraviolet and only NIR pump, respectively. The faster dynamic of the intraband (≈1.7 THz) compared to the interband (≈1.55 THz) nonlinearity is clear. The proposed two-color pump configuration remarkably allows one to modify the modulation bandwidth of the film via the delay of the two pump fields, as shown by the black curve in Fig. 4.4b. This enables the observation of a fast oscillation between a reduction (≈0.75 THz at $\Delta t = 0$) and an increase (≈2 THz at Δt≈130 fs) of the bandwidth, although with a fourfold reduction in the modulation depth compared to larger delays. Further, we show how the probe wavelength can be dynamically modified by a combination of the two ultraviolet and NIR pump pulses. In Fig. 4.4c, we show the change in the central wavelength of the $\lambda_{pr} = 1300$ nm probe pulse, recorded with an InGaAs spectrometer, as a function of both Δt and $\Delta\tau$ and for pump fluences $F_{ultraviolet} = 22$ mJ cm^{-2} and $F_{NIR} = 42$ mJ cm^{-2}. We note that the wavelength shift induced by the ultraviolet pump is negative, while the NIR pump gives both a positive and negative shift, depending on the delay with the probe. Fig. 4.4d shows the maximum positive ($\Delta\lambda_+$) and negative ($\Delta\lambda_-$) frequency shift induced by the ultraviolet and NIR pumps alone (blue and red curves, respectively) and combined (black curves). Interestingly, the wavelength shift induced by the two independent excitation mechanisms can also be algebraically added. Therefore, for a specific choice of the pump fluences, the wavelength shift is almost canceled when the two pump pulses are temporally overlapped. We note that, for higher pump fluences, wavelength shifts exceeding the pulse bandwidth can be achieved.

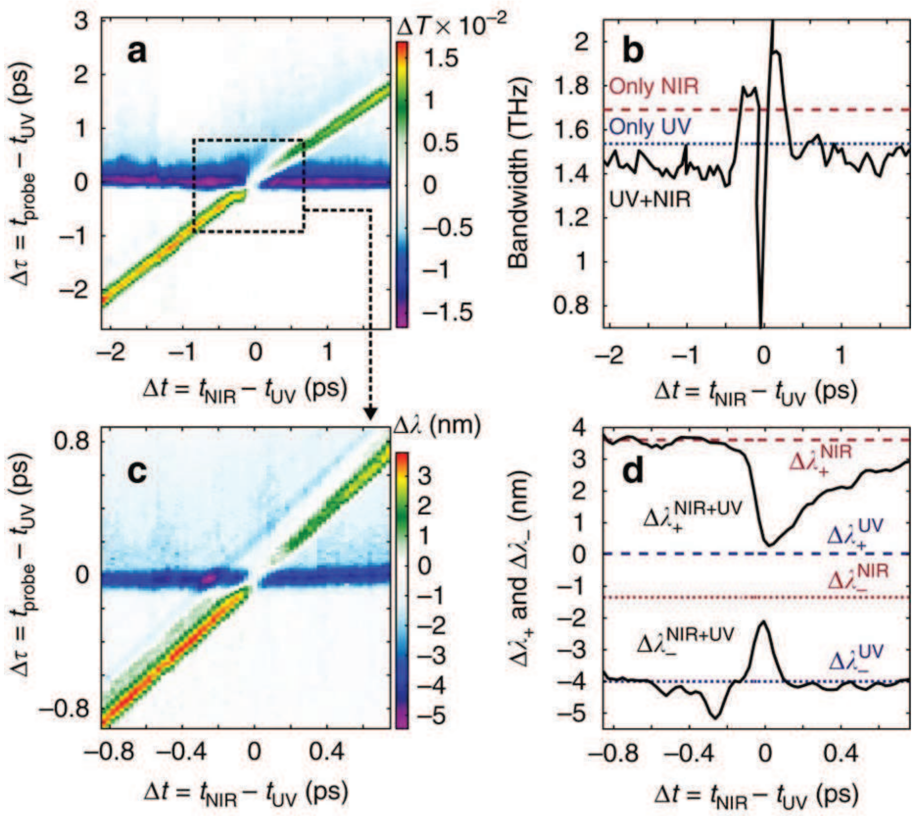

Figure 4.4. Two-Color Pumping Effects. (a) Change in the probe pulse transmission as a function of the pumpprobe delay ($\Delta\tau$) and the inter pumpdelay (Δt). The ultraviolet (UV) pump decreases the transmission, whereas the NIR increases it. The combined effect produces a Δt-dependent modulation. The modulation bandwidth is evaluated by performing a Fourier transform along $\Delta\tau$, and is shown by the black curve in (b). For delays close to $\Delta t = 0$, the modulation bandwidth can be decreased or increased by the two-colour combined effect. The blue and red dashed lines show the bandwidth of the ultraviolet-only and NIR-only driven modulation. (c) Measured central wavelength shift of the transmitted probe pulse ($\approx$ 15 nm bandwidth) in a zoomed $\Delta t - \Delta\tau$ region (square box in a). The ultraviolet pump blue shifts the probe wavelength, whereas the NIR pump does the opposite. At $\Delta t \approx 0$, the opposite effects almost entirely cancel the wavelength shift. (d) Summary of the findings in c, showing the maximum positive ($\Delta\lambda_+$) and negative ($\Delta\lambda_-$) wavelength shift for the NIR-only (red-dashed/dotted), ultraviolet only (blue-dashed/dotted) and two-color (solid black) Al:ZnO excitation.

4.4 Dynamic Control of Nanocavities with Transparent Conducting Oxides

We have shown that all-optical modulation of TCO films near their ENZ wavelength provides ultrafast control and large modulation performance, making them promising material platforms for dynamic control of nanophotonic devices. Indeed, optical tuning of TCOs triggered by photoexcitations has been successfully demonstrated with various geometries and material and incorporated in plasmonic systems [77, 81, 142, 147].However, a practical approach to design actively tunable devices by adopting metal oxides into conventional nanophotonic devices has not been reported yet.

Here, we demonstrate all-optical tuning of a metal nanocavity embedded with a TCO thin film (thickness $< \lambda/17$) to achieve the ultrafast spectral tuning of a Fabry–Pérot (FP) resonance in the NIR excited near the ENZ wavelength. Metal-insulatormetal(MIM) configurations have been extensively studied in photonics and plasmonics due to their strong light-matter interaction within subwavelength dimensions [148, 149]. Simple design and ease of fabrication make MIM structures common in nanophotonics, yet dynamic tuning of MIM-based devices has not been demonstrated. Although electrically driven active absorption tuning in the mid-infrared has been accomplished with ITO embedded MIM metafilms, the demonstrated switching speed was limited by the device capacitance [150]. As we have shown, intraband pumping of TCOs offers large (>2.5 THz) switching speeds and efficient optical modulation compared with electrical control. We observe that Fabry–Pérot resonance in an optical cavity can be transiently red-shifted to enable ON/OFF modulation of the transmitted signal up to 80%. Our work could enable actively controllable devices for beam steering, adaptive color filtering, and dynamic polarization rotation by using a set of diverse resonance modes in MIM configurations at subwavelength scales.

4.4.1 Nanocavity Fabrication and Design

A schematic of the TCO-based cavity is shown in Fig. 4.5a. Samples were fabricated as follows: 1) we deposited 25 nm of silver, followed by 25 nm of Al_2O_3 on a glass substrate by electron beam evaporation; 2) a 70-nm-thick Ga:ZnO film was then deposited using pulsed laser deposition followed by 205 nm of Al_2O_3; finally, we deposited a 24 nm silver film as a top layer with a protective 30-nm-thick alumina cap. Optical properties of the Ga:ZnO layer were obtained using spectroscopic ellipsometry as described earlier for Al:ZnO. The choice of Al_2O_3 and Ga:ZnO thicknesses was guided by FP calculations and numerical transmission simulations (COMSOL) of the nanocavity. In general, a static nanocavity composed of two reflecting surfaces

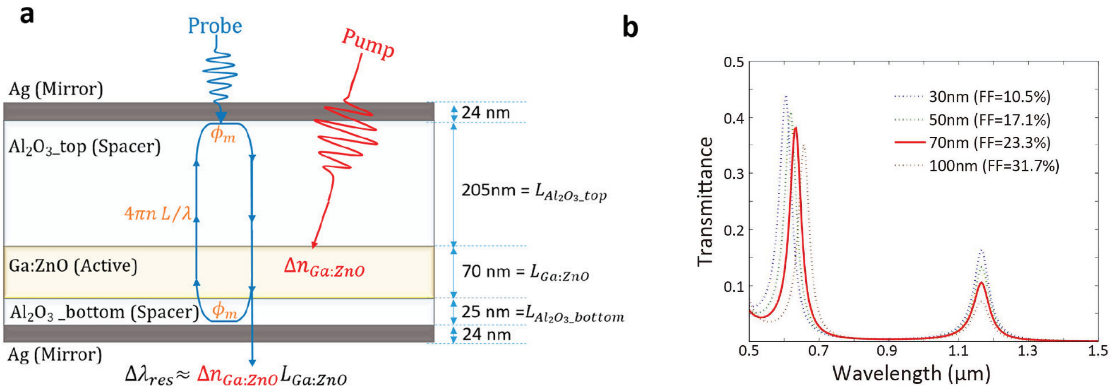
a
Probe
Pump
Ag (Mirror)
ϕ_m
Al_2O_3_top (Spacer)
$4\pi n L/\lambda$
Ga:ZnO (Active)
$\Delta n_{Ga:ZnO}$
Al_2O_3 _bottom (Spacer)
ϕ_m
Ag (Mirror)
24 nm
205nm = $L_{Al_2O_3\_top}$
70 nm = $L_{Ga:ZnO}$
25 nm = $L_{Al_2O_3\_bottom}$
24 nm
$\Delta\lambda_{res} \approx \Delta n_{Ga:ZnO} L_{Ga:ZnO}$
b
Transmittance
0.5
0.4
0.3
0.2
0.1
30nm (FF=10.5%)
50nm (FF=17.1%)
70nm (FF=23.3%)
100nm (FF=31.7%)
0.5
0.7
0.9
1.1
1.3
1.5
Wavelength (μm)

Figure 4.5. Active Nanocavity Design. (a) Cross-sectional schematic of the Ga:ZnO embedded nanocavity. The thickness of both top and botom silver mirror is 24 nm; the total thickness of alumina is 230 nm; and the thickness of Ga:ZnO is 70 nm. The reflection phase-shift from the metal mirrors (ϕ_m) and the phase accumulated throughout the cavity ($4\pi nL/\lambda$) is indicated. (b) Analytic transmittance of the nanocavity for several Ga:ZnO filling fractions (FF $= L_{Ga:ZnO}/\left(L_{Ga:ZnO} + L_{Al_2O_3}\right)$). The first-order resonance of the cavity occurs at a wavelength of 1200 nm for all FF, but the total transmittance decreases for larger FF due to the Ga:ZnO losses. The red line indicates the optimal FF choice considering both total transmittance and modulation performance.

separated by a dielectric spacer of thickness L and refractive index n will support FP resonances under the condition

$$4\pi nL/\lambda + 2\phi \approx 2m\pi \tag{4.9}$$

where ϕ is the reflection phase shift of the silver-Al_2O_3 interface (calculated from Fresnel equations), λ is the effective wavelength in Al_2O_3, and m is the resonance order. To enhance the modulation of the nanocavity, we want our resonances close to the ENZ wavelength of the Ga:ZnO film ($\approx$ 1200 nm), so we solve Eq. 4.9 for the thickness of the cavity to find $L = 300$ nm. Incorporating the active Ga:ZnO material into the nanocavity is a careful balance of loss to modulations: thick Ga:ZnO films provide larger modulation, but at the detriment of total transmission. Fig. 4.5b is a transmission plot of the nanocavity for several Ga:ZnO filling fractions (FF = $L_{Ga:ZnO}/\left(L_{Ga:ZnO} + L_{Al_2O_3}\right)$). The introduction of the Ga:ZnO layer slightly shifts the FP resonance to 1.16 μm, and for larger thickness, we observe a decrease in the total transmission amplitude. We estimate the total resonance shift of the active cavity with $\Delta n_{Ga:ZnO} L_{Ga:ZnO}$, where $\Delta n_{Ga:ZnO}$ is an induced change in the refractive index of Ga:ZnO and $L_{Ga:ZnO}$ is the Ga:ZnO thickness. Based on our previous calculations of the total refractive index shifts in Al:ZnO, we find the optimal modulation of the nanocavity occurs for a $L_{Ga:ZnO} = 70$ nm, as highlighted with a solid red line in Fig. 4.5b.

4.4.2 Dynamic Modulation with Intraband Pump

We investigate the tunability of our devices using a pump-probe setup as depicted in Fig. 4.6a. The setup is the same as in the previous experiments, except both pump and probe were generated using the OPA and had a spectral range of 1160–1600 nm. Initially, the setup was calibrated against the acquired ellipsometry data for the linear case (no pump). For calibration purposes, transmission spectra were recorded for different pulse wavelengths using a Czerny-Turner spectrograph (Andor Shamrock 163 Imaging Spectrograph coupled with an iDus InGaAs detector array). All the acquired curves were then fit with Lorentzian functions whose peaks were finally used to draw the device resonances which were approximated by a Gaussian curve as depicted in the Fig. 4.5b. The characteristic resonances recorded via the two described processes (i.e., ellipsometry and direct transmission of the tuned probe) were the same in within the experimental error. Fig. 4.5c reports the transmission spectra with (dashed blue line) and without (solid orange line) optical pumping for the cavity inclusive of the Ga:ZnO layer. As it is evident from Fig. 4.5c an appreciable spectral shift of the cavity resonance was apparent for the device with the Ga:ZnO layer. Similar pump-probe studies were conducted on a nanocavity without a Ga:ZnO layer, but spectral shift was observed. This indicates that the photoinduced carrier effects in the Ag mirrors and/or alumina spacer were not enough to induce the resonance shift under the same condition of intraband excitation of Ga:ZnO; hence, the induced red shift in resonance of the nanocavity results from the carrier dynamics of the Ga:ZnO film and not from the Ag nor alumina components. Even though the absolute value of the induced frequency shift is not large if compared to the resonance line width, it is still enough for enabling a remarkable signal modulation when operating in the linear region (see λ_o point in Fig. 4.5c). At this operational wavelength ($\lambda_o = 1200$ nm) even a small frequency shift can produce a substantial change in transmitted power (see green arrows in Fig. 4.5c). To record such a modulation and acquire more insights about its nature, we performed a standard degenerate pump and probe experiment at λ_o= 1200 nm. The signal transmitted through the sample was recorded as a function of the time delay $\Delta\tau$ between pump and probe. The normalized transient transmission is plotted as a function of $\Delta\tau$ in Fig. 4.6a, where three regions can be identified. The first two regions (labeled as "excitation" and "modulation" regions) are equally short and account for an overall ON/OFF time of approximately 400 fs. A third range, named "thermal" region, is also identified. As shown by the solid pink curves in Fig. 4.6a, the intraband material responses can be successfully modeled using the TTM (Eq. 4.5) as described earlier. The decay rate $\Delta T/T_o$ was fitted with a single exponential decay to extract the electron-phonon relaxation rate (τ_{e-p})

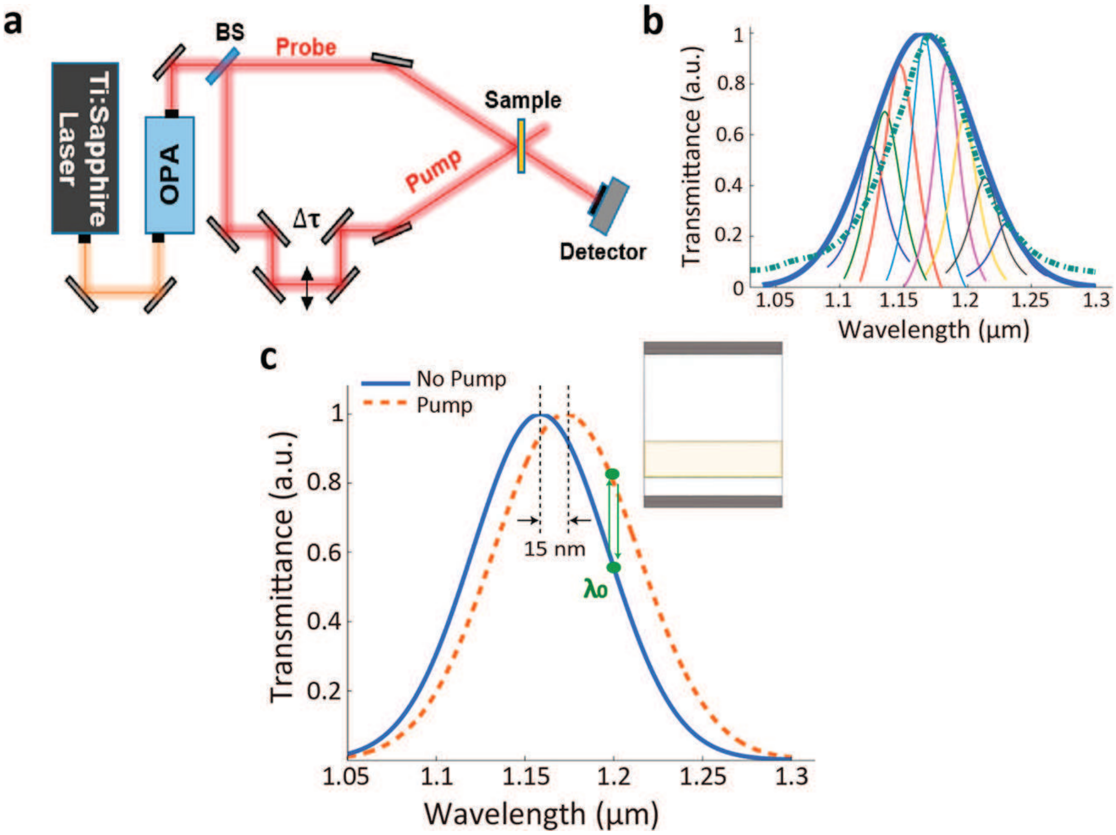

Figure 4.6. Ultrafast Modulation of the Nanocavity. (a) Pump-probe setup. (b) Normalized Gaussian fit (orange line) of the Lorentzian maxima representing the probe pulse is compared to the resonance (green dashed line) measured by ellipsometry on the nanocavity with Ga:ZnO and without a metasurface. For the sake of clarity only few spectra are shown. (c) Normalized resonance shift of about $\Delta\lambda =$ 15 nm of the nanocavity with 70 nm Ga:ZnO film and under pump excitation of intensity $I_p = 9$ mJ cm^{-2}.

which was found to be $\tau_{e-p} = 212$ fs. This relaxation rate is similar to what we have measured in Al:ZnO films, which a low photon lifetime or, alternatively, a small cavity Q-factor [102]. Excluding the slow thermal effects, which account for a limited fraction of the change in transmission, we find that our nanocavity has approximately an 80% amplitude modulation with a switching period of < 400 fs.

4.4.3 Numerical Model

The transient change in the optical properties of Ga:ZnO was estimated by fitting the shifted spectral response of the nanocavity with numerical simulation using a commercially available software based on the finite element method (COMSOL). Because the optical response of Ga:ZnO is dominated by the Drude response in the NIR range, we fit the Drude plasma frequency $\left(\omega_p = \sqrt{\frac{e^2 N_e}{\epsilon_o \epsilon_{\inf} m_e^* m_o}}\right)$ and damping coefficient $\left(\gamma_p = \frac{\hbar e}{m_e^* m_o \mu_e}\right)$ to match the resonance shift observed in pump-probe measurements, where N_e is the carrier concentration, m_o is the mass of electron, m_o^* is the effective mass of electron, and μ_e is the electron mobility. From the ω_p and γ_p extracted by numerical fits, we are able to calculate the temperature-dependent Drude parameters at the elevated electron temperature found using the TTM with experimental laser and material parameters (see Table 4.1). Here, we are describing the chemical potential as a function of temperature [137],

Table 4.1.
Summary of the Extracted Properties of Ga:ZnO Film

$T_e(K)$	$\omega_p(eV)$	$\gamma_p(eV)$	$\mu(eV)$	m_e^*	μ_e
300	1.850	0.0895	3.6803	0.1911	6.770
1891	1.700	0.0929	3.5056	0.2263	5.507

$$\mu(T_e) = \mu(0)\left[1 - \frac{\pi^2}{12}\left(\frac{T_e}{T_f}\right)^2\right]. \tag{4.10}$$

We plot the resulting change in optical constants for the two temperatures in Fig. 4.6b,c assuming a single Drude term. We observe that intraband excitation on Ga:ZnO film with 8% light absorption at pump level 9 mJ cm^{-2} induces a 130 nm shift of the ENZ wavelength with a small variation (6.5%) in the damping coefficient. At λ_o = 1200 nm, the absolute estimated change in refractive index ($\Delta n_{Ga:ZnO}$) is modest (0.24), while the relative variation ($\Delta n_{Ga:ZnO}/n_{Ga:ZnO}$) is 26%. As we have

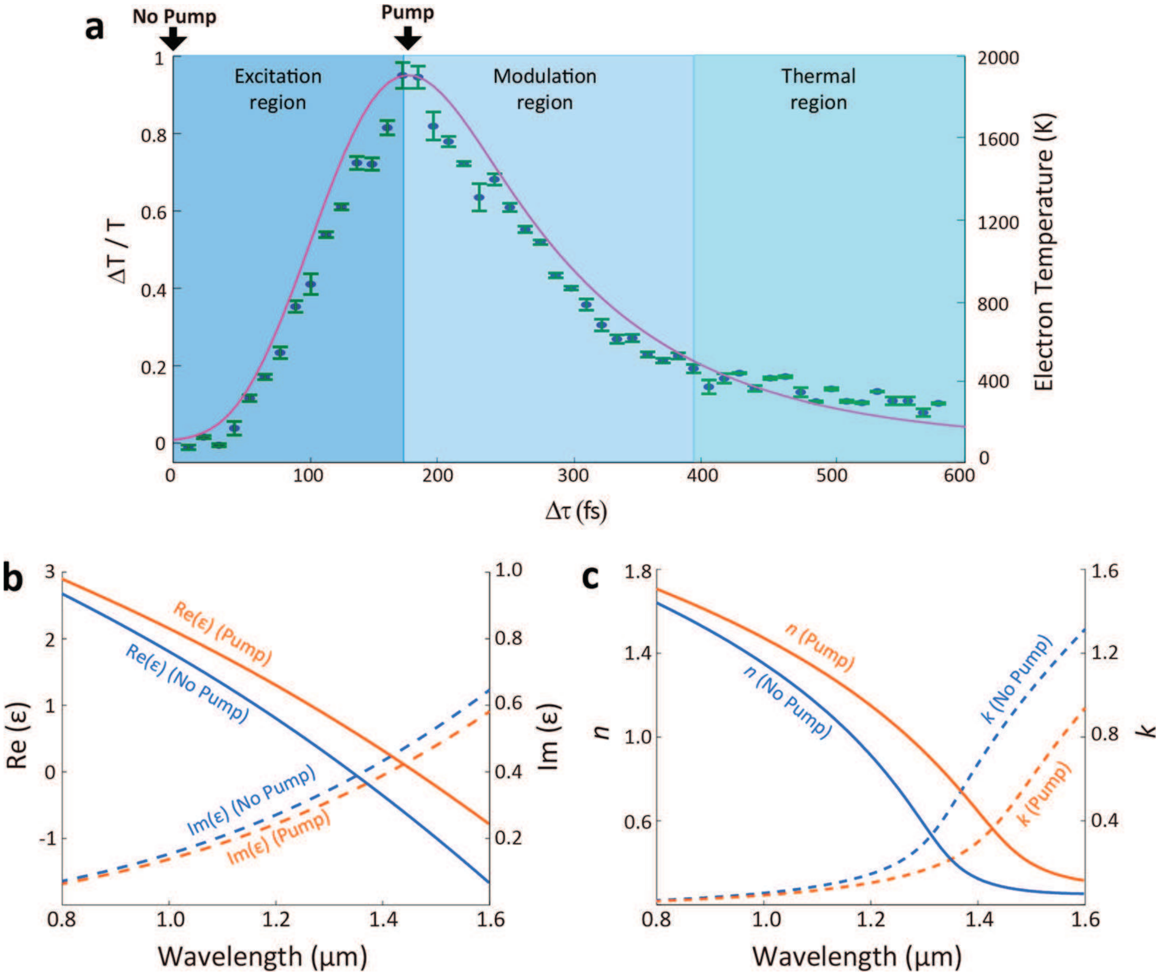

Figure 4.7. Transient Response of the Nanocavity. Percentage of the change in transmission as a function of the delay $\Delta\tau$ between the pump and probe pulses in Ga:ZnO embedded nanocavity. Transient dynamics is modeled with two temperature model (pink solid line). Three temporal phases have been identified: rise time, modulation region, and thermal tail. (b) Dielectric functions of Ga:ZnO thin film. Real (solid) and imaginary (dotted) part of permittivity of Ga:ZnO films are extracted by spectroscopic ellipsometry measurement without pump and fitted by numerical simulations with pump. (c) Refractive index of Ga:ZnO films calculated from the extracted dielectric function. Temporal positions for on/off pump states are indicated in panel a.

seen, operating within the ENZ spectral window gives rise to largely enhanced nonlinearities which are directly responsible for the optical modulation we recorded in our devices [81, 142].

4.5 Discussion and Conclusions

We have shown that TCOs near their ENZ wavlength exhibit two essential features of an ideal photonic switch: large and ultrafast modulation. This makes TCOs very promising materials for realizing high-performance dynamic devices with all-optical excitations. Although similar modulation performance has been achieved via electrical modulation [145, 150], the inherent RC delay limits the operating speed of these devices to sub-terahertz. Here, we have demonstrated not only large modulation in simple thin films of Al:ZnO ($\Delta R/R_0, \Delta T/T_0 \approx 100\%$), but also ultrafast ($< 1$ ps) responses. Furthremore, we have shown that this response occurs for a broad range of pump frequencies and, furthermore, that inter- and intraband nonlinearities are independent, allowing for simultaneous excitations. This feature has allowed us to realize optical modulation with > 2 THz frequencies, well above what is possible using electronic systems.

We have also demonstrated the exciting potential of TCOs for real-world nanophotonic devices. By incorporating a film of Ga:ZnO inside a metal-insulator-metal nanocavity, we observe improved modulation efficiencies while retaining the ultrafast properties of the TCO. We note that our strategy for improving efficiency relies on modulating a resonator, which could be generally applied to other systems including dielectric/metallic particles and waveguides. The optimal dynamic system will balance modulation amplitude and loss, since the inherent loss of a TCO near their ENZ wavelengths deteriorates the quality factor of the resonantor. Under these considerations, we expect the development of TCO materials will pave the road for improved and novel plasmonics and nanophotonics applications.

5. SINGLE AND DIMER NANOANTENNAS ON ENZ SUBSTRATES

Antennas operating at radiofrequency (RF) obey relatively simple design principles for finding their resonant wavelength. For example, the resonance of a monopole antenna occurs when the length of the antenna is integer multiples of one quarter the incident radiation's wavelength ($L_{ant} = \frac{n\lambda}{4}; \quad n = 1, 2, 3, ...$). Using this principle, it is straightforward to design a monopole antenna for any given wavelength by simply scaling the antenna's length proportionally. This property follows from the *scale-invariance* of Maxwell's equation in free-space [51]: given fields $\mathbf{E}(\mathbf{x}, t)$ and $\mathbf{B}(\mathbf{x}, t)$ satisfy Maxwell's equations, then fields $\mathbf{E}(\alpha\mathbf{x}, \alpha t)$ and $\mathbf{B}(\alpha\mathbf{x}, \alpha t)$ do as well. Remarkably, scale-invariance holds for Maxwell's equations in the presence of materials, *provided* the material parameters are not *dispersive.* For RF antennas, this caveat is fulfilled because the antenna is treated as a perfect conductor; the electrons are assumed to oscillate π-radians out-of-phase with respect to the driving field [151].

The scaling law is very useful for RF antenna design; however, when applied to metal nano antennas at optical frequencies, the scaling law fails. The reason is material dispersion. As discussed earlier, the electrons in metals are free to move throughout the material and are effectively treated as a non-interacting gas (i.e. a plasma). Owing to the finite electron density and effective mass, the response of the electron plasma is frequency dependent and exhibits a phase lag. The incident field can then significantly penetrate into the antenna and the scaling law is no longer valid.

Although optical antennas do not obey the RF scaling law, there is a modified linear scaling rule which was derived by considering the plasmon modes propagating down the length of the antenna [152]:

$$\lambda_{eff} = n_1 + n_2 \frac{\lambda}{\lambda_p}. \tag{5.1}$$

In equation (4.1), n_1 and n_2 are factors which depend on geometry and static dielectric properties and λ_p is the plasma wavelength. Accordingly, for a metal nanoantenna of length L, the half-wavelength resonance is not $\lambda/2$ but $\lambda_{eff}/2$. This effective wavelength scaling has been confirmed both numerically and experimentally [153] and allows for the design of antennas at optical frequencies.

Recently, a growing body of research is investigating the effects of ENZ TCO films on plasmonic systems. Prior plasmon-ENZ work include studies of single nanorods for resonance wavelength and radiation engineering [91, 93], metamaterial split-ring-resonators for polariton splitting [73, 154], and plasmon enhanced quantum wells for active terahertz control [155]. These studies demonstrate the great potential for plasmon-ENZ systems, but do not provide a thorough analysis or direct observation of the plasmon-ENZ coupling. Here, we investigate the plasmon-ENZ coupling in both single and dimer gold nanowire antennas with an aluminum-doped zinc oxide (Al:ZnO) TCO substrate exhibiting an epsilon-near-zero permittivity at telecommunication wavelengths. We characterize the plasmonic response of single nanorods with far-field spectroscopy and directly observe the electric field maps of single nanorods at the ENZ wavelength using scattering near-field optical microscopy (SNOM). Numerical calculations using finite element simulations of the correspondent nanorod waveguide coupled with an analytic 1D Fabry-Pérot model show excellent agreement with both far- and near-field measurements. We show that the plasmonic mode is highly dispersive and exhibits an effective mode index which is less than unity for wavelengths greather than the ENZ wavelength, resulting in the waveguide's wavelength being greater than the free-space excitation wavelength. Additionally, we demonstrate a strong suppression of near-field coupling between dimer nanorods on an ENZ substrate, which we attribute to the mode characteristics observed in single nanorod antennas.

5.1 Fabry-Pérot Model for Single Nanorod

To explain and analyze both the near- and far-field response of nanorod antennas on ENZ substrates, we develop a Fabry-Pérot (FP) model [153, 156] of the plasmon modes upon normal plane-wave illumination. In this model, the nanorod is treated as a truncated waveguide and incident light excites counter-propagating modes which reflect off either end of the nanorod's edges and form a standing-wave interference. The interference is either constructive or destructive depending on parameters such as free-space wavelength or nanorod length. Here, we consider gold nanorods with a thickness of 40 nm and a width of 70 nm, deposited onto a 315-nm-thick layer of either Al:ZnO or ZnO on top of a glass substrate. The length of the nanorods varies from 100 to 2000 nm. It is obvious that the normal plane-wave illumination with electric field along the nanorod length will excite modes only from the short faces of the nanorod, as illustrated in Fig. 1(a). A modal analysis of the nanorod cross-section using numerical simulations ensures only one supported quasi-bound mode. Simulations were done in COMSOL software using 2D [for mode analysis, Figs. 5.1(b-d)] and 3D finite element method (FEM) calculations. Permittivity values of gold were taken from Palik handbook [157], while values of Al:ZnO and ZnO were extracted from spectroscopic ellipsometry from 315-nm-thick Al:ZnO and ZnO films deposited via pulsed laser deposition (PLD) onto glass slides. The glass substrate was assumed to have a constant refractive index of 1.45. All edges of gold bricks were rounded with 10 nm radius of curvature. Simulation domains were squares (2D FEM) or cubes (3D FEM) with edge size of 4 m, surrounded with perfectly matching layers. We found the ENZ wavelength of the Al:ZnO film to be 1475 nm with a concomitant dielectric permittivity of $\varepsilon_{\text{ENZ}} = 0 + i0.35$. The spectroscopic data was fitted using a Drude+Lorentz oscillator model to obtain permittivity values across the 400-2500 nm spectral range. The electric-field mode profiles for the free-space wavelength of 1475 nm are shown in Figs. 5.1(b,c). As reported previously, the mode field is concentrated in air for the ENZ substrate compared with the ZnO dielectric substrate [156]. The mode propagation properties are demonstrated in Fig. 5.1(d) in terms of the effective mode index N and propagation length L_{prop} for both Al:ZnO and ZnO substrates. We find that the effective mode index for the nanorod waveguide on the Al:ZnO has a strong negative dispersion and, furthermore, that it is less than unity for wavelengths past the ENZ wavelength of 1475 nm. On the contrary, the effective mode index for the nanorod waveguide on the ZnO is weakly dispersive with a value of approximately 2. Another simulation of the mode propagation in a terminated nanorod provides the complex reflection coefficient $r = |r|\exp[i\phi]$, where $|r|$ and ϕ are the amplitude and phase, respectively, of the reflection coefficient [Fig. 5.1(e)]. We find that both reflection amplitude and phase are nearly constant, both for Al:ZnO and ZnO substrates.

We can now derive the complete near-field of a nanoantenna on an ENZ substrate and the equations which govern resonance by considering the modes of a nanorod subject to a plane wave excitation polarized along the length of the nanorod (along x-axis, see Fig. 5.1). The origin is set to the center of the nanorod. As mentioned, the incident field will predominantly scatter from each end of the nanorod and will generate counter propagating plasmonic modes $\mathbf{u}^+$ and $\mathbf{u}^-$. Because of the fixed cross-section of our nanorods, we can safely assume the propagation of plasmonic modes along x-axis as $\pm exp(\pm ik[x \pm L/2])$. Here, L is the length of the nanorod, $k = 2\pi N/\lambda_o + i/L_{prop}$ is the propagation constant of the plasmonic mode, L_{prop} is a propagation length, and the $\pm$ factor is associated with plasmonic modes propagation along $(+)$ or opposite $(-)$ to the x-axis. If the transverse field distribution of one plasmonic mode $\mathbf{u}^+$ is described as $[E_x(y,z), E_y(y,z), E_z(y,z)]^\dagger$, then the counter-propagating mode $\mathbf{u}^-$ should have electric field components $[-E_x(-y,z), -E_y(-y,z), E_z(-y,z)]^\dagger$ since the right-hand system $\{E_x, E_y, E_z\}$ rotates together with the propagation wave-vector. Due to the symmetry of the plasmonic mode $E_x(-y,z) = E_x(y,z)$, $E_y(-y,z) = -E_y(y,z)$, and $E_z(-y,z) = E_z(y,z)$, therefore the traverse distribution of the $\mathbf{u}^-$ mode is $[-E_x(y,z), E_y(y,z), E_z(y,z)]^\dagger$.

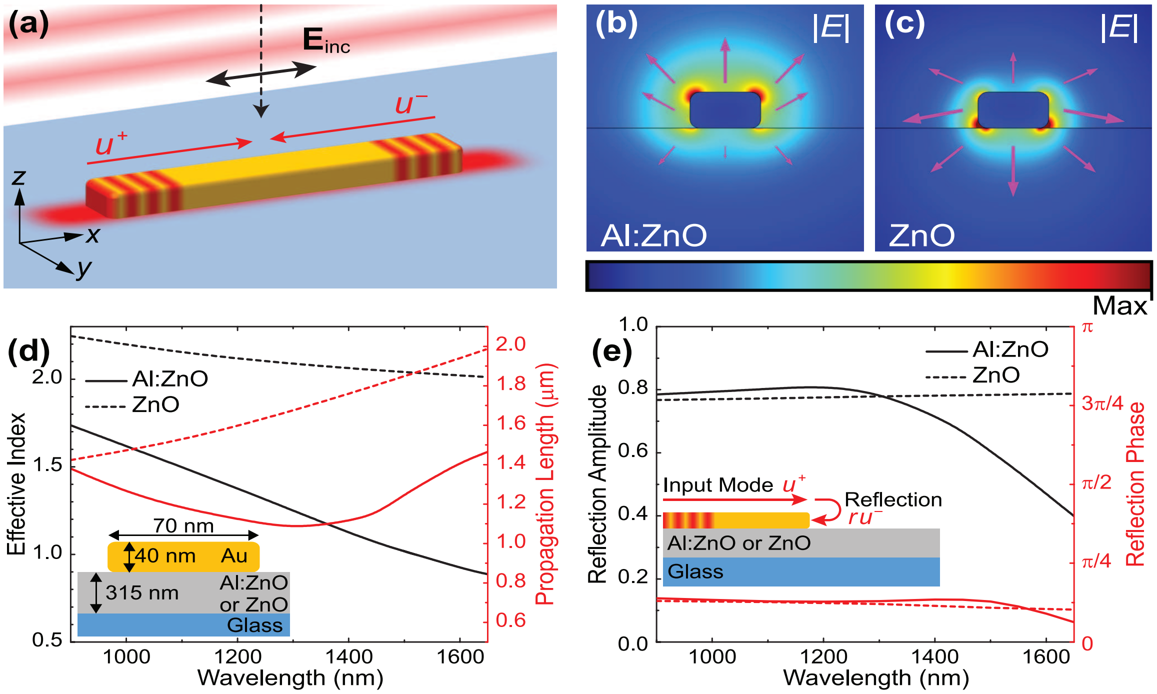

Figure 5.1. Semi-analytical Fabry-Pérot model for single nanorod. (a) Sketch of a nanorod upon normal illumination, exciting two counter-propagating nanorod modes. (b,c) Electric field distribution of nanorod waveguiding mode at the free-space wavelength of 1475 nm, deposited on (b) a Al:ZnO and (c) a ZnO substrate. Magenta arrows represent transverse electric field. (d,e) Numerically calculated effective mode index, propagation length, and reflection coefficient for a gold nanorod on the Al:ZnO (solid lines) and a ZnO substrate (dashed lines). Insets show the approximate configurations of the finite-element solver.

Each plasmonic mode will traverse the length of the nanorod, reflect from the opposite end, and begin to propagate in the opposite direction; this process then continues *ad infinitum*. If we let the $\beta = exp(ikL)$ denote the accumulated evolution after traversing a single length of the nanorod, and let r be the complex reflection coefficient from each end of the nanorod, then the mode u^+ excited at one end will evolve as:

$$A^+ \sum_{i=0}^{\infty} (r\beta)^{2i} \left[\mathbf{u}^+ + (r\beta)\mathbf{u}^-\right] \tag{5.2}$$

$$= A^+ \frac{\left[\mathbf{u}^+ + (r\beta)\mathbf{u}^-\right]}{1 + (r\beta)^2} \tag{5.3}$$

where A^+ is the excitation coefficient of mode $\mathbf{u}^+$ by the incident plane wave. Similarly, the mode $\mathbf{u}^-$ excited at the other end with a coefficient A^- will evolve as:

$$A^- \sum_{i=0}^{\infty} (r\beta)^{2i} \left[\mathbf{u}^- + (r\beta)\mathbf{u}^+\right] \tag{5.4}$$

$$= A^- \frac{\left[\mathbf{u}^- + (r\beta)\mathbf{u}^+\right]}{1 + (r\beta)^2} \tag{5.5}$$

The total field $\mathbf{E}(\mathbf{x})$ is then simply a sum of Eq. 5.3 and Eq. 5.5:

$$\mathbf{E}(\mathbf{x}) = \left[\frac{A^+ + (r\beta)A^-}{1 + (r\beta)^2}\right]\mathbf{u}^+ + \left[\frac{A^- + (r\beta)A^+}{1 + (r\beta)^2}\right]\mathbf{u}^- \tag{5.6}$$

Due to the symmetry of the incident fields polarization $A^- = -A^+ = -A$, meaning the excitation on one end is out-of-phase relatively to the excitation on the other end (however, it results in the same sign of the E_x component of each mode at both ends, since this is the polarization of the driving field). Thus, the total field electric field distribution for a nanorod upon normal illumination is

$$\mathbf{E}(\mathbf{x}) = A\frac{1 - (r\beta)}{1 + (r\beta)^2}\left[\mathbf{u}^+ - \mathbf{u}^-\right] = \frac{A}{1 + r\beta}\left[\mathbf{u}^+ - \mathbf{u}^-\right] \tag{5.7}$$

$$= \frac{A}{1 + r\beta}\left[\begin{pmatrix} E_x(y,z) \\ E_y(y,z) \\ E_z(y,z) \end{pmatrix} e^{ik(x+L/2)} - \begin{pmatrix} -E_x(y,z) \\ E_y(y,z) \\ E_z(y,z) \end{pmatrix} e^{-ik(x-L/2)}\right] \tag{5.8}$$

$$= \frac{2A\sqrt{\beta}}{1 + r\beta}\begin{pmatrix} E_x(y,z)\cos(kx) \\ iE_y(y,z)\sin(kx) \\ iE_z(y,z)\sin(kx) \end{pmatrix} \tag{5.9}$$

The beauty of the above semi-analytical Fabry-Prot model is that it allows finding full three-dimensional (3D) near-field distribution without doing complicated 3D simulations, but instead it uses simple 2D simulations (modal analysis) and relatively simple 3D simulation of mode reflection (the last takes much less computational time compared to the full 3D simulation of nanorod excitation, since the simulation domain is smaller, and the effect is non-resonant, as can be seen in Fig. 5.1). Using a single value A for normalization, we managed to accurately predict with our FP model distributions $E_y(x,y)$ and $E_z(x,y)$ at any alititude z and for any antenna length. Fig. 5.2 shows a side-by-side comparison of near-field maps obtained using full 3D FEM simulations (left column) and our semi-analytical FP model (right column) for a 600 nm antenna. The top and bottom rows show the maps obtained at different heights above the nanoantenna. As can be seen, there is a strong agreement between FP model and FEM simulations for E_y and E_z. A disagreement in E_x is caused by the presence of relatively strong exciting plane-wave and far-field antenna radiation in full 3D FEM simulations, while FP model predicts only evanescent field distribution. This model also predicts the position of resonances, since there the near-field will be at maximum. It is obvious that only the denominator in Eq. 5.6 is responsible for the resonance behavior. Neglecting weak amplitude variation of r and β, we find the resonance condition as $arg\left\{r\beta\right\} = \pi(1+m); m = 0, 2, 4, ...$ This simplifies to

$$\frac{2\pi N}{\lambda_o} L + \phi = \pi(1+m); m = 0, 2, 4, ... \tag{5.10}$$

where L is the nanorod length, and λ_0 is the free-space wavelength. Physically, this implies that, at resonance condition, excitations from one end of the nanorod should constructively interfere with the out-of-phase excitation from the opposite end after accumulating a single propagation and reflection phase. We note that Eq. (5.10) describes bright-modes only. Generalized FP model do not incorporate the excitation source and implies that, at resonance condition, the round-trip should be in-phase with initial excitation. Therefore, generalized FP models predict both bright- (even m) and dark-modes (odd m), the latter being inaccessible using normally incident plane wave source.

Equation 5.10 specifies the relation between nanorod length and resonance wavelength; consequentially, the rate of change in resonance wavelength as a function

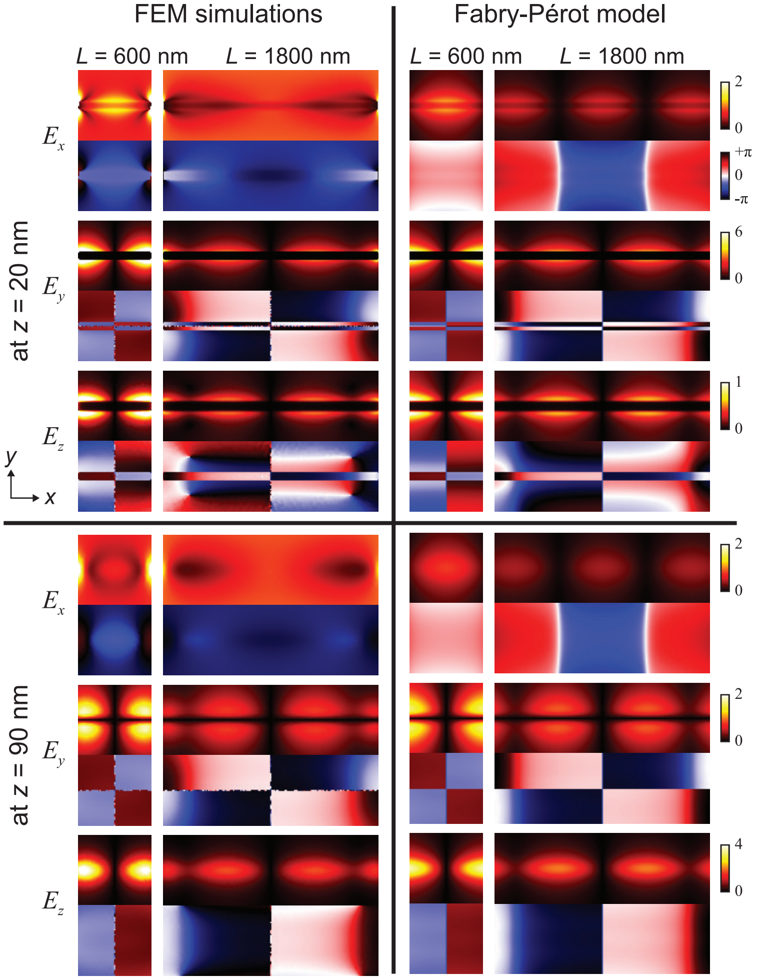

Figure 5.2. Comparison of the field produced by full 3D FEM simulations and semi-analytical Fabry-Pérot model. Simulations are done for gold antennas on Al:ZnO substrate at 1500 nm excitation from the bottom, polarized along the antenna length. The field was calculated at $z = 20$ nm (i.e., through the middle of the antenna, top) and $z = 90$ nm (i.e., 50 nm above the antenna, bottom) for two antenna lengths: 600 (left) and 1800 nm (right). The fields were normalized to the amplitude of the transmitted plane wave (note different colormap scales).

of antenna length can be calculated by differentiating Eq. 5.10 with respect to the free-space wavelength, λ_o. First, we re-write Eq. 5.10 as

$$2\pi L(\lambda_o) = \frac{\lambda_o}{N(\lambda_o)}[\pi + \pi m - \phi] \tag{5.11}$$

and then differentiate to find

$$2\pi \frac{dL}{d\lambda_o} = \left(\frac{1}{N} - \frac{\lambda_o}{N^2} \frac{dN}{d\lambda_o} \right) [\pi + \pi m - \phi] \tag{5.12}$$

This expression can then be inverted to find the change in resonance wavelength as a function of antenna length.

$$\frac{d\lambda_o}{dL} = \frac{2\pi}{\pi + \pi m - \phi} \left(\frac{1}{N} - \frac{\lambda_o}{N^2} \frac{dN}{d\lambda_o} \right)^{-1} \tag{5.13}$$

$$= \frac{2\pi}{\pi + \pi m - \phi} \left(\frac{N^2}{N - \lambda_o \frac{\partial N}{\partial \lambda}} \right) \tag{5.14}$$

This result follows from our assumption that the reflection phase ϕ is wavelength independent, which is justified from our FEM analysis [Fig. 5.1(e)]. Equation (5.14) shows that for modes with largely dispersive effective index, the scaling law between resonant wavelength and antenna length is non-linear. Furthermore, in the ideal limit $N \rightarrow 0$ the resonant wavelength becomes independent of antenna length, an effect referred to as a resonance pinning [91]. On the contrary, for non-dispersive and non-zero effective mode index the resonant wavelength should be simply proportional to the antenna length: $\lambda_0 = 2\pi NL/(\pi + \pi m - \phi)$.

In addition to the dispersive behavior of the resonance, we also use our model to accurately predict the near-field phase and magnitude of the single antennas. Fig. 5.2 shows a side-by-side comparison of near-field maps obtained using full 3D FEM simulations (left column) and our semi-analytical FP model (right column) for a 600 nm antenna. The top and bottom rows show the maps obtained at different heights above the nanoantenna. As can be seen, there is a strong agreement between FP model and FEM simulations for E_y and E_z.

5.2 Single Nanorod Far-Field Characterization

In order to verify the non-linear scaling law and resonance pinning for antennas on an ENZ substrate, as followed from the above semi-analytic FP model, we fabricated and characterized nanorod antenna arrays on Al:ZnO substrate. We deposited

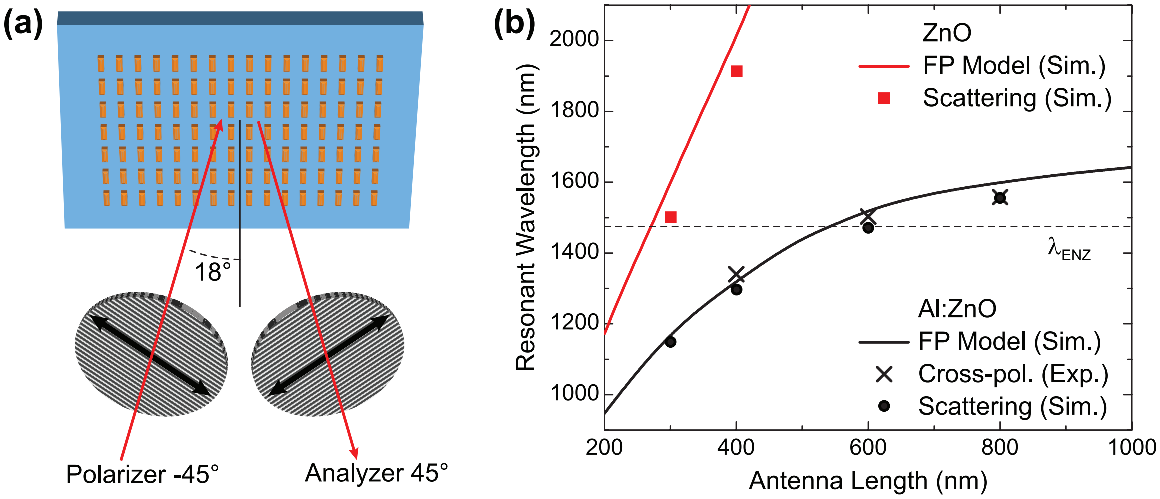

Figure 5.3. Far-field characterization of nanorod arrays. (a) Cross-polarized configuration of our ellipsometer used for measuring the far-field scattering of the single antenna arrays. The input polarization is rotated −45° with respect to the nanorod's long axis and incident at 18°. The reflected light is passed through an analyzer set at the 45°. (b) Resonant wavelength as a function of antenna length for the Al:ZnO (black) and ZnO (red) substrates. The solid lines are calculated using the Fabry-Pérot model; square and circular markers are results of scattering cross-section numerical calculations; and cross markers indicate experimental values obtained from cross-polarization spectroscopy. The dashed line indicates the ENZ wavelength of 1475 nm.

Al:ZnO films via pulsed laser deposition (PVD Products, Inc.) onto glass substrates using a KrF excimer laser (Lambda Physik GmbH) operating at 248 nm. A 2wt% doped Al:ZnO target (>99.99% purity) from Kurt J. Lesker Corp. was used as the ablation source. The energy density of the laser at the target surface was maintained at 1.5 J/cm^2 and the deposition temperature was fixed at 95°C. The optical properties of Al:ZnO films were characterized by spectroscopic ellipsometry (V-VASE, J.A. Woollam) over the spectral region from 400 to 2500 nm (see Fig. 5.4). The dielectric function of the film was retrieved by fitting a Drude + Lorentz oscillator model to the data. The model and the fitted parameters are shown in Eq. 5.1 and Table 5.1, respectively. To fabricate gold nanorods, positive electron beam resist (ZEP 520 A) was spin coated at 4000 rpm and then exposed by electron lithography (Vistec VB6). The beam energy was 100 kV and the beam current was 1.012 nA. We deposited a 40-nm-thick gold film on the resist using an electron beam evaporator. The sample was developed in ZED-N50 (n-amyl acetate) for 1 min, and then dipped in isopropyl alcohol for 30s to remove the ZED-N50. By setting the period along and perpendicular to the length of the antennas to $P_{\|} = 1200$ nm and $P_{\perp} = 600$ nm, respectively, we minimized antenna interaction while maintaining a significant antenna density. Each array consisted of antennas of lengths $L = 400$, 600, and 800 nm. Representative scanning electron microscope images are shown in Fig. 5.5. We measured the far-field response of the single nanorod arrays using the cross-polarized reflection configuration of our spectroscopic ellipsometer shown in Fig. 5.3(a). The sample was mounted such that the long axis of the nanorods was oriented vertically. We set the input polarizer at 45° and the output analyzer at −45° and collected the reflected light over a 900–2500 nm spectrum. The angle of incidence was set at 18° — the minimum physical angle of the ellipsometer. Using this setup, we were able to collect the field radiated by the nanorod array while suppressing the strong reflected signal of the substrate. We fitted the reflection spectra with Lorentzian curves to extract the resonant wavelength. In Fig. 5.3(b) we plot the experimentally observed resonance wavelengths for antennas of lengths $L = 400$, 600, and 800 nm (crosses). In addition, we plot the resonant wavelengths predicted using our Fabry-Pérot model,

Table 5.1.
Ellipsometry Model and Fits

ϵ_∞	$\omega_p(eV)$	$\Gamma_p(eV)$	f_l	$\omega_l(eV)$	Γ_l
2.5	2.32	0.089	15.02	4.53	0.001

$$\epsilon(\omega) = \epsilon_\infty - \frac{\omega_p^2}{\omega(\omega + i\Gamma_p)} + \frac{f_l\omega_l^2}{\omega_l^2 - \omega^2 + i\omega\Gamma_l} \tag{5.15}$$

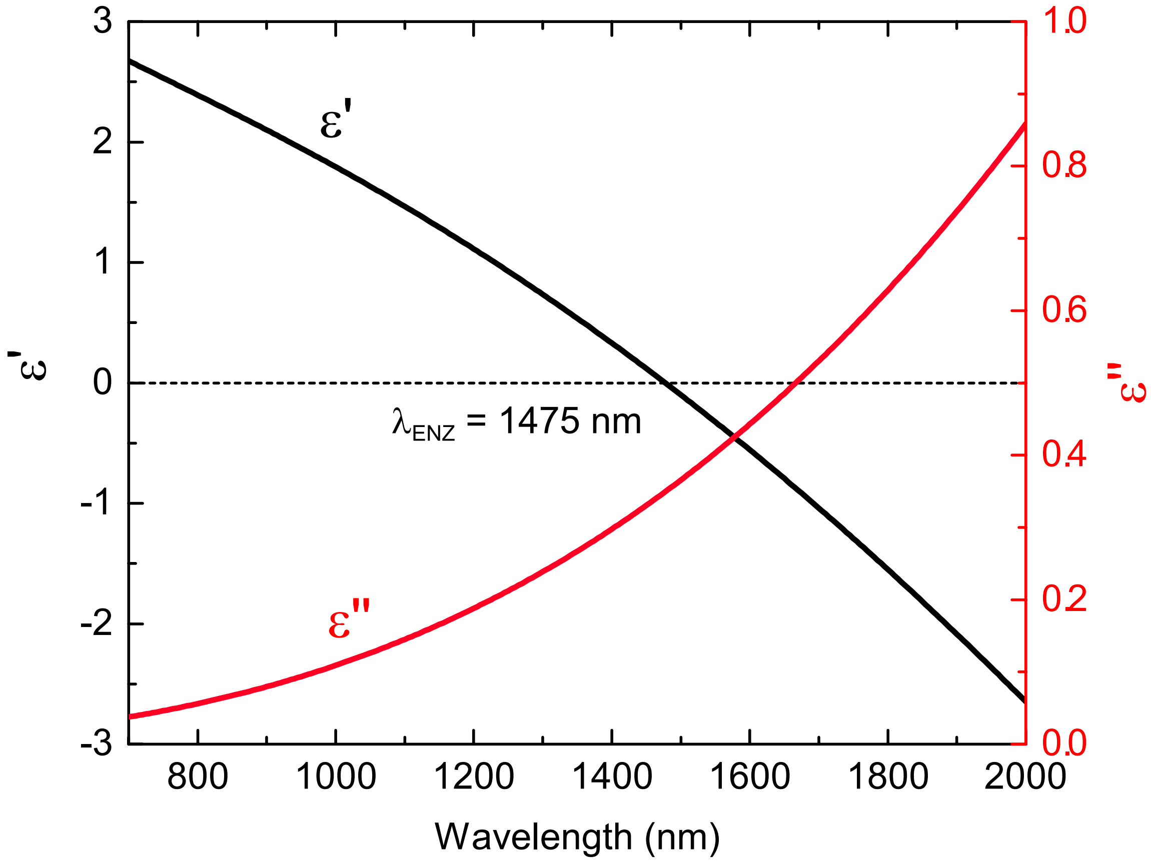

Figure 5.4. Permittivity values of the Al:ZnO film extracted using spectroscopic ellipsometry. The ENZ wavelength,λ_{ENZ}, is defined when real part $\epsilon' = 0$.

Eq. (5.1) (solid line), along with resonances for the scattering cross-sections obtained using full-wave FEM simulations of isolated antennas (circles). For comparison, we included corresponding values for a ZnO substrate of similar thickness (red lines and dots). As can be seen, there is a good agreement between measurements and simulations, supporting the assumption of the negligible antenna interaction. Additionally, the resonance position predicted by our semi-analytical FP model is in good correspondence with results of full 3D simulations and measurements, even though the ellipsometer excitation angle in the experiment was slightly different than normal

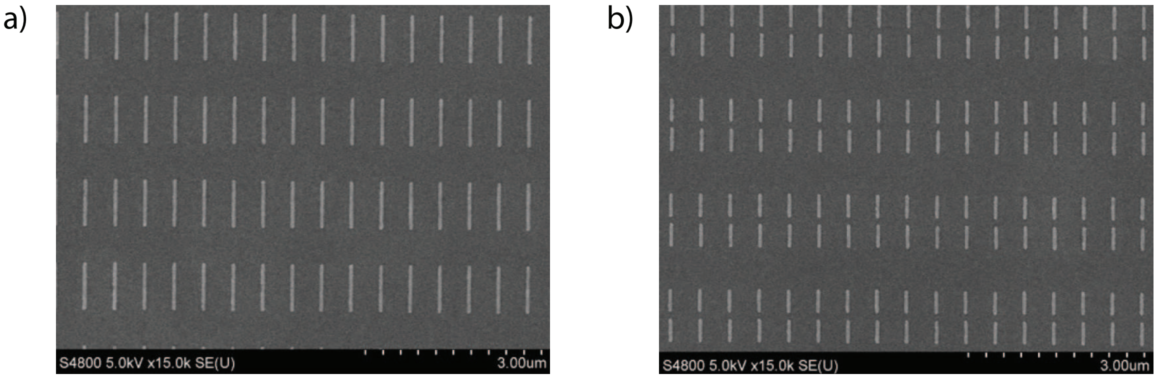

Figure 5.5. Representative SEM image of (a) single and (b) dimer nanoantenna arrays deposited on Al:ZnO substrates.

incidence. Finally, we verify that the resonance wavelength is largely non-linear and becomes nearly independent of antenna length beyond the ENZ wavelength, an effect referred to as resonance pinning [91].

5.3 Single Nanorod Near-Field Characterization

To directly image the modes of the nanorods, we perform near-field characterization using Scanning Near-field Optical Microscopy (SNOM). This was done using a commercial scattering-type SNOM (Neaspec GmbH). For the experiments, we used Platinum-coated standard Si atomic force microscope tips (Arrow$^{\text{TM}}$ NCPt from NanoWorld) operated in a tapping-mode. The tip radius of curvature of less than 25 nm is specified by the manufacturer. The tapping frequency and amplitude were $\sim$280 kHz and $\sim$50 nm, correspondingly. We illuminated all samples normally from beneath using a tunable telecom diode laser (TLB-6500-H-ES from New Focus) and a parabolic mirror. The spot size on the sample was approximately $\sim$50 μm and the incident total power was maintained at $\sim$1 mW. Scattered light was collected using a second parabolic mirror. A Mach-Zehnder interferometer with an oscillating mirror ($f \sim 300$ Hz) in the reference arm is incorporated in our SNOM in order to

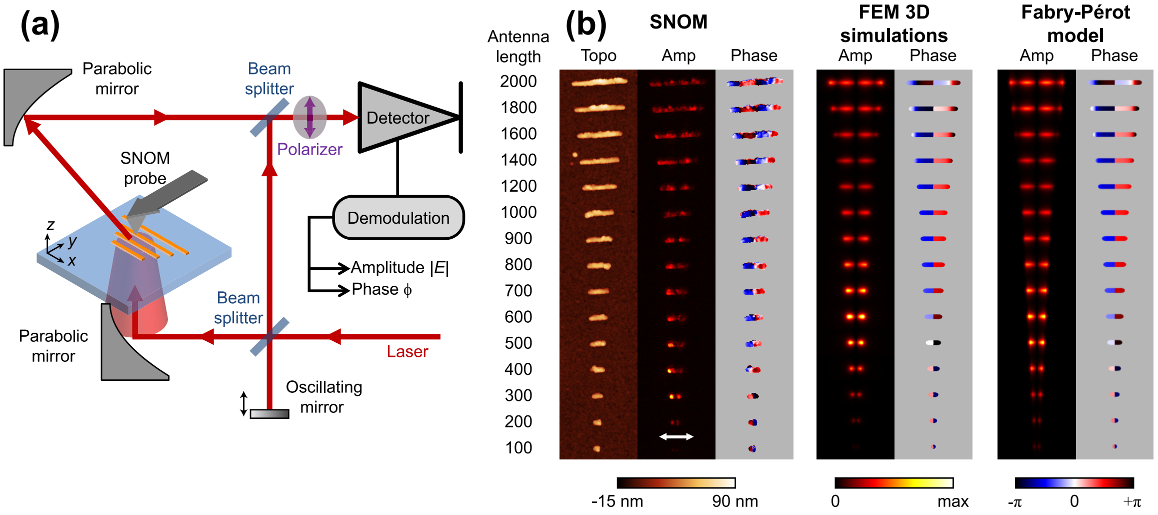
(a)
Parabolic mirror
Beam splitter
Detector
Polarizer
SNOM probe
z
y
x
Demodulation
Amplitude |E|
Phase ϕ
Beam splitter
Parabolic mirror
Laser
Oscillating mirror
(b)
Antenna length
SNOM
Topo
Amp
Phase
FEM 3D simulations
Amp
Phase
Fabry-Pérot model
Amp
Phase
2000
1800
1600
1400
1200
1000
900
800
700
600
500
400
300
200
100
-15 nm
90 nm
0
max
-π
0
+π

Figure 5.6. Near-field optical microscopy of individual nanorods. (a) Schematic of the SNOM setup. (b) First column contains the measured topography, the magnitude, and the phase of the near-field for gold antennas on Al:ZnO substrate at 1475 nm excitation, polarized along the antenna length (the polarization is shown with a white arrow). Second and third column are the corresponding z-component of the electric field (E_z) calculated at 50 nm above nanorods with full 3D finite-element simulations and semi-analytical Fabry-Pérot model, respectively. Recorded topography and designed antenna parameters were used for masks in phase maps.

resolve both amplitude and phase using a pseudo-heterodyne detection scheme [158]. To remove background signals, the collected output was demodulated at the third harmonic of the tip's tapping frequency. This technique allows us to simultaneously map both magnitude and phase of the near-field, in addition to the sample topography. Due to the tip elongation along z-axis, the recorded near-field signal corresponds well to the normal z-component of the electric field approximately 50 nm above the structure [159–161]. A schematic of our setup is shown in Fig. 5.6(a). The sample contains a column of individual nanorods of lengths varied in 100 nm steps from 100 nm to 2000 nm; the spacing between antennas was 1000 nm. Fig. 5.6(b) shows the topography and near-field maps of the gold antennas on the underlying Al:ZnO substrate, along with the near-field magnitude and phase, calculated with full FEM simulations and predicted from our semi-analytic Fabry-Pérot model as:

$$E_z(x) \propto \sin\left(\frac{2\pi N}{\lambda_0}x + \frac{i}{L_{\text{prop}}}x\right) \tag{5.16}$$

We find the antennas of length less than 1000 nm support dipolar near-field distribution, as clearly seen by the phase profile; furthermore, we confirm the 600 nm antenna is at resonance with the 1475 nm excitation. The strong agreement between all near-field maps confirms the low effective mode index of the nanorod plasmonic mode for ENZ substrate. Additionally, the correspondence between near-field measurements and simulations verifies the optical properties of fabricated Al:ZnO substrate on the subwavelength scale, which makes it unique compared to the engineered ENZ metamaterials composed of stacked finite-size structures [25, 27, 105].

5.4 Suppression of Near-Field Coupling in Plasmonic Dimer Antennas

Having shown the ability for ENZ materials to significantly alter plasmonic resonances in single nanorods, we now turn our focus to dimer nanorods deposited on an ENZ substrate. In general, the resonance of a dimer pair will depend on the separation between rods due to the interparticle coupling [162, 163]. For nanorod pairs oriented along their longitudinal axis, the resonant wavelength red-shifts away from the isolated resonant wavelength as the separation decreases. To characterize the shift in resonance for dimer antennas on an ENZ substrate, we fabricated arrays of dimer nanorods, consisted of two $L = 400$ nm nanorods and separated by a gap of 30, 50, 100, and 200 nm. We chose the period of all arrays to be $P_{\parallel} = 1300$ nm and $P_{\perp} = 500$ nm to maintain a constant and significant dimer density. We employed FEM simulations to calculate the scattering, absorption, and extinction cross sections of gold dimer antennas on an Al:ZnO substrate; for comparison, we performed similar simulations for dimer nanorods on a glass substrate [Fig. 5.7(a)]. We chose the antenna length for dimers on glass to be 320 nm so that the resonance positions coincide for gap distances of 200 nm. For dimers on ENZ, we find the spectral red-shift is reduced in comparison to antennas on glass and, furthermore, that the red-shift decreases monotonically for increasing individual antenna length. Additionally, we find that the extinction cross section's spectral width is narrow as a result of the asymmetric scattering and absorption cross-sections. In contrast, the red-shift for dimer antennas on glass substrate is independent of antenna length, which agrees well with previous observations and analysis [162–164]. We measured the far-field scattering from our arrays of gold dimers using the same ellipsometry setup used to characterize arrays of single antennas. Fig. 5.7(b) shows the experimentally obtained shift in resonance of $L = 400$ nm nanorod dimers (black squares), normalized to the resonant wavelength of dimers with $G = 200$ nm, as a function of gap size. Gap sizes were verified using scanning electron microscopy and all resonant wavelengths were found by fitting the scattering spectrum with Lorentzian peaks [see inset of Fig. 5.7(b)]. Included in this figure are the shift in the resonance wavelength for $L = 400$ nm dimers on Al:ZnO (black line) and for $L = 320$ nm dimers on a glass substrate (red line). The antenna length of 320 nm for dimers on glass substrates was chosen such that the resonance shift occurred at the same spectral range as our ENZ wavelength. Our experimental results show a reduced red-shift for antennas on the Al:ZnO substrate and corroborate our numerical simulations. The reduced shift in resonance corresponds to a suppression of near-field coupling between the two nanoantennas of the dimer. In general, the normalized red-shift of two plasmonic antennas as a function of gap size is proportional to the ratio of the interparticle near-field interaction to the single intraparticle Coulombic restoring force [163]. As we have shown from our single particle analysis and previous work [91], the near-field distribution of a single particle antenna is significantly altered at the ENZ regime of the substrate. In particular, we find that the field is primarily concentrated outside of the substrate past the ENZ wavelength since the air becomes the more optically dense media. The experimentally observed and numerically calculated strong reduction in the red-shift, as compared to dimers on glass substrates, implies that the near-field interaction is thus suppressed. We do note that a reduction in the red-shift will also follow from an

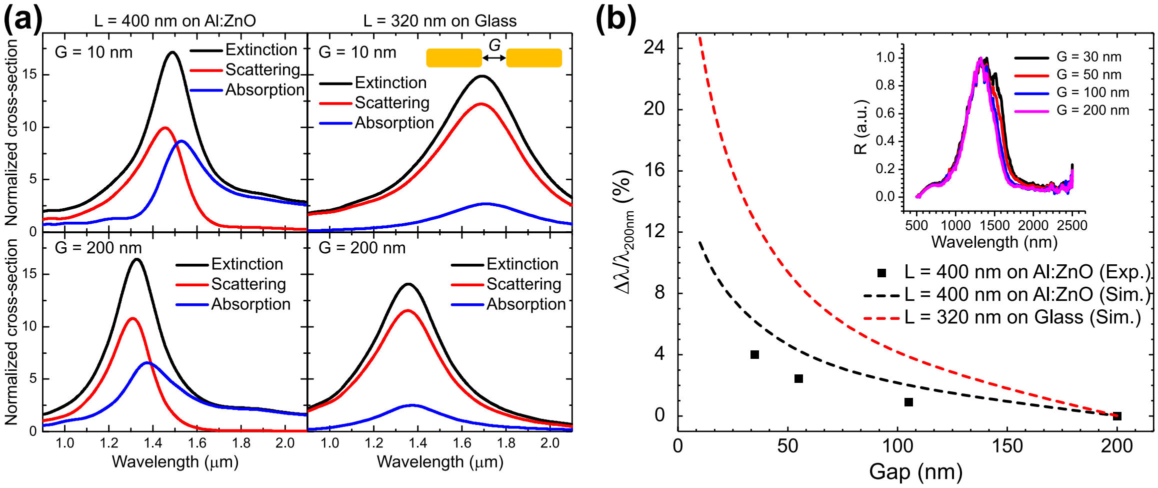

Figure 5.7. Suppression of near-field coupling in dimer antennas. (a) Scattering, extinction, and absorption cross-sections of dimer antennas on both Al:ZnO (left column) and glass (right column) substrates calculated with FEM. Gap distances of 10 and 200 nm are shown in the top and bottom rows, respectively. The antenna lengths are chosen such that the maximum cross-sections coincide at a gap distance of 200 nm to clearly illustrate the distinction in total red-shift. (b) Resonance wavelength red-shift of dimer nanoantennas as a function of gap size, normalized to a gap of 200 nm. Black squares and line mark the experimentally measured and simulated, respectively, red-shift of dimers on Al:ZnO as a function of gap size. Red line marks simulated red-shift for dimers on glass. Inset shows the collected cross-polarized reflection spectra.

increase in the individual antenna length of the dimer pair because the intraparticle Coulombic restoring force goes as a $1/(\text{particle size})^3$ dependence and the normalized red-shift, in the quasi-static dipole approximation, is given by $\Delta\lambda/\lambda_0 = (G/L+1)^{-3}$ where G is the gap size and L is the antenna length [163]. Indeed, we do observe a slight decrease in red-shift for antennas on a glass substrate for increasing antenna lengths (See Fig. 5.8). However, this contribution to the red-shift reduction is small, even for large changes in antenna lengths, and cannot account fully for our observations. We thus conclude that the predominant mechanism is the suppression of near-field interactions due to the ENZ substrate. We note that the suppression of the near-field coupling is directly related to the ENZ nature of the substrate and is independent of the physical origin of the ENZ response; therefore, near-field suppression is a general feature of an ENZ substrate. Furthermore, we anticipate that an ENZ substrate will also result in similar suppression of near-field coupling between dimer antennas aligned along their transverse axis.

5.5 Discussion and Conclusions

Maxwell's equations dictate that the fields in an ENZ material exhibit anomalous phase variation and the wavelength approaches infinity, i.e., $\lambda \to \infty$ as $\varepsilon \to 0$. This reasoning provides an intuitive picture for understanding and interpreting our results. As mentioned earlier, usually the scaling between the resonance wavelength and the physical length of the nanorod is approximately linear; however, as we have shown using Eq. (5.14), a non-linear scaling occurs when the effective mode index is largely dispersive. Although the refractive index of the metal nanorod is itself dispersive, the electric fields of the plasmon mode are primarily located outside of the nanorod, and, accordingly, the mode's effective index is predominately determined by the surrounding material's index. This implies that the incident radiation's wavelength λ_0 and the nanorod's plasmon wavelength λ_{SPP} are proportional via $\lambda_{\mathrm{SPP}} = \lambda_0/n_{\mathrm{eff}}$ and that the nanorod's resonance wavelength changes linearly to an increase in antenna length for a non-dispersive dielectric environment. However, for an antenna located near an ENZ material, the plasmon modes of the nanorod will have a strong negative dispersion and exhibit a near-zero effective index, as we have observed [see Fig. 5.1(d)]. Consequentially, when the free-space wavelength of incident light is increased near the ENZ point, the effective mode index *decreases* and the plasmon wavelength will *increase* dependent on the magnitude of the dispersion; as such, the nanorod will only resonate at a longer length.

In summary, we have demonstrated dispersive, less than unity index plasmon modes with gold antennas on an Al:ZnO substrate with a near-infrared ENZ point.

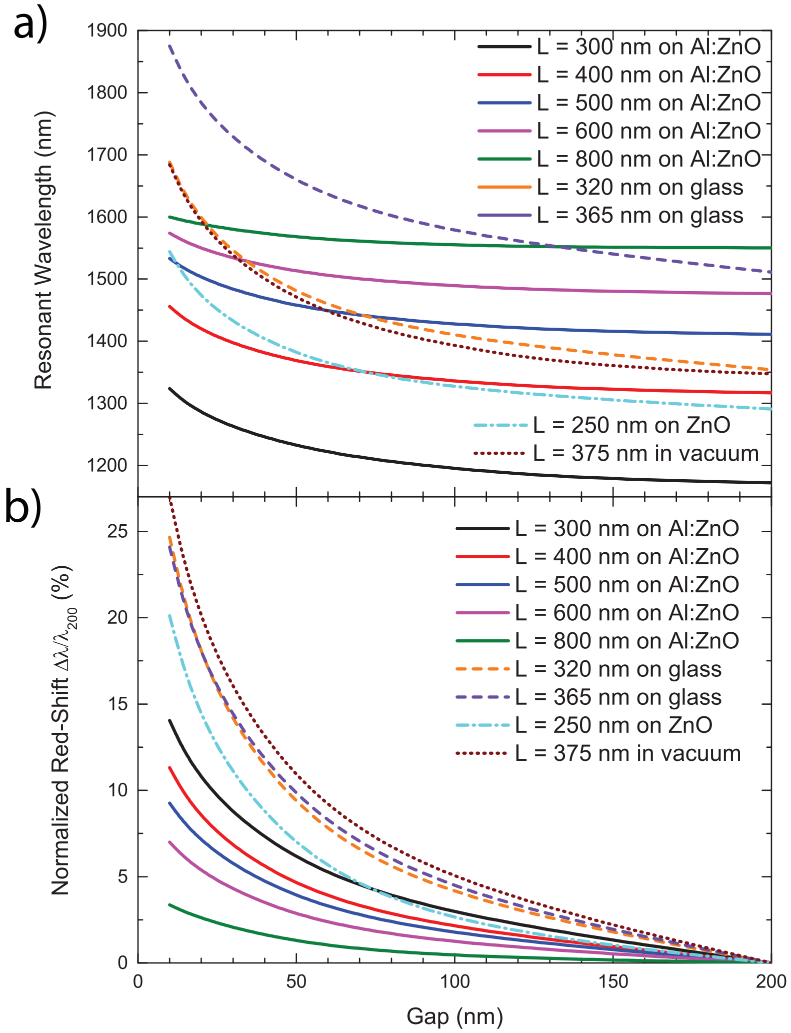

Figure 5.8. Resonance wavelength of dimer antennas as a function of gap size and antenna length. The resonance wavelength was calculated as a position of the peak in the simulated extinction spectra. Bottom image shows a shift of the resonance wavelength for dimer antennas, normalized to the resonance wavelength of dimer antennas with a 200-nm gap. The shift is reduced with a decrease of antenna length for ENZ substrate, while it is nearly the same for antennas on a glass and ZnO substrate or in vacuum.

Furthermore, we demonstrated a reduced red-shift in the resonance of dimer antennas on a ENZ substrate as a function of diminishing gap sizes because of suppressed near-field interactions. We have also developed a robust and accurate semi-analytic

Fabry-Pérot model for calculating electromagnetic near-fields, dispersion, and resonances of single nanorod antennas on arbitrary substrates. Our observations and analysis open new directions for engineering the resonance of both single and coupled plasmonic antennas. For instance, the established reduction in near-field coupling allows one to design arrays of independently operating antennas with higher densities and thereby significantly improve the array characteristics, especially when targeting gradient metasurface implementations. Moreover, by utilizing the suppressed near-field coupling, it may be possible to induce large modulation amplitudes by tuning the permittivity of the substrate around the ENZ point through either electrical or optical control. Additionally, it may be possible to utilize the near-zero index plasmon mode for increasing coherence between quantum emitters coupled to a plasmon system.

6. STRONG COUPLING BETWEEN ENZ FILMS AND PLASMONIC ANTENNAS

Coupled systems are prevalent and quintessential physical phenomena. The electromagnetic transitions of atoms and molecules are modified by coupling with the local environment or other emitters. Typically, these interactions are weak and treated with perturbation theory, such as the alteration of spontaneous decay rate (Purcell Effect) [165] or Forster energy transfer between donor and acceptor atoms and molecules [166]. Within this *weak* coupling regime, the emitter's energy levels remain unperturbed by the coupling; however, if the coupling is sufficiently strong enough such that energy exchange between the two systems exceeds the individual dissipation rates and decoherence, then the system enters the *strong* coupling regime [79, 136, 167, 168]. Here, it is no longer possible to describe the emitter as separate from the environment since the excitation becomes delocalized, and the coupled system must be treated as a new, hybrid system. The hybrid nature of strongly coupled systems introduces a breadth of new physical phenomena, including effects in quantum information processing, quantum-cavity electromagnetics, and ultrafast single-photon switches.

Photonic strong coupling is typically discussed in the context of an optical microcavities and a collection of molecules, such as in exciton polaritons [169–171], Van der Waal structures [172], and quantum dots [173,174]. These systems exhibit both interesting and potentially applicable features such as low-threshold switching [175, 176] and semiconductor lasing [177]. Typically, the coupling strength, g, between an optical cavity and a polariton is well below the thermal energy at room-temperatures ($k_B T \approx 1/40$ eV), so experiments are done at cryogenic temperatures to resolve the polariton energy from thermal decoherence. This limits the range of applications to nitrogen-cooled systems. The ideal strong coupling device or application would operate at room-temperature, which has led researchers to devote a large research front on finding novel systems which exhibit large coupling strengths.

One stategy for increasing the coupling strength, g, beyond room-temperature energies is by decreasing the optical cavity mode. The coupling strength in a system is inversely proportional to the square of the optical mode volume, V ($g \propto 1/\sqrt{V}$). Plasmonic offers extremely compact modes on the order of ten's of nanometers [39, 178] and even sub-nanometer [179]. Recent demonstrations of room-temperature strong coupling in plasmonic systems include plasmonic antennas and J-aggregates [180,181], 2-D materials [182], and single molecules [183]. This does not preclude the possibility of plasmonic strong coupling in systems which are not molecular. Strong coupling is a general feature of any coupled systems where energy is exchanged faster than the dissipation.

Here, we present a novel strongly coupled plasmonic systems by coupling the plasmon resonances of gold nanoantennas with the ENZ mode of an ultrathin film of Al:ZnO. At room-temperatures, we demonstrate a Rabi splitting $\hbar\Omega_R \approx 300$ meV. We show that for increasing antenna lengths, the antenna resonance exhibits a clear anti crossing behavior at the ENZ wavelength, which we numerically validate and match with a coupled harmonic oscillator model. Furthermore, we verify that strong coupling is sensitive to both the Al:ZnO film thickness and the Fourier components of the antenna's scattered field. Our results validate the existence of coupling between the non-radiative ENZ mode and provide a route to couple large fields into the TCO film, which could help to greatly enhance nonlinear interactions.

6.1 Coupled Harmonic Oscillators

Although many strongly coupled systems are inherently quantum, the underlying physics is accurately captured using the paradigm model of two coupled harmonic oscillators [184]. Remarkably, this system not only captures strong coupling effects such as energy splitting and level crossing, but can be applied to a large class of coupled systems. Examples include electromagnetic induced transparencies, Fano resonances, Borrman effects, and Kerker effects [185]. Let us consider two coupled harmonic oscillators and write the system of equation for the harmonic mode amplitude of oscillator one $x_1(\omega)$ and two $x_2(\omega)$ as [186],

$$\begin{pmatrix} \omega_1 - \omega - i\gamma_1 & g \\ g & \omega_2 - \omega - i\gamma_2 \end{pmatrix} \begin{pmatrix} x_1(\omega) \\ x_2(\omega) \end{pmatrix} = i \begin{pmatrix} f_1(\omega) \\ f_2(\omega) \end{pmatrix} \tag{6.1}$$

where ω is the frequency, $\omega_{1,2}$ and $\gamma_{1,2}$ are the resonance frequency and damping rates of oscillator one and two, respectively, $f_{1,2}(\omega)$ are the harmonic driving forces on oscillator one and two, respectively, and g is the coupling constant between the two oscillators. The eigenvalues of the system are solved by setting the determinant of the 2x2 matrix to zero and solving the resulting quadratic equation. The two complex eigenvalues are then given by,

$$\omega_{\pm} = \frac{1}{2}\left[\omega_1 + \omega_2 - i(\gamma_1 + \gamma_2)\right] \pm \frac{1}{2}\sqrt{(\omega_1 - \omega_2 - i(\gamma_1 - \gamma_2))^2 + 4g^2}. \tag{6.2}$$

The real portion of ω_{pm} gives the dispersion of the eigenvalues, while the imaginary portion dictates the line width.

To illustrate the distinct coupling regimes, we can fix the resonance frequency of oscillator one, $\omega_1 = const.$, and assume the resonance frequency of oscillator two is equal to $\omega_2 = \omega_1 + \delta\omega$, where $\delta\omega$ is a variable parameter so we can tune the frequency of oscillator two. Furthermore, we will assume the resonance amplitudes of the coupled modes are Lorentzian, i.e.

$$|x_{\pm}(\omega)| \propto \frac{1}{(\omega - \omega_{\pm})^2 + \gamma_{1,2}^2} \tag{6.3}$$

with the choice of $\gamma_{1,2} = \omega_1/5$. Figure 6.2a shows the real portion of Eq. 6.2 for both the uncoupled (dashed lines) and coupled oscillators (solid lines). For the uncoupled and coupled case, we have selected $g = 0$ and $g = 1.5\,\langle\gamma\rangle$, respectively, where $\langle\gamma\rangle = (\gamma_1 + \gamma_2)/2$ i.e. the average value of the dissipation rates. When no coupling is present, the two resonances intersect at $\delta\omega = 0$, but when coupling is introduced, we see the curves no longer intersect, a phenomena known as *anti crossing*. The degree of separation between each curve is found by calculating the difference in the two eigen frequencies at zero detuning, which is equal exactly to g i.e. $|(\omega_+ - \omega_-)|_{\delta\omega=0} = g$. Therefore, we can determine the degree of anti crossing by the value of the coupling constant. The dispersion curves of $\omega_\pm$ do not reveal if we are in the strong or weak coupling regime. To determine this, we need to look at how the magnitude of the dissipation terms compares to the coupling strength. Dissipation terms $\gamma_{1,2}$ will smear out the resonance curves, and if the damping is strong enough, then the anti crossing behavior will not be discernable—this is the weak coupling regime (see Fig. 6.1b). To observe strong coupling, the frequency split (or alternatively, the coupling strength)

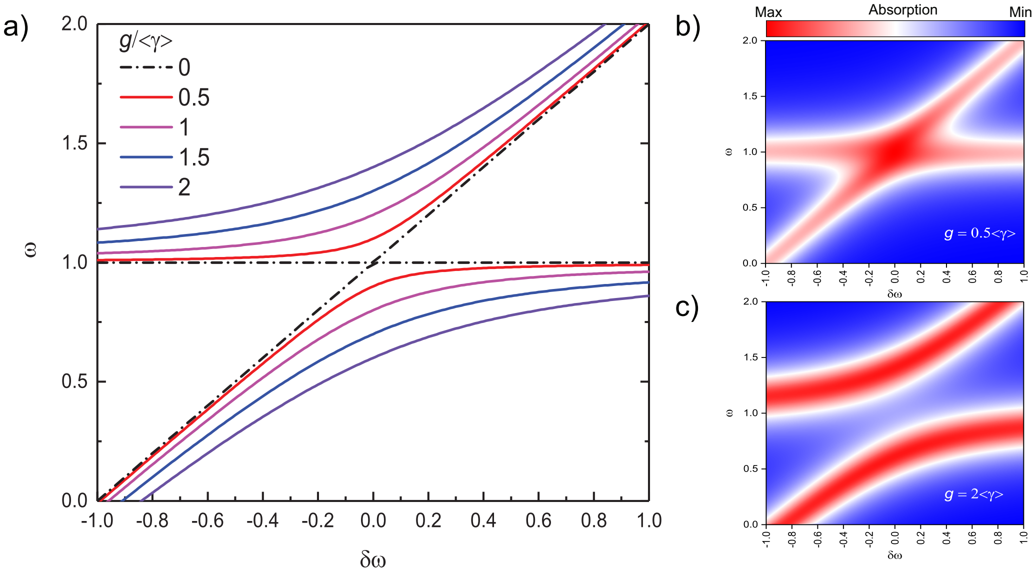

Figure 6.1. Coupled Harmonic Oscillators. (a) Real portion of the complex eigenvalues of two coupled harmonic oscillators as a function of the variable frequency parameter $\delta\omega$ for a coupling constant of $g = 0\langle\gamma\rangle$, $0.5\langle\gamma\rangle$, $1\langle\gamma\rangle$, $1{,}5\langle\gamma\rangle$, and $2\langle\gamma\rangle$. Resonance amplitude of each oscillator in the (b) weak coupling regime, with a coupling parameter $g = 0.5\,\langle\gamma\rangle$, and (c) the strong coupling regime, with a coupling parameter $g = 2.0\,\langle\gamma\rangle$

needs to be greater than the average dissipation rates of the individual oscillators. Quantitatively, this is given by

$$2g > \langle \gamma \rangle = (\gamma_1 + \gamma_2)/2. \tag{6.4}$$

Qualitatively, this implies that the exchange of energy between the two systems is faster than the average decay rate and implies the system is strongly coupled. The frequency at which energy is changed between the two systems is known as the *Rabi Frequency* (Ω_R) and is twice the coupling constant, i.e. ($\Omega_R = 2g$), Figure 6.1c shows the field amplitude of the oscillators in the strong coupling regime; here, it is evident that the splitting is much greater than the dissipation or spectral widths of the oscillators, as compared to Fig. 6.1(b) where the gap is unresolvable.

Although our analysis has been purely classical, we note that a fully quantum mechanical derivation ends in the same results and observable physics [168, 187]. Furthermore, the general consideration of driving forces in Eq. 6.1 leads to a wealth of resonant phenomena. Thus, the classical coupled harmonic oscillator model is extremely robust and applicable to for analyzing ENZ thin films coupled to plasmonic antennas.

6.2 ENZ Mode in Aluminum-doped Zinc Oxide Thin Films

As shown in Fig. 6.2a, the sample consists of gold nanorod antenna arrays deposited onto a 23-nm-thick aluminum-doped zinc oxide (Al:ZnO) film. Al:ZnO films were deposited onto glass substrates using pulsed laser deposition (PVD Products, Inc.). Briefly, a 2wt% doped Al:ZnO target (99.99% purity) target was ablated using a KrF excimer laser (Lambda Phsik, GmbH) operating at a wavelength of 248 nm, an at target fluence of 1.5 J/cm^2, and a repetition rate of 5 Hz. The deposition temperature was fixed at 90° C to set the ENZ wavelength near 1400 nm. Gold antennas were then fabricated on the Al:ZnO film by spin coating positive electron beam resist (ZEP 520 A) at 4000 rpm and then exposed by electron lithography (Vistec VB6). The beam energy and current was 100 kV and 1.012 nA, respectively. We deposited a 30-nm-thick gold film on the resist using electron beam evaporation. The entire sample was then developed in ZED-N50 for 1 minute and then dipped in isopropyl alcohol for 30s to remove remaining ZED-N50. Antenna arrays consisted of nanorods

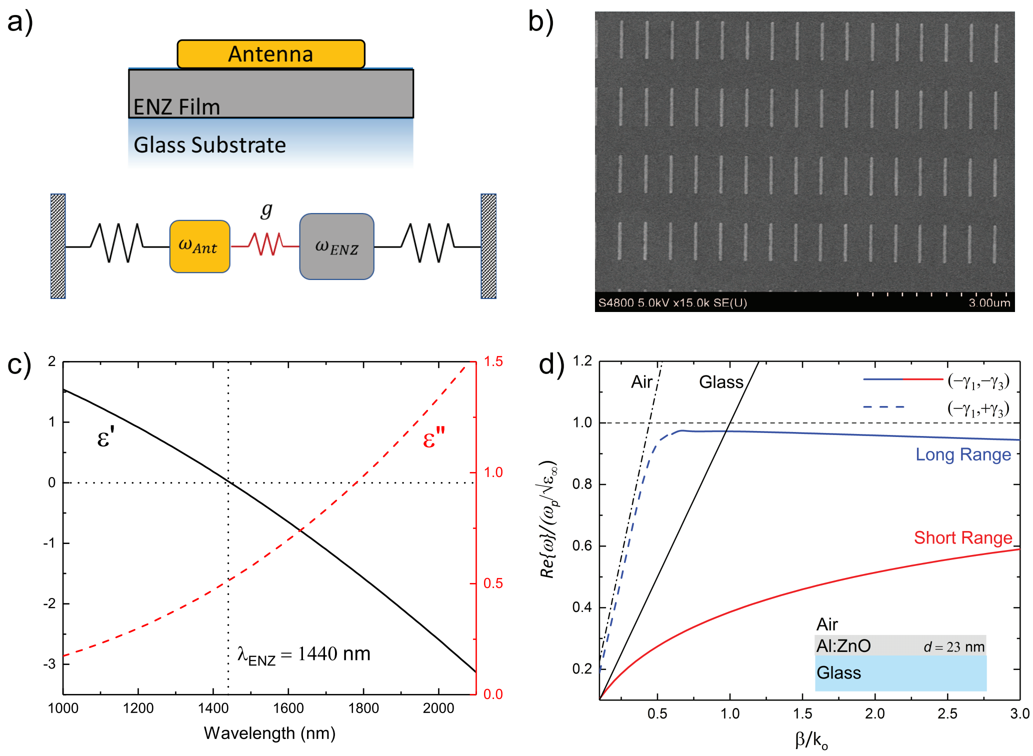

Figure 6.2. Plasmonic-ENZ System. (a) Schematic of the plasmonic antenna on an ENZ film, along with pictorial depiction of the antenna and ENZ film as two coupled harmonic oscillators. (b) SEM image of the gold nanoantennas deposited on a 23-nm-thick Al:ZnO film. (c) Real (black line, left axis) and imaginary (red line, right axis) dielectric constants of the Al:ZnO flim retrieved with spectroscopic ellipsometry, where the ENZ wavelength of 1440 nm is indicated with a dashed black line. (d) Dispersion relation of the air-ENZ-glass three-layered system (see inset). The long (short) range plasmon is indicated with a blue(red) line. The long range plasmon approaches the screened plasma frequency (i.e. ENZ wavelength) for large wavevectors β, as indicated by the nearly flat dispersion. The solid blue line indicates the mode bound to the film, while the dashed blue line is a wave which leaks into the substrate.

of 30 nm thickness, 110 nm widths, and varying lengths of 300, 350, ..., 650 nm; the period of the antenna arrays were set to 800 nm and 1200 nm in the parallel and perpendicular direction, respectively, of the antenna's long axis. Fig. 6.2b shows an exemplary scanning electron microscope image of an array of 600 nm nanorods.

The optical properties of the Al:ZnO film was characterized by spectroscopic ellipsometry (V-Vase, J.A. Woollam) over a spectral range of 800 to 2500 nm. The dielectric constants were retrieved by fitting a Drude oscillator model to the measured ellipsometer parameters (see Fig. 6.2c). We find the bare Al:ZnO film has a ENZ permittivity of $\epsilon_{ENZ} = 0.0 + 0.3i$ at $\lambda_{ENZ} = 1440$ nm. To find the dispersion of the ENZ mode of our bare Al:ZnO film, we solve the following dispersion equation for modes of a three layer structure

$$f(\beta,\omega) = 1 + \frac{\epsilon_1\gamma_3}{\epsilon_3\gamma_1} - i\tan(\kappa d)\left(\frac{\epsilon_2\gamma_3}{\epsilon_3\kappa} + \frac{\epsilon_1\kappa}{\epsilon_2\gamma_1}\right) = 0. \tag{6.5}$$

In Eq. 6.5, ω is the angular frequency, β is the transverse wavenumber, $k_o^2 = \omega^2/c^2$ is the free space wavenumber, $\gamma_{1,3} = \pm\sqrt{\epsilon_{1,3}k_o^2 - \beta^2}$ are the longitudinal wavenumber in the superstrate ($i = 1$) and superstrate ($i = 3$), and $\kappa = \sqrt{\beta^2 - \epsilon_2 k_o^2}$ is the longitudinal wavenumber in the Al:ZnO layer. Here, we choose to solve Eq. 6.5 using a real β, complex ω approach in order to capture the transient radiative decay behavior of the ENZ mode. Solutions of Eq. 6.5 reside on a four-sheet Reimann surface, where each sheet is characterized by a particular choice of $\gamma_{1,3}$ sign. Fig. 6.2d shows solutions of Eq. 6.5 (i.e. dispersion curves) for both modes bound to the Al:ZnO film—($-\gamma_1$,$-\gamma_3$), solid lines—and modes which couple to free-space radiation in the glass substrate—($-\gamma_1$,$+\gamma_3$), dashed lines—in addition to the long (blue lines) and short (red line) range surface plasmons. It is evident that the bound long range mode is an ENZ mode since the dispersion is nearly flat for a large range of transverse wavevectors β near the screened plasma frequency (i.e. plasma wavelength). Note that the transition from "substrate-leaky" to bound modes occur at wavevectors close to the dispersion curve of the glass substrate (Fig. 6.2a, solid black line). Although the film thickness satisfies the necessary condition of an ENZ mode ($t < \lambda_0/50$) [58], the long range mode does not lie exactly at the ENZ frequency as observed for the

2-nm Drude film in Fig. 3.1. Therefore, we expect the resonance of the film to be slightly red-shifted from the exact ENZ wavelength. To investigate the coupling of

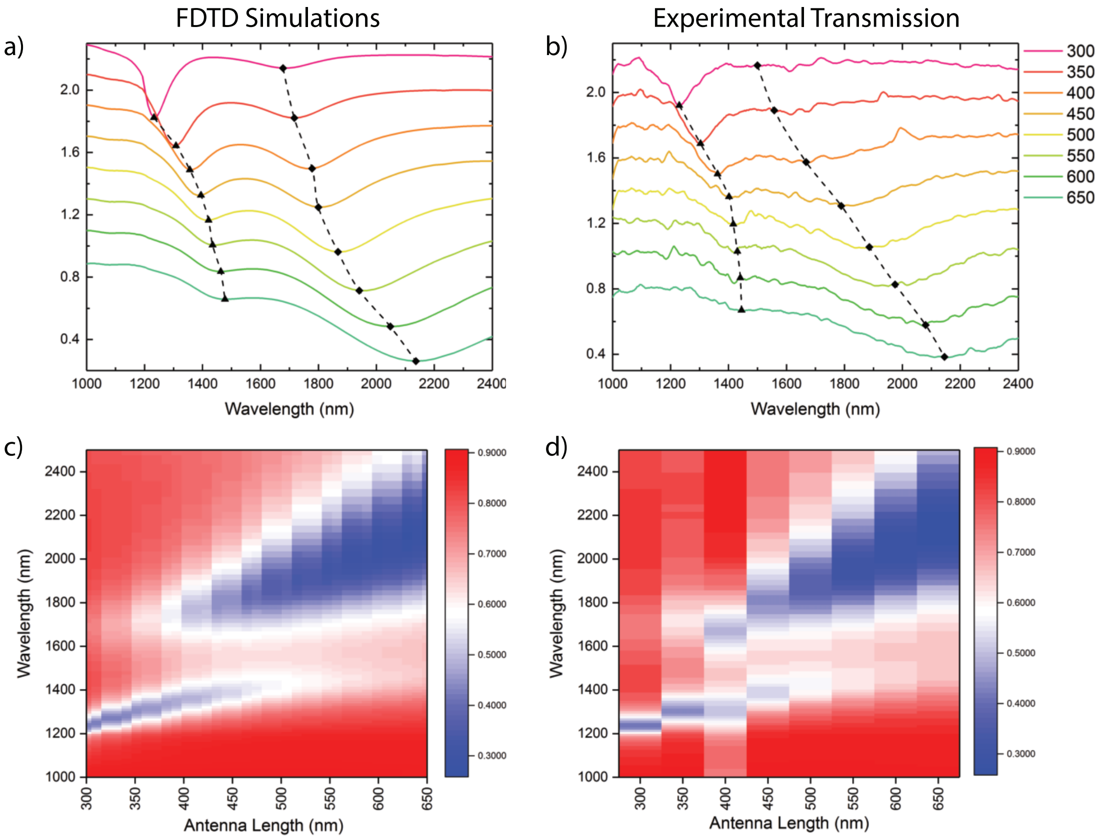

Figure 6.3. Transmission spectra of antennas on ultrathin ENZ film. (a) FDTD and (b) experimental transmission spectra of gold plasmonic antennas on 23 nm-thick Al:ZnO film. Transmission curves correspond to different antenna lengths and are separated for clarity. Triangles and diamonds correspond to the minimum transmission wavelength for the antenna and ENZ mode, respectively. (c) FDTD and (d) experimental color maps of the transmission as a function of antenna length and wavelength. Anti crossing behavior is observed near the ENZ wavelength of 1440 nm.

the plasmonic antenna and the ENZ modes, transmission spectra were collected for antenna arrays of varying lengths using normal incident light polarized along the long axis of the antennas. In addition, 3D finite difference time domain (FDTD) simulations were performed to calculate the theoretical transmission spectrum of the antenna array. Fig. 6.3 shows the numerical (a) and experimental (b) transmission curves for different antenna lengths, separated by a constant offset for clarity. Two resonance dips are observed. The first, shorter wavelength dip corresponds to the antenna resonance, as verified with numerical simulations of antennas on bare glass; the second, longer wavelength dip is the ENZ mode. The transmission minima are marked with triangles (antenna) and diamonds (ENZ) and their shifts are tracked with dotted lines to highlight the splitting behavior of the two modes. Color maps of the resonances for FDTD and experimental transmission measurements are shown in Fig. 6.3(c) and (d), respectively. Here, we can see a strong anti-crossing behavior of the resonance near the ENZ wavelength of 1440 nm with a gap which appears well resolvable from the line widths of the two resonances. Using the coupled harmonic oscillator model, we fit the experimental resonance minimas of both the antenna mode (lower branch) and the ENZ mode (upper branch) to real portion of Eq. 6.2 where the value of g is our variable parameter. The results of our fit are displayed in Fig. 6.4, and we extract a coupling constant of $g = 143.55$ meV (178 nm). Indeed, this coupling constant value satisfies the strong coupling condition (Eq. 6.4) and corresponds to a Rabi frequency of $\Omega_R = 218.39$ THz. The Rabi frequency is the rate at which energy is transfered between the antenna and ENZ mode and, within the strong coupling regime, should be observable as a beating pattern in the electric field in either single oscillator before damping suppresses the resonances. As an estimate, we calculate the ratio of the couping constant and the average decay rate and find $\Omega_R / \langle \gamma \rangle = 2.636$. Therefore, the mode at the strong coupling wavelength should oscillate between the antenna and the ENZ mode roughly three times before the fields dissipate. Experimentally, this feature could be resolved via ultrafast pump-probe studies provided that the probe was short enough to resolve the Rabi oscillations in either the antenna or ENZ mode. We can estimate the pulse width by calculating the period of Rabi oscillations as $T_R = 2\pi/\Omega_R = 28.7$ fs. Sub-20-fs pulses are easily

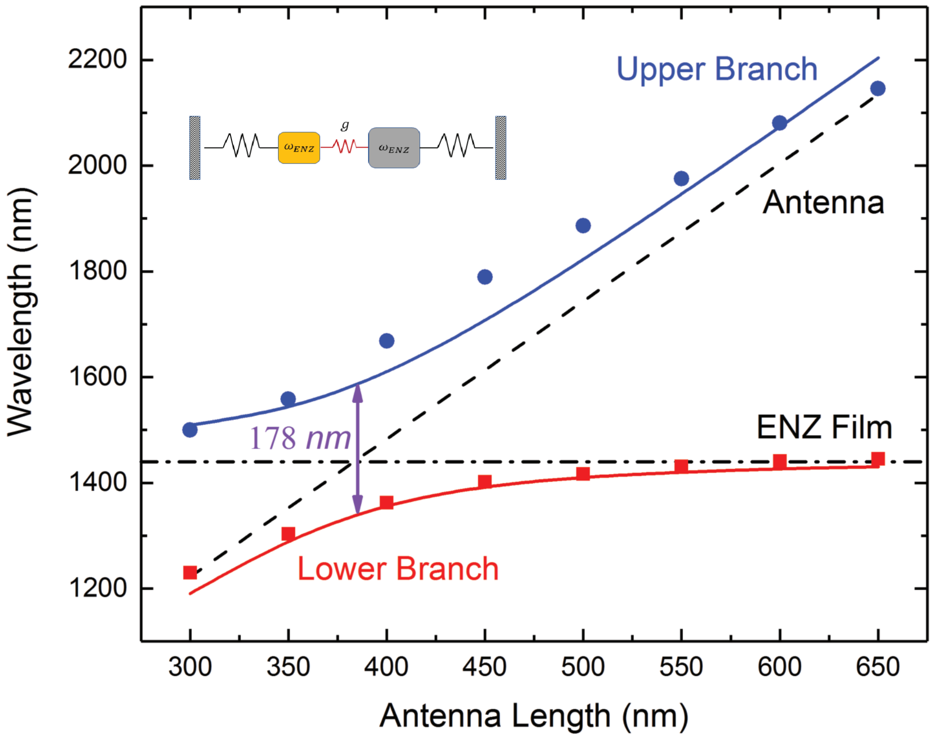

Figure 6.4. Wavelengths of the transmission minimum as a function of antenna length. Blue (Red) dots: minimum experimental transmission of ENZ (antenna) mode . Blue (Red) line: theoretical fit of the coupled harmonic oscillator model to the ENZ (antenna) mode. Black horizontal dashed (dashed dot) line: uncoupled resonance wavelength of the ENZ (antenna) mode. Extracted g value (in wavelengths) indicated by the purple arrow at the anti crossing point. Inset shows the pictorial description of the coupled harmonic oscillator model.

achieved using highly compressed broadband sources, so it is conceivable to measure these Rabi oscillations directly.

The coupling mechanism between the antenna and ENZ film is the overlap of the film with the antenna's electric field z-component (E_z). The dispersion of the ENZ mode (Fig. 6.3d) indicates a large spectrum of transverse momentum components

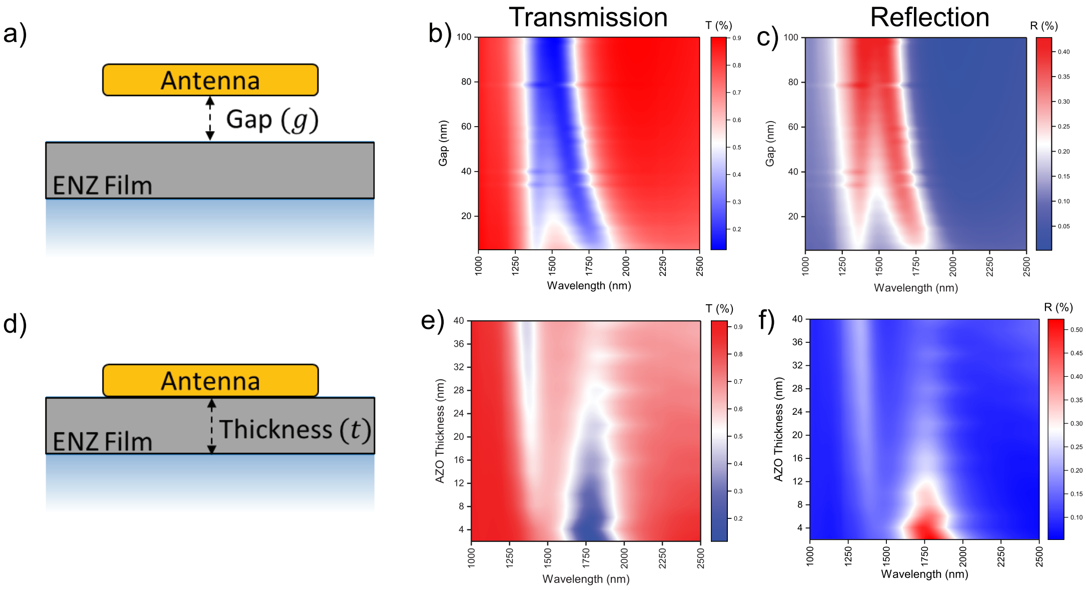

Figure 6.5. FDTD transmission and reflection spectra of ENZ-nanorod array. (a) Illustration of FDTD simulation for varying gap sizes. (b) Transmission and (c) reflection of ENZ-nanorod array as a function of the distance (d) between the antenna and the ENZ film. (d) Illustration of FDTD simulations for varying ENZ film thickness. (e) Transmission and (f) reflection of ENZ-nanorod array as a function of varying ENZ film thickness.

(β) are supported at the ENZ frequency beyond the light-line of both air and glass. These momentum correspond to strong gradients and highly confined z-components of the electric field. In the near-field vicinity of a plasmonic antennas, the scattered field is primary radial and the fields support large wave vectors. Therefore, we expect the coupling to be strongly dependent on the antenna-to-ENZ film distance (d). We numerically investigate this feature by performing FDTD simulations of $L = 400$ nm antennas (anti crossing length) with a varying antenna-ENZ film gap distance (schematic shown in Fig. 6.5(a)). In Fig. 6.5, we plot color maps of both the transmission (a) and reflection (b) of the antenna array for increasing gap distance. For distances greater than 15 nm, the strong coupling condition is no longer satisfied and the two resonances are no longer resolvable. As a second numerical test, we vary the thickness of the ENZ layer (schematic shown in Fig. 6.5d). For larger film thickness, the ENZ mode no longer supports a broad range of transverse momentum at the ENZ frequency, so the antenna will not couple effectively. An alternative picture is based on field penetration. For larger thickness, the electric field of the antenna will no longer penetrate to the opposite interface and the resulting surface charge density will be insufficient to provide a strong restoring force to support the oscillations. Fig. 6.5 shows transmission (e) and reflection(f) color maps of the $L = 400$ nm antenna array for varying film thickness. In contrast to variation of gap distance, the separation between the resonances grows with film thickness; however, the ENZ mode exhibits a strong decay in amplitude for larger thickness. The latter of these effects agrees, at least qualitatively, well with our understanding of field penetration decay for thicker films. What is interesting is both the observation of a linear increase in the mode splitting and the periodic beating pattern of the ENZ resonance. The origin of these effects remain to be understood and will be studied in future experiments.

6.3 Conclusions

In summary, we have demonstrated strong coupling between plasmonic antennas and ENZ modes supported by an ultrathin film of Al:ZnO. The system has a Rabi frequency of $\Omega_R = 218.39$ THz, which is 2.636 times larger than the systems average dissipation rates. Therefore, we expect these oscillations should be observable with ultrafast pump-probe experiments, provided the probe width is less than 20 fs. We have shown that sufficient electric field z-components are necessary for efficient coupling into the ENZ mode. Our results are general, and we expect similar strong coupling phenomena are present in any near-field scattering element and an ENZ film. Improved coupling is possible by either engineering the scatterer to provide large momentum components, or alternatively, by reducing the loss in either the ENZ film or scattering element. The former possibility could be achieved by moving into the mid-infrared wavelengths where losses in materials such as SiC are considerably smaller than TCOs; alternatively, TCOs such as dysprosium-doped cadmium oxide have been shown to have losses smaller than either Al:ZnO, Ga:ZnO or ITO. Losses in the scattering element could also be reduced with dielectric antennas, which have extremely narrow line widths but lower electric field amplitudes. This trade off between loss and field amplitude in dielectric resonators is the direction of future studies.

A further direction for consideration is utilizing this system for enhancing nonlinear interactions in the TCO. As we have already seen, the nonlinear enhancement is directly related to the strength of the optical field inside the TCO layer. However, coupling into this layer is difficult unless operating at the angle corresponding to the FIE maximum. Plasmon antennas which are strongly coupled to the ENZ mode provide a direct method for cycling large fields into the TCO layer though the Rabi oscillations. Evidence for this effect has already been suggested in a study of similar antennas on a thin ITO layer [76]. However, it remains a substantial challenge to not only understand theoretically if the nonlinear enhancement is possible, but to optimize the antenna coupling. Antennas which generate strong near-field components could potentially maximize the coupling. Alternatively, TCOs with lower loss factors would sustain the Rabi oscillations for longer periods of time, thereby increasing the interaction time.

7. OUTLOOK AND CONCLUSIONS

This thesis has focused on the study of epsilon-near-zero ultrafast, nonlinear, and strongly coupled physics utilizing transparent conducting oxide platforms. Its content provides a comprehensive discourse of my primary PhD research and reflects my attempt at a coherent illustration of ENZ phenomena and applications. At this point, I wish to depart from a standard summary—the information is found at each chapter's end—and focus on future directions for TCO-based ENZ research.

A central theme of epsilon-near-zero effects in transparent conducting oxides is their optical loss. The physical origin of loss in a TCO is electron scattering, predominately from crystal defects present in the lattice. Unfortunately, as we have discussed, defects are a necessary evil to induce a sufficient carrier density and achieve plasma frequencies at the high-energy spectrum of the infrared [29, 31]. Careful balance of crystallinity and dopant concentrations is a promising route for achieving low-loss TCOs, as recenly shown in crystalline Ga:ZnO on sapphire [188–190] and doped cadmium oxides [71, 191]. Unfortunately, these materials still can not achieve ENZ wavelengths less than 2000 nm, (i.e. carrier concentrations greater than 10^{22} cm^{-3}). To date, the concentrations achieved in crystalline oxides are only achievable in heavily-doped, poly-crystalline metal oxide films which have defect states (e.g. oxygen and hydrogen) which contribute additional free carriers—along with loss. However, novel conducting oxides continue to develope at a prolific rate, and with modern advancements in both fabrication and theoretical modeling of complex material, it is possible that a low-loss, visibile/near-infrared ENZ platform is achievable.

An alternatively approach to mitigating loss is to accept the low carrier concentrations and develop TCOs for ENZ applications at mid-infrared wavelengths. Here, optical loss is bound by Landau damping, which is modest at low carrier concentrations [192, 193]. Although near-infrared wavelengths are the predominant choice for telecommunication applications, the mid-infrared spectrum pertains to phenomena such as blackbody radiation. Here, TCOs with a mid-infrared ENZ wavelength could be used for controlling and manipulating thermal radiation. Indeed, recent work has demonstrated the potential to tailor the spectral emission of a hot ENZ material [69]. It may even be possible to control this response on an ultrafast scale utilizing the femtosecond recombination rates of conducting oxides.

Beyond materials, we have emphasized the application of ENZ for enhancing a broad range of nonlinear interactions. It should be noted that one key reason for the enhancement of the nonlinear phenomena should be the reduction in group-velocity as we have discussed in Chapter 3. Essentially, a near-zero permittivity material will efficiently capture the optical field energy, allowing for an increased light-matter interaction [96]. Slow-light nonlinear enhancement is largely unexplored experimentally and is, therefore, a pertinent feature of future nonlinear ENZ research.

From an experimentalist's point of view and as a closing comment, a thorough theoretical description of the nonlinear enhancement in various ENZ materials would greatly benefit future research. Namely, it remains an open question as to whether perturbation theory applies when the nonlinear corrections are comparable to the linear terms [77,81,82]. In addition, there is likely a significant non-local contribution, especially in ultrathin films supporting ENZ/Berrreman modes, near the crossover wavelength which has yet to be investigated. Hydrodynamic models which account for both nonlinear and non-local contributions in dilute plasma could possibly provide deeper insight into these questions [86, 194–196].

From an application point of view, ENZ-enhanced nonlinearities represent a very exciting research direction. The large nonlinearities which have been observed in TCO films could potentially enable extremely fast and efficient modulators for on-chip nanophotonic applications where ultra-small propagation lengths mitigate the inherent loss factor [77]. Combining ENZ materials with resonant structures may provide avenues for the exploration of strong coupling, which may be useful for controlling emission and for further enhancing the tunability of devices. Particularly, it would be interesting to explore LI strong coupling in the context of Fano Resonances, Embedded Eigenstates, and Bound States in the Continuum for photonic and plasmonic systems where loss versus coupling strength can be controlled [185, 197, 198]. ENZ can be seen as a unique platform to couple materials development with optical science to advance both fundamental and application-driven research.

REFERENCES

REFERENCES

[1] Max Born and Emil Wolf. *Principles of optics: electromagnetic theory of propagation, interference and diffraction of light*. Elsevier, 2013.

[2] Grant R Fowles. *Introduction to modern optics*. Courier Corporation, 1989.

[3] Eugene Hecht. Optics, 4th. *International edition, Addison-Wesley, San Francisco*, 3:2, 2002.

[4] Bahaa EA Saleh, Malvin Carl Teich, and Bahaa E Saleh. *Fundamentals of photonics*, volume 22. Wiley New York, 1991.

[5] John D Joannopoulos, Steven G Johnson, Joshua N Winn, and Robert D Meade. *Photonic crystals: molding the flow of light*. Princeton university press, 2011.

[6] David R Smith, Willie J Padilla, DC Vier, Syrus C Nemat-Nasser, and Seldon Schultz. Composite medium with simultaneously negative permeability and permittivity. *Physical review letters*, 84(18):4184, 2000.

[7] Richard W Ziolkowski and Ehud Heyman. Wave propagation in media having negative permittivity and permeability. *Physical review E*, 64(5):056625, 2001.

[8] John Brian Pendry. Negative refraction makes a perfect lens. *Physical review letters*, 85(18):3966, 2000.

[9] Vladimir M Shalaev, Wenshan Cai, Uday K Chettiar, Hsiao-Kuan Yuan, Andrey K Sarychev, Vladimir P Drachev, and Alexander V Kildishev. Negative index of refraction in optical metamaterials. *Optics letters*, 30(24):3356–3358, 2005.

[10] Muhan Choi, Seung Hoon Lee, Yushin Kim, Seung Beom Kang, Jonghwa Shin, Min Hwan Kwak, Kwang-Young Kang, Yong-Hee Lee, Namkyoo Park, and Bumki Min. A terahertz metamaterial with unnaturally high refractive index. *Nature*, 470(7334):369, 2011.

[11] Jung-Tsung Shen, Peter B Catrysse, and Shanhui Fan. Mechanism for designing metallic metamaterials with a high index of refraction. *Physical review letters*, 94(19):197401, 2005.

[12] DC Adams, Sandeep Inampudi, T Ribaudo, D Slocum, S Vangala, NA Kuhta, WD Goodhue, Viktor A Podolskiy, and D Wasserman. Funneling light through a subwavelength aperture with epsilon-near-zero materials. *Physical review letters*, 107(13):133901, 2011.

[13] N Garcia, EV Ponizovskaya, and John Q Xiao. Zero permittivity materials: Band gaps at the visible. *Applied physics letters*, 80(7):1120–1122, 2002.

[14] Richard W Ziolkowski. Propagation in and scattering from a matched metamaterial having a zero index of refraction. *Physical Review E*, 70(4):046608, 2004.

[15] Mário Silveirinha and Nader Engheta. Tunneling of electromagnetic energy through subwavelength channels and bends using ε-near-zero materials. *Physical review letters*, 97(15):157403, 2006.

[16] Mário G Silveirinha and Nader Engheta. Theory of supercoupling, squeezing wave energy, and field confinement in narrow channels and tight bends using ε near-zero metamaterials. *Physical Review B*, 76(24):245109, 2007.

[17] Mário Silveirinha and Nader Engheta. Design of matched zero-index metamaterials using nonmagnetic inclusions in epsilon-near-zero media. *Physical Review B*, 75(7):075119, 2007.

[18] Andrea Alù and Nader Engheta. Light squeezing through arbitrarily shaped plasmonic channels and sharp bends. *Physical Review B*, 78(3):035440, 2008.

[19] Andrea Alu, Mário G Silveirinha, Alessandro Salandrino, and Nader Engheta. Epsilon-near-zero metamaterials and electromagnetic sources: Tailoring the radiation phase pattern. *Physical review B*, 75(15):155410, 2007.

[20] Christos Argyropoulos, Pai-Yen Chen, Giuseppe DAguanno, Nader Engheta, and Andrea Alu. Boosting optical nonlinearities in ε-near-zero plasmonic channels. *Physical Review B*, 85(4):045129, 2012.

[21] Ruopeng Liu, Qiang Cheng, Thomas Hand, Jack J Mock, Tie Jun Cui, Steven A Cummer, and David R Smith. Experimental demonstration of electromagnetic tunneling through an epsilon-near-zero metamaterial at microwave frequencies. *Physical review letters*, 100(2):023903, 2008.

[22] Brian Edwards, Andrea Alù, Michael E Young, Mário Silveirinha, and Nader Engheta. Experimental verification of epsilon-near-zero metamaterial coupling and energy squeezing using a microwave waveguide. *Physical review letters*, 100(3):033903, 2008.

[23] Ernst Jan R Vesseur, Toon Coenen, Humeyra Caglayan, Nader Engheta, and Albert Polman. Experimental verification of n= 0 structures for visible light. *Physical review letters*, 110(1):013902, 2013.

[24] Ruben Maas, James Parsons, Nader Engheta, and Albert Polman. Experimental realization of an epsilon-near-zero metamaterial at visible wavelengths. *Nature Photonics*, 7(11):nphoton–2013, 2013.

[25] Yang Li, Shota Kita, Philip Muñoz, Orad Reshef, Daryl I Vulis, Mei Yin, Marko Lončar, and Eric Mazur. On-chip zero-index metamaterials. *Nature Photonics*, 9(11):738, 2015.

[26] Saman Jahani and Zubin Jacob. All-dielectric metamaterials. *Nature nanotechnology*, 11(1):23, 2016.

[27] Parikshit Moitra, Yuanmu Yang, Zachary Anderson, Ivan I Kravchenko, Dayrl P Briggs, and Jason Valentine. Realization of an all-dielectric zero-index optical metamaterial. *Nature Photonics*, 7(10):791, 2013.

[28] Gururaj V Naik, Vladimir M Shalaev, and Alexandra Boltasseva. Alternative plasmonic materials: beyond gold and silver. *Advanced Materials*, 25(24):3264–3294, 2013.

[29] Gururaj V Naik, Jongbum Kim, and Alexandra Boltasseva. Oxides and nitrides as alternative plasmonic materials in the optical range. *Optical Materials Express*, 1(6):1090–1099, 2011.

[30] Viktoriia E Babicheva, Nathaniel Kinsey, Gururaj V Naik, Marcello Ferrera, Andrei V Lavrinenko, Vladimir M Shalaev, and Alexandra Boltasseva. Towards cmos-compatible nanophotonics: Ultra-compact modulators using alternative plasmonic materials. *Optics express*, 21(22):27326–27337, 2013.

[31] Paul R West, Satoshi Ishii, Gururaj V Naik, Naresh K Emani, Vladimir M Shalaev, and Alexandra Boltasseva. Searching for better plasmonic materials. *Laser & Photonics Reviews*, 4(6):795–808, 2010.

[32] Brian G Lewis and David C Paine. Applications and processing of transparent conducting oxides. *MRS bulletin*, 25(8):22–27, 2000.

[33] David S Ginley and Clark Bright. Transparent conducting oxides. *MRS bulletin*, 25(8):15–18, 2000.

[34] Roy G Gordon. Criteria for choosing transparent conductors. *MRS bulletin*, 25(8):52–57, 2000.

[35] Kenji Nomura, Hiromichi Ohta, Akihiro Takagi, Toshio Kamiya, Masahiro Hirano, and Hideo Hosono. Room-temperature fabrication of transparent flexible thin-film transistors using amorphous oxide semiconductors. *Nature*, 432(7016):488, 2004.

[36] Stephan Lany and Alex Zunger. Dopability, intrinsic conductivity, and nonstoichiometry of transparent conducting oxides. *Physical Review Letters*, 98(4):045501, 2007.

[37] Xinge Yu, Tobin J Marks, and Antonio Facchetti. Metal oxides for optoelectronic applications. *Nature materials*, 15(4):383, 2016.

[38] Alexandra Boltasseva and Harry A Atwater. Low-loss plasmonic metamaterials. *Science*, 331(6015):290–291, 2011.

[39] Stefan Alexander Maier. *Plasmonics: fundamentals and applications*. Springer Science & Business Media, 2007.

[40] Dmitri K Gramotnev and Sergey I Bozhevolnyi. Plasmonics beyond the diffraction limit. *Nature photonics*, 4(2):83, 2010.

[41] Jon A Schuller, Edward S Barnard, Wenshan Cai, Young Chul Jun, Justin S White, and Mark L Brongersma. Plasmonics for extreme light concentration and manipulation. *Nature materials*, 9(3):193, 2010.

[42] Justus C Ndukaife, Vladimir M Shalaev, and Alexandra Boltasseva. Plasmonicsturning loss into gain. *Science*, 351(6271):334–335, 2016.

[43] Kevin F MacDonald, Zsolt L Sámson, Mark I Stockman, and Nikolay I Zheludev. Ultrafast active plasmonics. *Nature Photonics*, 3(1):55, 2009.

[44] Marcello Ferrera, Nathaniel Kinsey, Amr Shaltout, Clayton DeVault, Vladimir Shalaev, and Alexandra Boltasseva. Dynamic nanophotonics. *JOSA B*, 34(1):95–103, 2017.

[45] Sergey V Makarov, Anastasia S Zalogina, Mohammad Tajik, Dmitry A Zuev, Mikhail V Rybin, Aleksandr A Kuchmizhak, Saulius Juodkazis, and Yuri Kivshar. Light-induced tuning and reconfiguration of nanophotonic structures. *Laser & Photonics Reviews*, 11(5):1700108, 2017.

[46] Gregory J Exarhos and Xiao-Dong Zhou. Discovery-based design of transparent conducting oxide films. *Thin solid films*, 515(18):7025–7052, 2007.

[47] Douglas H Lowndes, DB Geohegan, AA Puretzky, DP Norton, and CM Rouleau. Synthesis of novel thin-film materials by pulsed laser deposition. *Science*, 273(5277):898–903, 1996.

[48] Anderson Janotti and Chris G Van de Walle. Oxygen vacancies in zno. *Applied Physics Letters*, 87(12):122102, 2005.

[49] Anderson Janotti and Chris G Van de Walle. Native point defects in zno. *Physical Review B*, 76(16):165202, 2007.

[50] Neil W Ashcroft and N David Mermin. *Solid state physics*. Holt, Rinehart and Winston, 1976.

[51] J David Jackson. *Electrodynamics*. Wiley Online Library, 1975.

[52] Hiroyuki Fujiwara. *Spectroscopic ellipsometry: principles and applications*. John Wiley & Sons, 2007.

[53] Rohit P Prasankumar and Antoinette J Taylor. *Optical techniques for solid-state materials characterization*. CRC Press, 2016.

[54] Peter B Johnson and R-W_ Christy. Optical constants of the noble metals. *Physical review B*, 6(12):4370, 1972.

[55] Yu-Jung Lu, Ruzan Sokhoyan, Wen-Hui Cheng, Ghazaleh Kafaie Shirmanesh, Artur R Davoyan, Ragip A Pala, Krishnan Thyagarajan, and Harry A Atwater. Dynamically controlled purcell enhancement of visible spontaneous emission in a gated plasmonic heterostructure. *Nature Communications*, 8(1):1631, 2017.

[56] Inigo Liberal and Nader Engheta. Near-zero refractive index photonics. *Nature Photonics*, 11(3):149, 2017.

[57] Simon Vassant, Jean-Paul Hugonin, Francois Marquier, and Jean-Jacques Greffet. Berreman mode and epsilon near zero mode. *Optics express*, 20(21):23971–23977, 2012.

[58] Salvatore Campione, Igal Brener, and Francois Marquier. Theory of epsilon-near-zero modes in ultrathin films. *Physical Review B*, 91(12):121408, 2015.

[59] Kosmas L Tsakmakidis, Tim W Pickering, Joachim M Hamm, A Freddie Page, and Ortwin Hess. Completely stopped and dispersionless light in plasmonic waveguides. *Physical review letters*, 112(16):167401, 2014.

[60] Pierre Berini. Long-range surface plasmon polaritons. *Advances in optics and photonics*, 1(3):484–588, 2009.

[61] JJ Burke, GI Stegeman, and T Tamir. Surface-polariton-like waves guided by thin, lossy metal films. *Physical Review B*, 33(8):5186, 1986.

[62] Thierry Taliercio, Vilianne Ntsame Guilengui, Laurent Cerutti, Eric Tournié, and Jean-Jacques Greffet. Brewster mode in highly doped semiconductor layers: an all-optical technique to monitor doping concentration. *Optics express*, 22(20):24294–24303, 2014.

[63] William H Press, Saul A Teukolsky, William T Vetterling, and Brian P Flannery. *Numerical recipes 3rd edition: The art of scientific computing*. Cambridge university press, 2007.

[64] Aref Bakhtazad, Habibollah Abiri, and R Ghayour. A general transform for regularizing planar open waveguide dispersion relation. *Journal of lightwave technology*, 15(2):383–390, 1997.

[65] Chengkun Chen, Pierre Berini, Dazeng Feng, Stoyan Tanev, and Velko P Tzolov. Efficient and accurate numerical analysis of multilayer planar optical waveguides in lossy anisotropic media. *Optics Express*, 7(8):260–272, 2000.

[66] Tobin A Driscoll, Nicholas Hale, and Lloyd N Trefethen. Chebfun guide, 2014.

[67] Ting S Luk, Salvatore Campione, Iltai Kim, Simin Feng, Young Chul Jun, Sheng Liu, Jeremy B Wright, Igal Brener, Peter B Catrysse, Shanhui Fan, et al. Directional perfect absorption using deep subwavelength low-permittivity films. *Physical Review B*, 90(8):085411, 2014.

[68] L Nordin, O Dominguez, CM Roberts, W Streyer, K Feng, Z Fang, VA Podolskiy, AJ Hoffman, and D Wasserman. Mid-infrared epsilon-near-zero modes in ultra-thin phononic films. *Applied Physics Letters*, 111(9):091105, 2017.

[69] Young Chul Jun, Ting S Luk, A Robert Ellis, John F Klem, and Igal Brener. Doping-tunable thermal emission from plasmon polaritons in semiconductor epsilon-near-zero thin films. *Applied Physics Letters*, 105(13):131109, 2014.

[70] Jura Rensberg, You Zhou, Steffen Richter, Chenghao Wan, Shuyan Zhang, Philipp Schöppe, Rüdiger Schmidt-Grund, Shriram Ramanathan, Federico Capasso, Mikhail A Kats, et al. Epsilon-near-zero substrate engineering for ultrathin-film perfect absorbers. *Physical Review Applied*, 8(1):014009, 2017.

[71] Yuanmu Yang, Kyle Kelley, Edward Sachet, Salvatore Campione, Ting S Luk, Jon-Paul Maria, Michael B Sinclair, and Igal Brener. Femtosecond optical polarization switching using a cadmium oxide-based perfect absorber. *Nature Photonics*, 11(6):390, 2017.

[72] Aleksei Anopchenko, Long Tao, Catherine Arndt, and Ho Wai Howard Lee. Field-effect tunable and broadband epsilon-near-zero perfect absorbers with deep subwavelength thickness. *ACS Photonics*, 2018.

[73] Salvatore Campione, Joel R Wendt, Gordon A Keeler, and Ting S Luk. Near-infrared strong coupling between metamaterials and epsilon-near-zero modes in degenerately doped semiconductor nanolayers. *Acs Photonics*, 3(2):293–297, 2016.

[74] Young Chul Jun, John Reno, Troy Ribaudo, Eric Shaner, Jean-Jacques Greffet, Simon Vassant, Francois Marquier, Mike Sinclair, and Igal Brener. Epsilon-near-zero strong coupling in metamaterial-semiconductor hybrid structures. *Nano letters*, 13(11):5391–5396, 2013.

[75] Nikolai Christian Passler, Christopher R Gubbin, Thomas Folland, Ilya Razdolski, D Scott Katzer, David F Storm, Martin Wolf, Simone De Liberato, Joshua D Caldwell, and Alexander Paarmann. Strong coupling of epsilon-near-zero phonon polaritons in polar dielectric heterostructures. *Nano letters*, 2018.

[76] M Zahirul Alam, Sebastian A Schulz, Jeremy Upham, Israel De Leon, and Robert W Boyd. Large optical nonlinearity of nanoantennas coupled to an epsilon-near-zero material. *Nature Photonics*, 12(2):79, 2018.

[77] M Zahirul Alam, Israel De Leon, and Robert W Boyd. Large optical nonlinearity of indium tin oxide in its epsilon-near-zero region. *Science*, page aae0330, 2016.

[78] Nicolaas Bloembergen. *Nonlinear optics*. World Scientific, 1996.

[79] Robert W Boyd. *Nonlinear optics*. Elsevier, 2003.

[80] Peter E Powers and Joseph W Haus. *Fundamentals of nonlinear optics*. CRC Press, 2017.

[81] Lucia Caspani, RPM Kaipurath, Matteo Clerici, Marcello Ferrera, Thomas Roger, J Kim, Nathaniel Kinsey, Monika Pietrzyk, Andrea Di Falco, Vladimir M Shalaev, et al. Enhanced nonlinear refractive index in ε-near-zero materials. *Physical review letters*, 116(23):233901, 2016.

[82] Orad Reshef, Enno Giese, M Zahirul Alam, Israel De Leon, Jeremy Upham, and Robert W Boyd. Beyond the perturbative description of the nonlinear optical response of low-index materials. *Optics letters*, 42(16):3225–3228, 2017.

[83] Carsten Brée, Ayhan Demircan, and Günter Steinmeyer. Kramers-kronig relations and high-order nonlinear susceptibilities. *Physical Review A*, 85(3):033806, 2012.

[84] Salvatore Campione, Domenico de Ceglia, Maria Antonietta Vincenti, Michael Scalora, and Filippo Capolino. Electric field enhancement in -near-zero slabs under tm-polarized oblique incidence. *Physical Review B*, 87(3):035120, 2013.

[85] Antonio Capretti, Yu Wang, Nader Engheta, and Luca Dal Negro. Comparative study of second-harmonic generation from epsilon-near-zero indium tin oxide and titanium nitride nanolayers excited in the near-infrared spectral range. *Acs Photonics*, 2(11):1584–1591, 2015.

[86] Domenico de Ceglia, Salvatore Campione, Maria Antonietta Vincenti, Filippo Capolino, and Michael Scalora. Low-damping epsilon-near-zero slabs: Nonlinear and nonlocal optical properties. *Physical Review B*, 87(15):155140, 2013.

[87] MA Vincenti, M Kamandi, D de Ceglia, C Guclu, M Scalora, and F Capolino. Second-harmonic generation in longitudinal epsilon-near-zero materials. *Physical Review B*, 96(4):045438, 2017.

[88] David A Powell, Andrea Alù, Brian Edwards, Ashkan Vakil, Yuri S Kivshar, and Nader Engheta. Nonlinear control of tunneling through an epsilon-near-zero channel. *Physical Review B*, 79(24):245135, 2009.

[89] Haim Suchowski, Kevin OBrien, Zi Jing Wong, Alessandro Salandrino, Xiaobo Yin, and Xiang Zhang. Phase mismatch–free nonlinear propagation in optical zero-index materials. *Science*, 342(6163):1223–1226, 2013.

[90] Nadia Mattiucci, Mark J Bloemer, and Giuseppe DAguanno. Phase-matched second harmonic generation at the dirac point of a 2-d photonic crystal. *Optics Express*, 22(6):6381–6390, 2014.

[91] Jongbum Kim, Aveek Dutta, Gururaj V Naik, Alexander J Giles, Francisco J Bezares, Chase T Ellis, Joseph G Tischler, Ahmed M Mahmoud, Humeyra Caglayan, Orest J Glembocki, et al. Role of epsilon-near-zero substrates in the optical response of plasmonic antennas. *Optica*, 3(3):339–346, 2016.

[92] Prasad P Iyer, Mihir Pendharkar, Chris J Palmstrøm, and Jon A Schuller. Ultrawide thermal free-carrier tuning of dielectric antennas coupled to epsilon-near-zero substrates. *Nature communications*, 8(1):472, 2017.

[93] Sebastian A Schulz, Asad A Tahir, M Zahirul Alam, Jeremy Upham, Israel De Leon, and Robert W Boyd. Optical response of dipole antennas on an epsilon-near-zero substrate. *Physical Review A*, 93(6):063846, 2016.

[94] Iñigo Liberal, Ahmed M Mahmoud, and Nader Engheta. Geometry-invariant resonant cavities. *Nature communications*, 7:10989, 2016.

[95] Stefano Vezzoli, Vincenzo Bruno, Clayton DeVault, Thomas Roger, Vladimir M Shalaev, Alexandra Boltasseva, Marcello Ferrera, Matteo Clerici, Audrius Dubietis, and Daniele Faccio. Optical time reversal from time-dependent epsilon-near-zero media. *Physical review letters*, 120(4):043902, 2018.

[96] Mohammad H Javani and Mark I Stockman. Real and imaginary properties of epsilon-near-zero materials. *Physical review letters*, 117(10):107404, 2016.

[97] Andrea Marini and FJ García De Abajo. Self-organization of frozen light in near-zero-index media with cubic nonlinearity. *Scientific reports*, 6:20088, 2016.

[98] Alessandro Ciattoni, Andrea Marini, Carlo Rizza, Michael Scalora, and Fabio Biancalana. Polariton excitation in epsilon-near-zero slabs: Transient trapping of slow light. *Physical Review A*, 87(5):053853, 2013.

[99] G DAguanno, N Mattiucci, MJ Bloemer, R Trimm, N Aközbek, and A Alù. Frozen light in a near-zero index metasurface. *Physical Review B*, 90(5):054202, 2014.

[100] SE Harris and Lene Vestergaard Hau. Nonlinear optics at low light levels. *Physical Review Letters*, 82(23):4611, 1999.

[101] Jacob B Khurgin. Slow light in various media: a tutorial. *Advances in Optics and Photonics*, 2(3):287–318, 2010.

[102] Maxim R Shcherbakov, Polina P Vabishchevich, Alexander S Shorokhov, Katie E Chong, Duk-Yong Choi, Isabelle Staude, Andrey E Miroshnichenko, Dragomir N Neshev, Andrey A Fedyanin, and Yuri S Kivshar. Ultrafast all-optical switching with magnetic resonances in nonlinear dielectric nanostructures. *Nano Letters*, 15(10):6985–6990, 2015.

[103] Alexander S Shorokhov, Elizaveta V Melik-Gaykazyan, Daria A Smirnova, Ben Hopkins, Katie E Chong, Duk-Yong Choi, Maxim R Shcherbakov, Andrey E Miroshnichenko, Dragomir N Neshev, Andrey A Fedyanin, et al. Multifold enhancement of third-harmonic generation in dielectric nanoparticles driven by magnetic fano resonances. *Nano letters*, 16(8):4857–4861, 2016.

[104] Arseniy I Kuznetsov, Andrey E Miroshnichenko, Mark L Brongersma, Yuri S Kivshar, and Boris Lukyanchuk. Optically resonant dielectric nanostructures. *Science*, 354(6314):aag2472, 2016.

[105] Xueqin Huang, Yun Lai, Zhi Hong Hang, Huihuo Zheng, and CT Chan. Dirac cones induced by accidental degeneracy in photonic crystals and zero-refractive-index materials. *Nature materials*, 10(8):582, 2011.

[106] Hodjat Hajian, Ekmel Ozbay, and Humeyra Caglayan. Enhanced transmission and beaming via a zero-index photonic crystal. *Applied Physics Letters*, 109(3):031105, 2016.

[107] Igor I Smolyaninov, Vera N Smolyaninova, Alexander V Kildishev, and Vladimir M Shalaev. Anisotropic metamaterials emulated by tapered waveguides: application to optical cloaking. *Physical review letters*, 102(21):213901, 2009.

[108] Tom Strudley, Tilman Zehender, Claire Blejean, Erik PAM Bakkers, and Otto L Muskens. Mesoscopic light transport by very strong collective multiple scattering in nanowire mats. *Nature photonics*, 7(5):413–418, 2013.

[109] Tom Strudley, Duygu Akbulut, Willem L Vos, Ad Lagendijk, Allard P Mosk, and Otto L Muskens. Observation of intensity statistics of light transmitted through 3d random media. *Optics letters*, 39(21):6347–6350, 2014.

[110] Shun Lien Chuang. *Physics of photonic devices*, volume 80. John Wiley & Sons, 2012.

[111] AJ Sabbah and D Mark Riffe. Femtosecond pump-probe reflectivity study of silicon carrier dynamics. *Physical Review B*, 66(16):165217, 2002.

[112] ES Harmon, MR Melloch, JM Woodall, DD Nolte, N Otsuka, and CL Chang. Carrier lifetime versus anneal in low temperature growth gaas. *Applied physics letters*, 63(16):2248–2250, 1993.

[113] Nathan P Wells, Paul M Belden, Joseph R Demers, and William T Lotshaw. Transient reflectivity as a probe of ultrafast carrier dynamics in semiconductors: A revised model for low-temperature grown gaas. *Journal of Applied Physics*, 116(7):073506, 2014.

[114] Shantanu Gupta, MY Frankel, JA Valdmanis, John F Whitaker, Gerard A Mourou, FW Smith, and AR Calawa. Subpicosecond carrier lifetime in gaas grown by molecular beam epitaxy at low temperatures. *Applied Physics Letters*, 59(25):3276–3278, 1991.

[115] Shantanu Gupta, John F Whitaker, and Gerard A Mourou. Ultrafast carrier dynamics in iii-v semiconductors grown by molecular-beam epitaxy at very low substrate temperatures. *IEEE Journal of Quantum Electronics*, 28(10):2464–2472, 1992.

[116] L Nevou, J Mangeney, M Tchernycheva, FH Julien, F Guillot, and E Monroy. Ultrafast relaxation and optical saturation of intraband absorption of gan/aln quantum dots. *Applied Physics Letters*, 94(13):132104, 2009.

[117] Norio Iizuka, Kei Kaneko, and Nobuo Suzuki. Near-infrared intersubband absorption in gan/aln quantum wells grown by molecular beam epitaxy. *Applied physics letters*, 81(10):1803–1805, 2002.

[118] Norio Iizuka, Kei Kaneko, and Nobuo Suzuki. All-optical switch utilizing intersubband transition in gan quantum wells. *IEEE journal of quantum electronics*, 42(8):765–771, 2006.

[119] Valentin Ortiz, J Nagle, and Antigoni Alexandrou. Influence of the hole population on the transient reflectivity signal of annealed low-temperature-grown gaas. *Applied physics letters*, 80(14):2505–2507, 2002.

[120] Chi H Lee, A Antonetti, and G Mourou. Measurements on the photoconductive lifetime of carriers in gaas by optoelectronic gating technique. *Optics Communications*, 21(1):158–161, 1977.

[121] KF Lamprecht, S Juen, L Palmetshofer, and RA Höpfel. Ultrashort carrier lifetimes in h+ bombarded inp. *Applied physics letters*, 59(8):926–928, 1991.

[122] FE Doany, D Grischkowsky, and C-C Chi. Carrier lifetime versus ion-implantation dose in silicon on sapphire. *Applied Physics Letters*, 50(8):460–462, 1987.

[123] A Esser, K Seibert, H Kurz, GN Parsons, C Wang, BN Davidson, G Lucovsky, and RJ Nemanich. Ultrafast recombination and trapping in amorphous silicon. *Physical Review B*, 41(5):2879, 1990.

[124] R Rosei. Temperature modulation of the optical transitions involving the fermi surface in ag: Theory. *Physical Review B*, 10(2):474, 1974.

[125] N Del Fatti, C Voisin, M Achermann, S Tzortzakis, D Christofilos, and F Vallée. Nonequilibrium electron dynamics in noble metals. *Physical Review B*, 61(24):16956, 2000.

[126] Philippe Nozieres. *Theory of quantum liquids: Superfluid bose liquids.* CRC Press, 2018.

[127] SI Anisimov, BL Kapeliovich, and TL Perelman. Electron emission from metal surfaces exposed to ultrashort laser pulses. *Zh. Eksp. Teor. Fiz*, 66(2):375–377, 1974.

[128] Lan Jiang and Hai-Lung Tsai. Improved two-temperature model and its application in ultrashort laser heating of metal films. *Journal of heat transfer*, 127(10):1167–1173, 2005.

[129] GL Eesley. Observation of nonequilibrium electron heating in copper. *Physical review letters*, 51(23):2140, 1983.

[130] C-K Sun, F Vallée, LH Acioli, EP Ippen, and JG Fujimoto. Femtosecond-tunable measurement of electron thermalization in gold. *Physical Review B*, 50(20):15337, 1994.

[131] Jongbum Kim, Gururaj V Naik, Alexander V Gavrilenko, Krishnaveni Dondapati, Vladimir I Gavrilenko, SM Prokes, Orest J Glembocki, Vladimir M Shalaev, and Alexandra Boltasseva. Optical properties of gallium-doped zinc oxidea low-loss plasmonic material: first-principles theory and experiment. *Physical Review X*, 3(4):041037, 2013.

[132] Tal Heilpern, Manoj Manjare, Alexander O Govorov, Gary P Wiederrecht, Stephen K Gray, and Hayk Harutyunyan. Determination of hot carrier energy distributions from inversion of ultrafast pump-probe reflectivity measurements. *Nature communications*, 9(1):1853, 2018.

[133] Chennupati Jagadish and Stephen J Pearton. *Zinc oxide bulk, thin films and nanostructures: processing, properties, and applications*. Elsevier, 2011.

[134] YR Ryu, TS Lee, and HW White. Properties of arsenic-doped p-type zno grown by hybrid beam deposition. *Applied Physics Letters*, 83(1):87–89, 2003.

[135] Steven J Byrnes. Multilayer optical calculations. *arXiv preprint arXiv:1603.02720*, 2016.

[136] Lukas Novotny and Bert Hecht. *Principles of nano-optics*. Cambridge university press, 2012.

[137] Hadis Morkoç and Ümit Özgür. *Zinc oxide: fundamentals, materials and device technology*. John Wiley & Sons, 2008.

[138] J Hohlfeld, S-S Wellershoff, J Güdde, U Conrad, V Jähnke, and E Matthias. Electron and lattice dynamics following optical excitation of metals. *Chemical Physics*, 251(1-3):237–258, 2000.

[139] Charles Kittel et al. *Introduction to solid state physics*, volume 8. Wiley New York, 1976.

[140] Alessandra Catellani, Alice Ruini, and Arrigo Calzolari. Optoelectronic properties and color chemistry of native point defects in al: Zno transparent conductive oxide. *Journal of Materials Chemistry C*, 3(32):8419–8424, 2015.

[141] Zhibin Lin, Leonid V Zhigilei, and Vittorio Celli. Electron-phonon coupling and electron heat capacity of metals under conditions of strong electron-phonon nonequilibrium. *Physical Review B*, 77(7):075133, 2008.

[142] Peijun Guo, Richard D Schaller, Leonidas E Ocola, Benjamin T Diroll, John B Ketterson, and Robert PH Chang. Large optical nonlinearity of ito nanorods for sub-picosecond all-optical modulation of the full-visible spectrum. *Nature communications*, 7:12892, 2016.

[143] RM Kaipurath, Monika Pietrzyk, L Caspani, T Roger, M Clerici, C Rizza, A Ciattoni, Andrea Di Falco, and D Faccio. Optically induced metal-to-dielectric transition in epsilon-near-zero metamaterials. *Scientific reports*, 6:27700, 2016.

[144] Xu Fang, Ming Lun Tseng, Jun-Yu Ou, Kevin F MacDonald, Din Ping Tsai, and Nikolay I Zheludev. Ultrafast all-optical switching via coherent modulation of metamaterial absorption. *Applied Physics Letters*, 104(14):141102, 2014.

[145] Ho W Lee, Georgia Papadakis, Stanley P Burgos, Krishnan Chander, Arian Kriesch, Ragip Pala, Ulf Peschel, and Harry A Atwater. Nanoscale conducting oxide plasmostor. *Nano letters*, 14(11):6463–6468, 2014.

[146] Argishti Melikyan, Luca Alloatti, Alban Muslija, David Hillerkuss, Philipp C Schindler, J Li, Robert Palmer, Dietmar Korn, Sascha Muehlbrandt, Dries Van Thourhout, et al. High-speed plasmonic phase modulators. *Nature Photonics*, 8(3):229, 2014.

[147] Benjamin T Diroll, Peijun Guo, Robert PH Chang, and Richard D Schaller. Large transient optical modulation of epsilon-near-zero colloidal nanocrystals. *ACS nano*, 10(11):10099–10105, 2016.

[148] Yoichi Kurokawa and Hideki T Miyazaki. Metal-insulator-metal plasmon nanocavities: Analysis of optical properties. *Physical Review B*, 75(3):035411, 2007.

[149] Jesper Jung, Thomas Søndergaard, and Sergey I Bozhevolnyi. Gap plasmon-polariton nanoresonators: Scattering enhancement and launching of surface plasmon polaritons. *Physical Review B*, 79(3):035401, 2009.

[150] Junghyun Park, Ju-Hyung Kang, Soo Jin Kim, Xiaoge Liu, and Mark L Brongersma. Dynamic reflection phase and polarization control in metasurfaces. *Nano letters*, 17(1):407–413, 2016.

[151] Constantine A Balanis. Antenna theory: A review. *Proceedings of the IEEE*, 80(1):7–23, 1992.

[152] Lukas Novotny. Effective wavelength scaling for optical antennas. *Physical Review Letters*, 98(26):266802, 2007.

[153] Ertugrul Cubukcu and Federico Capasso. Optical nanorod antennas as dispersive one-dimensional fabryprot resonators for surface plasmons. *Applied Physics Letters*, 95(20):201101, 2009.

[154] Salvatore Campione, Sheng Liu, Alexander Benz, John F. Klem, Michael B. Sinclair, and Igal Brener. Epsilon-near-zero modes for tailored light-matter interaction. *Phys. Rev. Applied*, 4:044011, Oct 2015.

[155] S. Vassant, A. Archambault, F. Marquier, F. Pardo, U. Gennser, A. Cavanna, J. L. Pelouard, and J. J. Greffet. Epsilon-near-zero mode for active optoelectronic devices. *Phys. Rev. Lett.*, 109:237401, Dec 2012.

[156] Jens Dorfmüller, Ralf Vogelgesang, R. Thomas Weitz, Carsten Rockstuhl, Christoph Etrich, Thomas Pertsch, Falk Lederer, and Klaus Kern. Fabryprot resonances in one-dimensional plasmonic nanostructures. *Nano Letters*, 9(6):2372–2377, 2009.

[157] Edward D. Palik, editor. *Handbook of Optical Constants of Solids. Handbook of Optical Constants of Solids.* Academic Press, New York, 1985.

[158] Nenad Ocelic, Andreas Huber, and Rainer Hillenbrand. Pseudoheterodyne detection for background-free near-field spectroscopy. *Applied Physics Letters*, 89(10):101124, 2006.

[159] Andrei Andryieuski, Vladimir A. Zenin, Radu Malureanu, Valentyn S. Volkov, Sergey I. Bozhevolnyi, and Andrei V. Lavrinenko. Direct characterization of plasmonic slot waveguides and nanocouplers. *Nano Letters*, 14(7):3925–3929, 2014.

[160] Vladimir A. Zenin, Andrei Andryieuski, Radu Malureanu, Ilya P. Radko, Valentyn S. Volkov, Dmitri K. Gramotnev, Andrei V. Lavrinenko, and Sergey I. Bozhevolnyi. Boosting local field enhancement by on-chip nanofocusing and impedance-matched plasmonic antennas. *Nano Letters*, 15(12):8148–8154, 2015.

[161] Vladimir A. Zenin, Sajid Choudhury, Soham Saha, Vladimir M. Shalaev, Alexandra Boltasseva, and Sergey I. Bozhevolnyi. Hybrid plasmonic waveguides formed by metal coating of dielectric ridges. *Opt. Express*, 25(11):12295–12302, May 2017.

[162] Prashant K. Jain, Wenyu Huang, and Mostafa A. El-Sayed. On the universal scaling behavior of the distance decay of plasmon coupling in metal nanoparticle pairs: A plasmon ruler equation. *Nano Letters*, 7(7):2080–2088, 2007.

[163] Prashant K. Jain and Mostafa A. El-Sayed. Surface plasmon coupling and its universal size scaling in metal nanostructures of complex geometry: Elongated particle pairs and nanosphere trimers. *The Journal of Physical Chemistry C*, 112(13):4954–4960, 2008.

[164] J. Aizpurua, Garnett W. Bryant, Lee J. Richter, F. J. García de Abajo, Brian K. Kelley, and T. Mallouk. Optical properties of coupled metallic nanorods for field-enhanced spectroscopy. *Phys. Rev. B*, 71:235420, Jun 2005.

[165] Edward Mills Purcell. Spontaneous emission probabilities at radio frequencies. In *Confined Electrons and Photons*, pages 839–839. Springer, 1995.

[166] Th Förster. Zwischenmolekulare energiewanderung und fluoreszenz. *Annalen der physik*, 437(1-2):55–75, 1948.

[167] Shaul Mukamel. *Principles of nonlinear optical spectroscopy*, volume 29. Oxford university press New York, 1995.

[168] CR Stephen. Nonlinear and quantum optics using the density matrix, 2010.

[169] Hui Deng, Gregor Weihs, Charles Santori, Jacqueline Bloch, and Yoshihisa Yamamoto. Condensation of semiconductor microcavity exciton polaritons. *Science*, 298(5591):199–202, 2002.

[170] Jacek Kasprzak, M Richard, S Kundermann, A Baas, P Jeambrun, JMJ Keeling, FM Marchetti, MH Szymańska, R Andre, JL Staehli, et al. Bose–einstein condensation of exciton polaritons. *Nature*, 443(7110):409, 2006.

[171] Gabriel Christmann, Raphaël Butté, Eric Feltin, Jean-Francois Carlin, and Nicolas Grandjean. Room temperature polariton lasing in a gan/ algan multiple quantum well microcavity. *Applied Physics Letters*, 93(5):051102, 2008.

[172] S Dufferwiel, S Schwarz, F Withers, AAP Trichet, F Li, M Sich, O Del Pozo-Zamudio, C Clark, A Nalitov, DD Solnyshkov, et al. Exciton–polaritons in van der waals heterostructures embedded in tunable microcavities. *Nature communications*, 6:8579, 2015.

[173] Emmanuelle Peter, Pascale Senellart, David Martrou, Aristide Lemaître, J Hours, JM Gérard, and Jacqueline Bloch. Exciton-photon strong-coupling regime for a single quantum dot embedded in a microcavity. *Physical review letters*, 95(6):067401, 2005.

[174] J Pelal Reithmaier, G Sek, A Löffler, C Hofmann, S Kuhn, S Reitzenstein, LV Keldysh, VD Kulakovskii, TL Reinecke, and A Forchel. Strong coupling in a single quantum dot–semiconductor microcavity system. *Nature*, 432(7014):197, 2004.

[175] Dario Ballarini, Milena De Giorgi, Emiliano Cancellieri, Romuald Houdré, Elisabeth Giacobino, Roberto Cingolani, Alberto Bramati, Giuseppe Gigli, and Daniele Sanvitto. All-optical polariton transistor. *Nature communications*, 4:1778, 2013.

[176] Alexander Dreismann, Hamid Ohadi, Yago del Valle-Inclan Redondo, Ryan Balili, Yuri G Rubo, Simeon I Tsintzos, George Deligeorgis, Zacharias Hatzopoulos, Pavlos G Savvidis, and Jeremy J Baumberg. A sub-femtojoule electrical spin-switch based on optically trapped polariton condensates. *Nature materials*, 15(10):1074, 2016.

[177] S Christopoulos, G Baldassarri Höger Von Högersthal, AJD Grundy, PG Lagoudakis, AV Kavokin, JJ Baumberg, G Christmann, R Butté, E Feltin, J-F Carlin, et al. Room-temperature polariton lasing in semiconductor microcavities. *Physical review letters*, 98(12):126405, 2007.

[178] William L Barnes, Alain Dereux, and Thomas W Ebbesen. Surface plasmon subwavelength optics. *nature*, 424(6950):824, 2003.

[179] Felix Benz, Mikolaj K Schmidt, Alexander Dreismann, Rohit Chikkaraddy, Yao Zhang, Angela Demetriadou, Cloudy Carnegie, Hamid Ohadi, Bart de Nijs, Ruben Esteban, et al. Single-molecule optomechanics in picocavities. *Science*, 354(6313):726–729, 2016.

[180] Brendan G DeLacy, Owen D Miller, Chia Wei Hsu, Zachary Zander, Steven Lacey, Raymond Yagloski, Augustus W Fountain, Erica Valdes, Emma Anquillare, Marin Soljacic, et al. Coherent plasmon-exciton coupling in silver platelet-j-aggregate nanocomposites. *Nano letters*, 15(4):2588–2593, 2015.

[181] Nche T Fofang, Tae-Ho Park, Oara Neumann, Nikolay A Mirin, Peter Nordlander, and Naomi J Halas. Plexcitonic nanoparticles: plasmon- exciton coupling in nanoshell- j-aggregate complexes. *Nano letters*, 8(10):3481–3487, 2008.

[182] Marie-Elena Kleemann, Rohit Chikkaraddy, Evgeny M Alexeev, Dean Kos, Cloudy Carnegie, Will Deacon, Alex Casalis Pury, Christoph Große, Bart Nijs, Jan Mertens, et al. Strong-coupling of wse 2 in ultra-compact plasmonic nanocavities at room temperature. *Nature communications*, 8(1):1296, 2017.

[183] Rohit Chikkaraddy, Bart de Nijs, Felix Benz, Steven J Barrow, Oren A Scherman, Edina Rosta, Angela Demetriadou, Peter Fox, Ortwin Hess, and Jeremy J Baumberg. Single-molecule strong coupling at room temperature in plasmonic nanocavities. *Nature*, 535(7610):127, 2016.

[184] Lukas Novotny. Strong coupling, energy splitting, and level crossings: A classical perspective. *American Journal of Physics*, 78(11):1199–1202, 2010.

[185] Mikhail F Limonov, Mikhail V Rybin, Alexander N Poddubny, and Yuri S Kivshar. Fano resonances in photonics. *Nature Photonics*, 11(9):543, 2017.

[186] Shanhui Fan, Wonjoo Suh, and John D Joannopoulos. Temporal coupled-mode theory for the fano resonance in optical resonators. *JOSA A*, 20(3):569–572, 2003.

[187] Marlan O Scully and M Suhail Zubairy. Quantum optics, 1999.

[188] S Kalusniak, S Sadofev, and F Henneberger. Zno as a tunable metal: new types of surface plasmon polaritons. *Physical review letters*, 112(13):137401, 2014.

[189] Sergey Sadofev, Sascha Kalusniak, Peter Schäfer, and Fritz Henneberger. Molecular beam epitaxy of n-zn (mg) o as a low-damping plasmonic material at telecommunication wavelengths. *Applied Physics Letters*, 102(18):181905, 2013.

[190] Wasanthamala Badalawa, Hiroaki Matsui, Akifumi Ikehata, and Hitoshi Tabata. Surface plasmon modes guided by ga-doped zno layers bounded by different dielectrics. *Applied Physics Letters*, 99(1):011913, 2011.

[191] Edward Sachet, Christopher T Shelton, Joshua S Harris, Benjamin E Gaddy, Douglas L Irving, Stefano Curtarolo, Brian F Donovan, Patrick E Hopkins, Peter A Sharma, Ana Lima Sharma, et al. Dysprosium-doped cadmium oxide as a gateway material for mid-infrared plasmonics. *Nature materials*, 14(4):414, 2015.

[192] Jacob B Khurgin. How to deal with the loss in plasmonics and metamaterials. *Nature nanotechnology*, 10(1):2, 2015.

[193] Jacob Khurgin, Wei-Yi Tsai, Din Ping Tsai, and Greg Sun. Landau damping and limit to field confinement and enhancement in plasmonic dimers. *ACS Photonics*, 4(11):2871–2880, 2017.

[194] Cristian Ciraci, John B Pendry, and David R Smith. Hydrodynamic model for plasmonics: a macroscopic approach to a microscopic problem. *ChemPhysChem*, 14(6):1109–1116, 2013.

[195] Søren Raza, Thomas Christensen, Martijn Wubs, Sergey I Bozhevolnyi, and N Asger Mortensen. Nonlocal response in thin-film waveguides: loss versus nonlocality and breaking of complementarity. *Physical Review B*, 88(11):115401, 2013.

[196] Pavel Ginzburg, Alexey V Krasavin, Gregory A Wurtz, and Anatoly V Zayats. Nonperturbative hydrodynamic model for multiple harmonics generation in metallic nanostructures. *Acs Photonics*, 2(1):8–13, 2014.

[197] Frank H Stillinger and David R Herrick. Bound states in the continuum. *Physical Review A*, 11(2):446, 1975.

[198] Francesco Monticone, Hugo M Doeleman, Wouter Den Hollander, A Femius Koenderink, and Andrea Alù. Trapping light in plain sight: Embedded photonic eigenstates in zero-index metamaterials. *Laser & Photonics Reviews*, 12(5):1700220, 2018.